On the Characteristics of Highly Confined Light Fields: A High-Resolution Interference Microscopy Study

PAR

Myun Sik KIM

(EPFL)

ÉCOLE POLYTECHNIQUE
FÉDÉRALE DE LAUSANNE

Suisse
2011

ABSTRACT

The Investigation of highly confined light fields created by different mechanisms, such as refraction, diffraction, and scattering, are the main subject of this thesis. We distinguish a specific scattering phenomenon of dielectric microspheres from general definition of light scattering that includes refraction and diffraction. Light confinement has been studied by numerous researchers in theoretical ways. However, the experimental approaches for microstructures were always limited due to the lack of resolution and functionalities of the measurement system. To understand the characteristics of optical fields propagating in free space or emerging form microstructures, intensity is not always sufficient. It is therefore necessary to measure the phase of light. The main goal of this work was to set up an optical instrument that is able to measure the amplitude and phase of the light field in the real 3D object space. By combining an optical interferometer (Mach-Zehnder type) with an optical microscope, we have developed a multi-functional high-resolution interference microscope (HRIM). Phase shifting interferometry (PSI) and the five frame (Schwider-Hariharan) algorithm have been introduced in the HRIM in order to directly measure the phase. Auxiliary techniques have been applied for the first time to the experimental setup of the HRIM. For example, multiple-wavelengths light sources for the study of the spectral dependency, immersion of object space for an enhanced resolution and a phase telescope (Bertrand lens) to image and manipulating the Fourier plane (the back focal plane of the objective) have been demonstrated. In addition to a plane-wave illumination, the engineering of the illumination beams allows to broaden the range of experimental investigations for a given sample, such as wavefront management by focused Gaussian beams and focused Bessel beams, and polarization-induced beam shaping for particular shapes of localized illuminations to a small sample.

Our main subject is the confinement of light. Three physical optical mechanisms are discussed in detail: refraction, diffraction and scattering. Discussion is done by examples. We have chosen effects that represent the different effects of physical optics at a microscale: highly focused Gaussian beam for refraction, the spot of Arago and Talbot effect for diffraction and photonic nanojets for scattering. Note that even though scattering in general includes refraction and diffraction, here we use the term "scattering" only for scattered hotspots, *i.e.,* photonic nanojets, by dielectric microspheres. Our study contributes to the understanding of strong confinement in submicron or sub-wavelength dimensions by such effects and show for the first time experimental data on phase and amplitude fields. Basic physical principles, like the Gouy phase shift for focused light were demonstrated for the photonic nanojet, for a complex optical phenomenon where focusing is based on scattering rather than refraction.

We present the capabilities of the HRIM system through a series of measurements of aforementioned problems for highly confined light fields. To meet the proper

experimental conditions for each problem of interest, the HRIM employs several auxiliary techniques of conventional microscopy, *e.g.,* multiple-wavelengths light sources, an immersion technique, and a manipulation of the Fourier plane (the back focal plane of the objective). Engineering of the illumination including polarization-induced beam shaping broadens the range of applications of the instrument and we illustrate this by examples. Furthermore, the HRIM can be operated in two distinguished modes for measurements of the axial phase evolution, "longitudinal-differential mode" or "propagation mode". The longitudinal differential mode directly visualizes peculiar phase evolutions along the optical axis used to prove the phase anomalies. The HRIM with auxiliary techniques therefore serves as a powerful tool for the investigation of highly confined light fields in small volumes.

ABSTRACT

Stark gebündeltes Licht kann durch unterschiedliche Effekte erzeugt werden. Bekannte Mechanismen sind Brechung, Beugung oder Streuung. Der Schwerpunkt dieser Arbeit liegt auf der Untersuchung der Eigenschaften des Lichts wenn es von Mikrostrukturen gebündelt wurde. Um die Eigenschaften optischen Felder zu verstehen und zu interpretieren, ist es oft nicht genügend die Intensitätsverteilung zu kennen. Ein vollständiges Bild ergibt sich nur durch Messung der Phase des Lichts.

In dieser Arbeit wird der Gebrauch und die Entwicklung eines hochauflösenden Multifunktionsmikroskops (HRIM) beschrieben, welches sich ideal für diese Messaufgabe eignet. Das Instrument misst die Intensität und Phase des Lichtes bei höchster Auflösung in kleinen Probevolumen. Um diese Funktionalität zu erreichen wurden zwei Konzepte in einem Instrument kombiniert: Interferometrie und Mikroskopie. Interferometrie ist das ideale Konzept zum Messen der Phase des Lichtes. Zusätzlich dazu hilft ein mikroskopisches Abbilungssystem mit höchster numerischer Apertur bei hoher Auflösung zu messen. Das HRIM besteht also eigentlich aus zwei Geräten: einem Interferometer und einem Mikroskop.

Unser Hauptthema ist stark gebündeltes Lichtes erzeugt von Mikrostrukturen. Die Diskussion wird Anhand von Beispielen geführt. Drei physikalisch-optische Mechanismen werden im Detail besprochen: Brechung, Beugung und Streuung. Wir haben Effekte ausgewählt, die den unterschiedlichen Wirkprinzipien auf der Mikroskala entsprechen. Wir betrachten den Fall eines fokussierten Gaußschen Lichtstrahls als Beispiel für Brechung, den Arago Spot und den Talbot Effekt als Beispiel für die Beugung und den photonischen Nanojet als Beispiel für die Streuung. Unsere Studie trägt wesentlich zum Verständnis der Eigenschaften der Ausbreitung des Lichtes in gebündelten Feldern im Submikron- und Subwellenlängenbereich bei. Für viele hier gegebenen Beispiele sind es die ersten verfügbaren experimentellen Daten. Grundlegende physikalische Phänomene, wie die Gouy Phasenanomalie, werden für den Photonic Nanojet, ein kompliziertes optisches Phänomen bei dem die Bündelung des Lichtes auf Streuung basiert, zum ersten Mal überhaupt demonstriert.

In unserer Arbeit untersuchen wir auch Begrenzungen und weitere Entwicklungsmöglichkeiten des HRIM Systems. Beschäftigt man sich mit Lichtfeldern in kleinen Volumen stellt man fest, dass jede Messaufgabe spezielle Anpassungen an die experimentellen Bedingungen benötigt. Da können zusätzliche Techniken aus Interferometrie oder der Mikroskopie helfen. In dieser Arbeit wurde das HRIM mit einigen dieser zusätzlichen Techniken ausgestattet. So verwenden wir zum Beispiel multispektrale Abbildungen um den Einfluss der Wellenlängen zu demonstrieren, die Immersiontechnik aus der Mikroskopie um höhere Auflösung zu erreichen und die Manipulation der rückwärtigen Brennebene (Fourier-Ebene) um mehr Informationen zu gewinnen. Weitere Beispiele sind Techniken zur Beeinflussung der Polarisation oder der Form und Phase des Beleuchtungsstrahls.

Wir veranschaulichen dies wiederum an ausgewählten Beispielen. Außerdem kann das HRIM in zwei unterschiedlichen Modi für die Aufnahmen der axialen Phasenpropagation arbeitet: Im sogenannten "Längs-differential Modus" oder im "Ausbreitungmodus". Der Längs-differential Modus erlaubt die direkte Messung der Phasenpropagation entlang der optischen Axe in Bezug zu einer Referenzphase. Zusammenfassend lässt sich sagen, dass das HRIM ausgestattet mit zusätzlichen Techniken ein leistungsfähiges Werkzeug für die Untersuchung von stark gebündelten Licht in kleinen Volumen ist.

CONTENTS

ii

Contents

CHAPTER 1

Introduction

OPTICS began with the observation of light and its interactions with matter, *i.e.,* optical phenomena like rainbows and the glow of sunset. The study of such observations helps to uncover the secrets behind natural events (discoveries) and to learn something for applications in our daily life. LIGHT is a part of the electromagnetic radiation that can be seen by humans, which is termed "visible light" in a sense of visual perception of our eyes. Visible light, which is roughly represented by the colors of the rainbow, has a wavelength in a range from about 400 nm (blue) to about 780 nm (red) [1.1]. Since optics is a branch of physics, where the term light often comprises the adjacent radiation regions that are not visible to the human eye, we take an account for the properties of ultraviolet (UV) and infrared (IR) spectrums to find proper explanations and solutions for optical problems that we encounter every day [1.2].

The earliest known lenses were made from polished crystal, often quartz, and have been dated as early as 700 BC for Assyrian lenses, which are presumed to be served as a magnifying glass or a burning-glass to start fires by concentrating sunlight [1.3, 1.4]. Such presumed applications fall into two main categories of modern optics, one having to do with imaging, the other with energy concentration. A lens used as a magnifying glass is an example of imaging, while a lens used as a burning-glass is an example of energy concentration that we define as CONFINEMENT OF LIGHT which is the main subject of this thesis.

Such light confinement has been one of the most interesting subjects from the birth of optics to the latest researches, which now pursue the smallest confinement, such as a sub-wavelength or a submicron dimension. There are varieties of

techniques to confine light into a small volume, such as photonic crystal structures, plasmonic structures, waveguides, lenses, diffraction gratings, scattering objects.

Light has a **W**AVE NATURE, which has two known properties, the amplitude and the phase. Since most sensors including human eyes are only sensitive to the intensity of light, which is the square of the amplitude, observations of light and optical phenomena have hardly ever been for the phase. When other light sources were not coherent enough, the development of **L**ASER in the mid-1960s made the phase measurement feasible in laboratory experiments thanks to the **C**OHERENCE of the light source.

INTERFERENCE is the demonstration of the wave nature of light and moreover a classical way to obtain the phase information of the light wave, which is conducted by comparing the light field of interest (object) with a reference light field (reference) which is correlated or coherent to the object.

1.1 Basic physics of problem of interest

We limit the scope of the problems of interest to that the confinement of light, to which specific cases of three classical effects are applied, takes place in a homogeneous portion of space with an idealization as below:

- Refraction: focusing of light by lenses

    (size of lenses > several centimeters)

- Diffraction: by small single objects or periodic structures

    (size of objects $\geq$ several micrometers or period of periodic structures $\geq \sim\lambda$)

- Scattering: by dielectric microspheres

    (size of spheres $\geq \sim\lambda$)

Even though scattering in general includes refraction and diffraction phenomena, here we separate the scattering problem from the others in order to focus on one particular case for the dielectric microspheres.

1.1.1 Refraction of light

REFRACTION is the bending of a light wave when it passes from one medium to another at the interface separating the two media. It basically occurs due to the speed of light being different in the media of different densities. The amount of bending depends on the indices of refraction of two media and is described quantitatively by the law of refraction (Snell's Law) [1.5]

$$\frac{\sin \theta_1}{\sin \theta_2} = \frac{n_2}{n_1}, \tag{1.1}$$

where θ_1 and θ_2 are incident and refraction angles and n_1 and n_2 are refractive indices of incident and refraction media, respectively. The mechanism of focusing by lenses is the refraction of light. It was Ernst Abbe who first described the relationship between image resolution, angular aperture and refractive index of the medium. He called the new measure of performance of the objective lens *numerical aperture* (NA) and defined it as [1.6]

$$NA = n \cdot \sin \theta, \tag{1.2}$$

where θ is the angle the ray makes with the optical axis (half the value of the angle of the image-forming cone), and n is the refractive index of the medium through which the rays pass. It is clear that θ can never be larger than 90° and since sine of 90° is 1, no objective can have an *NA* numerically larger than the *n* of the medium in which it is working. This implies the maximum acceptance angle for the front lens of the objective of 180°. In practice, the largest angle of acceptance of glass lenses in any medium is around 140°, so the NA of an objective is always less than the theoretical maximum. This will be discussed with examples in chapter 5.

SCALAR theory has limited validity when applied to electromagnetic waves. In orther words, light (a part of the electromagnetic radrition) manifests VECTORIAL charaterstics, which are represented by two transverse components and one longitudinal component of the elctric and magnetic fields. While the low NA system can be described by the scalar theory, the high NA (> 0.6) system demonstrates prominent vectorial properties [1.7]. For instance, a high-NA focusing of a linearly polarized plane wave leads to a strong longitudinal component of the electric field in the focal plane, although it vanishes at the focal point itself [1.8]. Far-field measurement techniques are therefore not able to detect such a feature. The measurement of transverse components leads to assymetry in the transverse spot as a signature of the vectorial effect. Moreover, an analyzer, which is an additional polarizer inserted along the orthogonal direction to the polarization after the object space, can distinguish the orthogonal component from the parallel one.

1.1.2 Diffraction of light

DIFFRACTION is the bending of light by the wave nature of light and behaves differently from refraction. The amount of bending depends on the relative size of the wavelength of light to the size of the object. If the object is much larger than the light's wavelength, the bending will be almost unnoticeable. However, if the two are closer in size or equal, the amount of bending is considerable, and easily seen by naked eye.

Due to the wave nature of light, when diffracted light fields from either a single object or periodic objects fall together at the same position with geometric symmetry, constructive interference can confine light fields in small space. This will be discussed with examples in chapters 6 and 7.

1.1.3 Scattering of light

SCATTERING of light is a general physical process where light is forced to deviate from a straight trajectory by one or more localized non-uniformities in the medium through which it passes [1.9]. Aforementioned light bending phenomena, such as refraction and diffraction, can be included in this definition. However, in this thesis we treat one particular case of the scattering that does not fit in the abovementioned categories but can be described in a scattering model at high precision. The scattering of a monochromatic light by small dielectric spherical objects, whose size is comparable to or bigger than the wavelength, leads to a specific scattering phenomenon, a hotspot with strong confinement, which has been termed *photonic nanojet* since the first publication in 2004 [1.10]. Examples will be given and discussed in chapters 8 and 9.

1.2 Thesis outline

This thesis is a treatise on light confinements studied by means of interferometry with high-resolution techniques. The main motivation is to build an instrument able to investigate the amplitude and phase fields of light with high resolution and moreover in actual three-dimensional (3D) object space. In order to measure and investigate light fields in such high-confinement situations, high-resolution interference microscopy (HRIM) has been considered and different setups have been attempted to fit it into proper experimental geometries for the problems of interest:

- Multiple wavelengths

- Immersion of the object space

- Illumination engineering

- Auxiliary techniques of conventional microscopy

This thesis will demonstrate capabilities of multifunctional HRIM through the different problems linked to highly confined light fields. Light confinement can be realized by different principles. We begin with the discussion of confinement by refraction found in highly focused beams and move onto diffractive and scattering phenomena, which confine light in submicron volume dimension.

This thesis consists of ten chapters. In **Chapter 2**, the interference of light and basics of interferometry, capable of probing the wave properties of light by

measuring amplitude and phase, are discussed. In **Chapter 3** details of the experimental setup of the HRIM are given and explained. **Chapter 4** presents auxiliary techniques to meet proper experimental conditions for specific samples, which are needed to understand measurement principles for applications treated in the following chapters.

Chapter 5 discusses the confinement of light due to refraction. Highly focused Gaussian beams are investigated in oil immersion with a maximum numerical aperture of 1.4. The influence of the variation of the NAs of the focusing and observing objectives is demonstrated. Measured 3D amplitude and phase distributions of such beams are presented and discussed. The smallest spot sizes could be realized because we carried out studies in immersion.

Chapters 6 and **7** present results on light confinement by diffraction. We consider two specific cases: single objects in **chapter 6** and gratings in **chapter 7**. We consider amplitude modulation only. A detailed study of the spot of Arago [1.11] and diffraction from fine gratings is presented. Special attention is paid to the near-field diffraction region where confinement of light occurs by means of interference between diffracted light fields.

Chapter 8 presents an example on scattering confinement by photonic nanojets. Fundamental properties of the photonic nanojet are investigated and the transition from scattering phenomenon to refraction depending on the size of spheres is discussed. **Chapter 9** is dedicated to the engineering of such scattered hotspots for applications. The HRIM offers the possibility to manipulate the illumination and specific nanojet spots are demonstrated.

In **Chapter 10**, we summarize main achievements and conclude.

1.3 References

[1.1]   Wikipedia, "Light," http://en.wikipedia.org/wiki/Light.

[1.2]   Wikipedia, "Optics," http://en.wikipedia.org/wiki/Optics.

[1.3]   D. Whitehouse, "World's oldest telescope?," BBC News (July 1, 1999). http://news.bbc.co.uk/1/hi/sci/tech/380186.stm

[1.4]   Wikipedia, "Nimurd lens," http://en.wikipedia.org/wiki/Nimrud_lens.

[1.5]   M. Born and E. Wolf, *Principles of Optics* (Cambridge University Press, 1999), 7th ed., Chap. 1.

[1.6]   E. Abbe, "On the Estimation of Aperture in the Microscope," J. of the Royal Microscopical Society **1**, 388-423 (1881).

6

Chapter 1. Introduction

[1.7]   S. van Haver, "the Extended Nijboer-Zernike Diffraction Theory and its Applications," Ph.D. thesis, chap. 2, Delft University of Technology, The Netherlands, 2009.
[1.8]   H. P. Urbach and S. F. Pereira, "Focused fields of given power with maximum electric field components," Phys. Rev. A 79, 013825 (2009).
[1.9]   Wikipedia, "Scattering," http://en.wikipedia.org/wiki/Scattering.
[1.10] Z. Chen, A. Taflove, and V. Backman, "Photonic Nanojet enhancement of backscattering of light by nanoparticles: a potential novel visible-light ultramicroscopy technique," Opt. Express **12**, 1214-1220 (2004).
[1.11] M. Born and E. Wolf, *Principles of Optics* (Cambridge University Press, 1999), 7th ed., Chap. 8.

Chapter 2

Interference and interferometry

INTERFERENCE is in general the interaction between waves traveling in the same space that, combined with each other, produce a resultant wave in accordance with the principle of superposition. When two waves superpose, depending on the phase differences along the waves, constructive or destructive interferences might occur. Since light has a wave nature, such effects are also found for light and when light waves are coherently combined the resulting distribution of energy is given as the sum of the amplitude and phase of all waves and this is called interference of light.

In constructive interference, the amplitudes of the wave are added and become larger than the single amplitudes. This happens for instance when the two waves are in phase as two wave crests reach the same point simultaneously, and then the wave height is the sum of the two individual waves. Destructive interference is based on the same mechanism and describes the situation when waves cancel out each other. This can happen when waves are out of phase and as an example the crests of one wave coincide with the troughs of the other. In the following sub-sections, we will discuss more technical aspects in order to utilize such phenomenon in our study.

2.1 Two-beam interference

We derive equations for the two-beam interference that is the fundamental working principal of interferometric measurement systems. A light wave can be described by its frequency, amplitude, and phase, and the resulting interference pattern between

two waves depends on these properties, among others. The two-beam interference equation that describes the resulting intensity *I* for monochromatic waves is

$$I = A_1^2 + A_2^2 + 2A_1A_2 \cos(\phi_1 - \phi_2), \tag{2.1}$$

where A_1, A_2 and ϕ_1, ϕ_2 are the amplitude and phase of the individual light beams, respectively. In practice, instruments and detectors respond only to irradiance (= intensity), *I*, which is the square of the electric field amplitude, A^2. Equation (2.1) can be re-derived by using the single beam intensities I_1 and I_2 as

$$I = I_1 + I_2 + 2\sqrt{I_1 I_2} \cos(\phi_1 - \phi_2). \tag{2.2}$$

Interferometers intend to measure the phase difference between a reference beam and an object beam, $\Delta\phi = \phi_1 - \phi_2$, which is a relative value rather than the absolute phase of the light wave of interest.

2.2 Interferometer

An **I**NTERFEROMETER is an optical device that utilizes the interference phenomenon to obtain useful parameters based on amplitude and phase information. Interferometers divide an incident beam into two beams, delay them by making them travelling over two different paths, recombine them at the output, and detect the resulting intensity. This task can be achieved by using different optical configurations. Among them, two typical setups for reflection and transmission are given in Fig. 2.1, which were named after their inventors Michelson [2.1] and Mach-Zehnder [2.2, 2.3] interferometers, respectively.
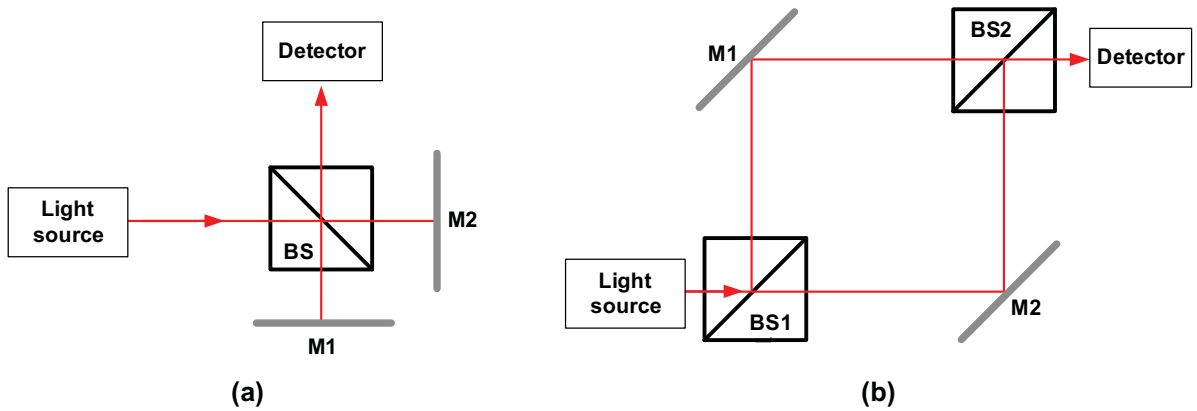

Fig, 2.1: *Schematics of (a) Michelson interferometer and (b) Mach-Zehnder interferometer.*

The Michelson interferometer uses a single beam splitter (BS), which divides and recombines the waves. Two mirrors (M1, M2) reflect the light back to the beam splitter as shown in Fig. 2.1(a). The Mach-Zehnder interferometer starts with one input beam and splits it into two separate beams, such as a reference beam and an object beam by the first beam splitter (BS1). While one arm, the reference arm, in general preserves the original properties of the input beam, the second, the object arm, introduces external influences, *e.g.,* optical path length changes, refractive index changes, or disturbance of the object beam by a sample. At the output, another beam splitter (BS2) recombines these two beams and the result is observed by a detector as shown in Fig. 2.1(b). Mach-Zehnder interferometry is applied to investigate small objects in transmission with connection to the microscopic imaging system, which will be discussed in detail in chapter 3.

2.3 Phase shifting interferometry

When we obtain interference fringes, additional techniques are required to extract useful information out of them. Advances of computers' capability allowed digitalizing such interferograms for further analysis. Phase shifting interferometry (PSI) is a well established technique that allows (in conventional optical interferometers) the evaluation by recording a series of interferograms where the phase of one of the two interfering beams is changed by a known amount and direction between images. Intensity variations across the measurement plane, either from pixel to pixel nonuniformity or source distributions, only weakly influence the measurement since the phase is calculated at each pixel independently [2.4]. When two dimensional (2D) interferograms are recorded, the result is a phase map at a fixed grid of points, which represents the wavefront. The basic equation can be found as following. By substituting I_{dc} for $I_1 + I_2$ and I_{ac} for $2\sqrt{I_1 I_2}$ into Eq. (2.2), we derive a simplified two-beam interference equation for PSI as

$$I = I_{dc} + I_{ac}\cos(\phi+\delta)\,,\qquad\qquad(2.3)$$

where ϕ is the unknown phase of interest, and δ is a known phase shift.

2.3.1 Phase shifting methods

Since there are three unknowns, I_{dc}, I_{ac}, and ϕ, in Eq. (2.3), at least three interferogram images are needed to determine the phase ϕ. To obtain this multiple interferogram images, a phase shift is introduced in the optical path of one beam with respect to the other beam. The most straightforward and most common method for changing the phase is a movable mirror in the reference arm of the optical

interferometer. The displacement of a moving mirror requires nanometric precision to achieve a shift within a fraction of the optical wavelength. Therefore, PSI is commonly equipped with a piezoelectric transducer (PZT) to introduce such small moving steps of the mirror.

2.3.2 Phase shifting algorithms

The most common phase shift used in the algorithm is δ equal to 90° or $\pi/2$, which is equivalent to a quarter of the wavelength ($\lambda/4$) for a single-path setup (for transmission), for example, a Mach-Zehnder interferometer.

Once the phase shift is implemented in the measurement system, the recorded series of interferograms must be analyzed to find the phase at each pixel in the 2D images. For example, letting $\delta_1 = 0°$, $\delta_2 = 90°$, $\delta_3 = 180°$, $\delta_4 = 270°$, $\delta_5 = 360°$, the intensity at each pixel of recorded images can be found by Eq. (2.3) as [2.4]

$$I_1 = I_{dc} + I_{ac}\cos(\phi)$$
$$I_2 = I_{dc} - I_{ac}\sin(\phi)$$
$$I_3 = I_{dc} - I_{ac}\cos(\phi) \quad\quad\quad (2.4)$$
$$I_4 = I_{dc} + I_{ac}\sin(\phi)$$
$$I_5 = I_{dc} + I_{ac}\cos(\phi).$$

As mentioned before, the minimum number of interferograms needed to determine the phase ϕ is three, but more images help to reduce the errors due to possible phase shift errors. For instance, with the fourth image one can apply to the four step algorithm and the phase is found in [2.4]

$$\phi = \tan^{-1}\left(\frac{I_4 - I_2}{I_1 - I_3}\right). \quad\quad\quad (2.5)$$

One more step provides further improvement, which is known as *Schwider-Hariharan algorithm* [2.5-2.7]. The fifth image, where $\delta_5 = 360°$, is nominally identical to the first, but proper mathematical treatment leads to a modification of Eq. (2.5) as

$$\phi = \tan^{-1}\left(\frac{2(I_2 - I_4)}{2I_3 - I_5 - I_1}\right), \qu\quad\quad (2.6)$$

which is much less sensitive to the miscalibration of the phase shifter. By going from 4 steps to 5 steps of the Schwider-Hariharan algorithm, the error due to a 5% incorrect phase shift is reduced by nearly a factor of 25 [2.4, 2.7]. We can further

reduce the errors by several orders of magnitude by using more steps [2.4, 2.7], but this five step algorithm is sufficiently robust to the phase shift error since other errors are generally larger.

2.4 References

[2.1] A. A. Michelson, "The relative motion of the earth and the luminiferous ether," Amer. J. Sci. **22**, 120-129 (1881).

[2.2] L. Zehnder, "Ein neuer Interferenzrefraktor," Zeitschrift für Instrumentenkunde **11**, 275-285 (1891).

[2.3] L. Mach, "Über einen Interferenzrefraktor," Zeitschrift für Instrumentenkunde **12**, 89-93 (1892).

[2.4] E. P. Goodwin and J. C. Wyant, *Field Guide toInterferometric Optical Testing* (SPIE 2006), p 32-42.

[2.5] J. Schwider, R. Burow, K.-E. Elssner, J. Grzanna, R. Spolaczyk, and K. Merkel, "Digital wave-front measuring interferometry: some systematic error sources," Appl. Opt. **22**, 3421-3432 (1983).

[2.6] P. Hariharan, B. F. Oreb, and T. Eiju, "Digital phase-shifting interferometry: a simple error-compensating phase calculation algorithm," Appl. Opt. **26**, 2504-2506 (1987).

[2.7] J. C. Wyant, "Optics 505" class note, Chap. 9. (http://www.optics.arizona.edu/jcwyant/)

12

Chapter 2. Interference and Interferometry

CHAPTER 3

High-resolution interference microscopy

HIGH-RESOLUTION INTERFERENCE MICROSCOPY (HRIM) is a kind of holographic microscopy with in-line geometry in a sense of recording interferograms and retrieving information of light fields of interest, especially amplitude and phase distributions. As long as HRIM relies more on interferometry, such as a Mach-Zehnder interferometer and phase shifting techniques, than holographic techniques, we have named our experimental system an interference microscope. Interferometric testing systems have been developed for 2D measurements, for example, surface profiling and wavefront measurements of light fields in a plane of interest [3.1]. The major difference from other types of interference microscopes is the capability to record real three-dimensional amplitude and phase fields by scanning the samples in the axial direction with particular illuminations when they are necessary. The HRIM has been already proven as a powerful tool for the 3D characterizations of macro- and micro-optics [3.2, 3.3] and to measure light field features with nanometric precision [3.4]. In this chapter we present working principals and details of the experimental setup of the HRIM.

3.1 Basic system setup

We conceptually distinguish three functional blocks.

---

* Contents of section 3.2 partially based on [3.3] M.-S. Kim, T. Scharf, and
   H. P. Herzig, Opt. Express 18, 14319-14329 (2010).

14

The optical interferometer is the core to apply interference technique with the aim to investigate both amplitude and phase of the light distribution emerging from the sample. It is designed to work in transmission for visible light. All optical paths are in free space. The interferometer applies phase shifting interferometry that involves a moving mirror driven by a piezo actuator in the reference arm. A classical five frame algorithm, called the Schwider-Hariharan method, allows to precisely extract the phase information.

The optical microscope with highest magnification and numerical aperture lenses is the backbone of the observation system, which is able to probe light fields confined in micrometric or even in sub-wavelength dimensions. All standard microscopy techniques for resolution and contrast enhancement can be applied.

The illumination block offers the possibility to vary the illumination and allows 3D measurements under controlled illumination conditions, which is unique in our HRIM when compared to others.

3.1.1 Optical interferometer

Among various configurations of interferometers, a Mach-Zehnder interferometer shown in Fig. 3.1(a) is well-known for transmission-mode experiments. As illustrated in Fig. 3.1(b), the HRIM employs this transmission type arrangement with a modification of optical paths in order to implement phase shifting interferometry in the reference (Ref.) arm and an optical microscope (section 3.1.2) in the object (Obj.) arm.
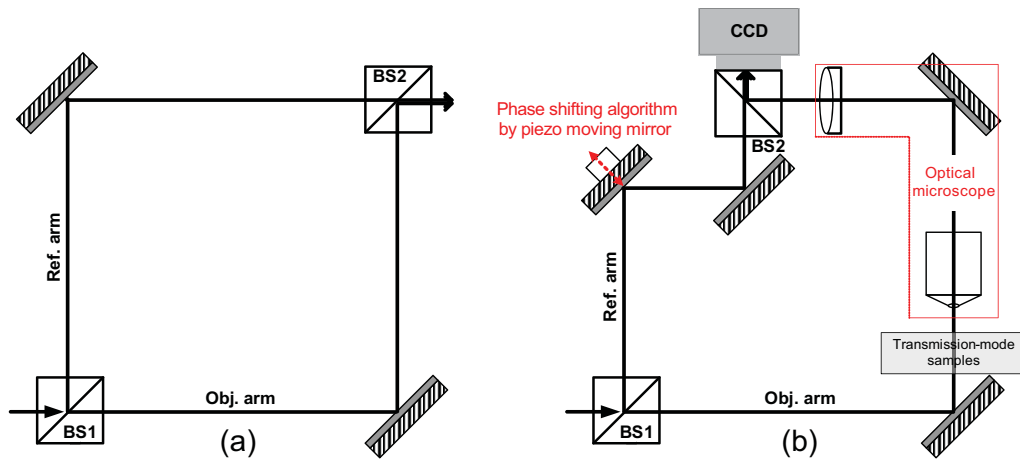

Fig. 3.1: *Schematic diagrams of optical interferometers: (a) a conventional Mach-Zehnder interferometer and (b) a modified Mach-Zehnder interferometer implemented in the HRIM with adjusted optical paths in order to apply a phase shifting interferometry (in Ref. arm) and an optical microscope (in Obj. arm).*

Detailed information of experimental configurations and optical elements can be found in Fig. 3.2, which shows a schematic view of the system with all components.
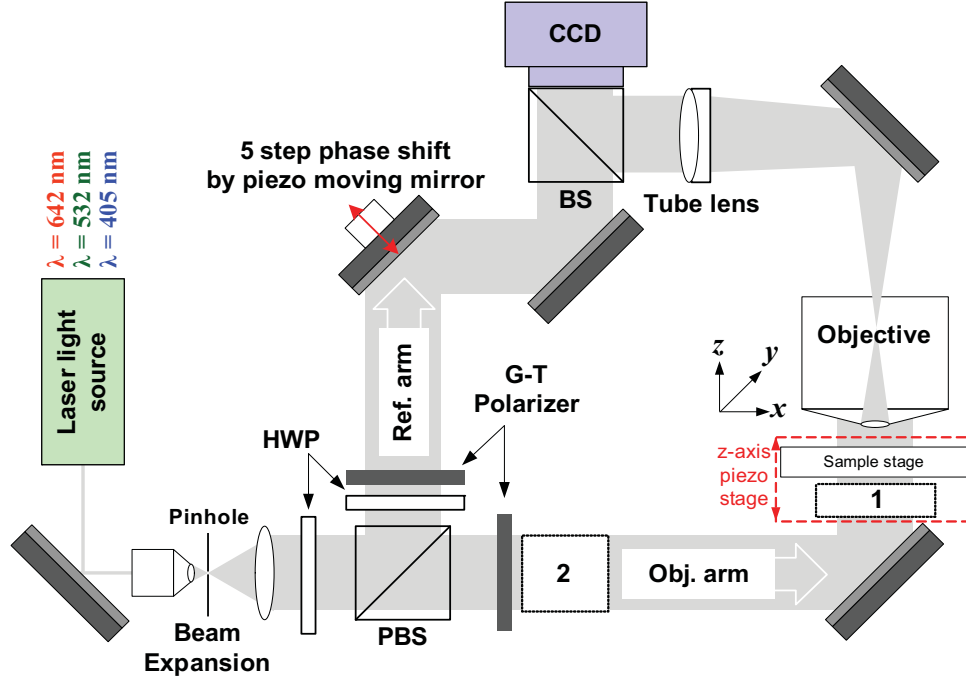
Fig. 3.2: *Schematic of the experimental setup. After divided by the polarizing beam splitter (PBS), a linearly polarized plane wave emerges in both the reference (Ref.) and object (Obj.) arms. In the reference arm, the piezo driven mirror modulates the optical path by five steps of 90° (= λ/4). In the object arm, additional elements to manage polarization and illumination can be introduced at position of squares one or two.*

For light sources, three single mode polarized laser diodes with different powers and wavelengths are used (CrystaLaser, 642nm: DL640-050-3, 532nm: IR-GCL-025-S, 405nm: BCL-040-405-S). Such multiple wavelengths can be applied to to investigate spectral dependency or chromatic behaviors of the light fields of interest. The beam diameters from the laser sources are approximately 1 mm ($1/e^2$ intensity). A beam expander, a Keplerian telescope, expands the emerging laser beams to a diameter of 10 mm, which is the smallest clear aperture size of optical components in the HRIM. In addition, spatial filtering is implemented by placing a pinhole at the focus of the first lens. A polarizing beam splitter (PBS) divides intensities to be sent to the reference arm and the object arm. Half wave plates (HWP) and Glan-Taylor (G-T) polarizers are used to adjust the intensities and to optimize the contrast of interference fringes. In the object arm the expanded and collimated beam directly illuminates the system under investigation unless additional illumination components and/or polarization controllers are inserted at position one or two in Fig. 3.2. The beam splitter (BS) combines light fields from the reference arm and the

object arm that form interference fringes which are sent to a charge-coupled device (CCD) camera. The CCD camera records the 2D fringe images corresponding to the image plane of the observing objective, the plane of interest in the object space. The samples and additional illumination elements are mounted together on a precision piezo stage with a z-scan range of 500 μm and a nominal accuracy of 1 nm (Mad City Labs Inc., Nano-Z500). Scanning them together leads to the 3D measurements under constant illumination conditions.

After interferograms are recorded, we need a supplementary technique to obtain the 2D phase distributions from the measured data. This can be done either by numerical methods like in digital holography or by direct retrieval methods like in phase shifting interferometry (PSI). The HRIM is equipped with PSI. In the reference arm, a piezo-electrically driven mirror (Mad City Labs Inc., Nano-P15) is mounted to change the optical path lengths as illustrated in Figs. 3.1 (b) and 3.2. Five frames of fringe images are recorded with a phase shift of 90° (= $\lambda/4$) by each. The Schwider-Hariharan algorithm leads to Eq. (2.6) that is applied to find the phase information.

3.1.2 Optical microscope

In order to probe micro-size samples and light fields, an optical microscope is implemented in the object arm of the HRIM. It consists of infinity-corrected objectives and a tube lens from Leica Microsystems as shown in Fig. 3.2. A CCD camera is placed in the back focal plane of the tube lens without additional imaging components. The magnification of the objectives fixes the size of the field of view. For example, at 100X magnification, a pixel on a CCD sensor corresponds to 46.5 nm in the object plane. With an image sensor of 1360 x 1024 pixels, the maximum field of view of the CCD camera becomes 64 x 48 μm^2 (Sicon Corporation, CFW1312M camera with SONY ICX205AK image sensor of 1360 x 1024 pixels).

In general, a high numerical aperture (NA) of the observation objective ensures high resolution of the amplitude and phase measurements. Moreover, high magnification provides more pixels on an image sensor for small objects until the maximum useful magnification is reached. In order to achieve the optimum resolution we use highly corrected objectives with high numerical apertures, for example, a 100X / NA 0.9 dry objective (Leica Microsystems, HC PL FLUOTAR) and an oil immersion objective with 100X magnification and a NA of 1.4 (Leica Microsystems, HCX PL APO). We apply these objectives either for observation or illumination. For the immersion objective, a standard immersion oil with the refractive index of n_D = 1.515 (Leica Microsystems, Type N immersion liquid) was chosen as a gap medium. Depending on the size of the sample, a proper magnification should be chosen to image the whole field. Moreover, the thickness of the medium for immersion or in which the sample is imbeded should be accurately

considered to bring the focal plane of used objectives to the effective region of interest near by the sample. All available objective lenses equipped in the HRIM are listed in the Table 3.1.

Table 3.1: *Objective lenses and characteristics*

Type	Magnification	NA	Free working distance	Immersion	Correction
HCX APO	100	0.7-1.4	90 µm	Oil	*Apochromat
HC PL FL	100	0.9	270 µm	Air	**Fluotar
HCX APO	50	0.9	280 µm	Air	Apochromat
N PLAN	50	0.5	7.1 mm	Air	***N PLAN
HC PL FL	20	0.5	1.15 mm	Air	Fluotar
HC PL FL	10	0.3	11 mm	Air	Fluotar
HC PL FL	5	0.15	13.7 mm	Air	Fluotar

* Apochromat: the highest degree of correction for spherical and chromatic aberrations.

**Fluotar: Semi-apochromatic correction for spherical and chromatic aberrations.

***N PLAN: nomal field of view plan correction.

3.1.3 Illumination engineering and 3D data recording

Under standard measurement conditions, an expanded collimated beam which resembles a plane wave with linear polarization parallel to the *x*-axis illuminates the sample as depicted in Fig. 3.2. By including additional illumination components, such as an aperture, a lens or a spatial light modulator installed into the position of the square one in Fig. 3.2, one can modify the amplitude and/or phase distributions of the incident beam. Two typical examples for such elements as used in our experiments are illustrated in Fig. 3.3. Figure 3.3(a) describes the generation of a spherical wavefront by focusing the light with an objective close to the bottom of the sample. We define the entrance plane where the illumination starts to interact with the sample. When the central part of a plane-wave illumination is blocked, the amplitude distribution in the focal plane resembles a zeroth-order Bessel function of the first kind in radial direction within finite extentions [3.5 3.6]. The focusing causes a Gaussian apodization in the amplitude distribution that can be represented as a product of a Bessel function and a Gaussian profile. This type of experimental Bessel beams are known as *Bessel-Gauss beams* [3.7] or a focused Bessel beams. Unlike a diffraction-free beam [3.8, 3.9], such beam carries a finite power and

18

transverse and longitudinal extensions due to the fast decrease of the Gaussian profile. Figure 3.3(b) illustrates how to generate a focused Bessel beam (Bessel-Gauss beam) illumination by using a focusing lens and an annular pupil creating an annular illumination by blocking the central part of a plane-wave illumination beam by an opaque disc.
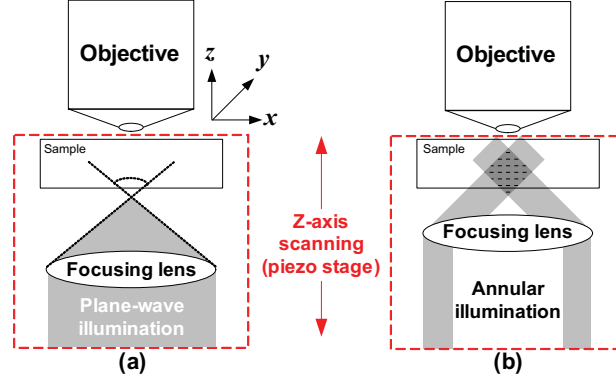

Fig. 3.3: _Use of additional illumination components: (a) a spherical-wavefront illumination is obtained by simply adding a focusing lens into the position of square one (Fig. 3.2) and either a converging or diverging wavefront can be adjusted by properly placing the foci with respect to the entrance plane of the sample. A Bessel-Gauss beam illumination in (b) requires focusing an annular incident beam. Elements are fixed on the same piezo stage to be moved together with the sample in order to keep illumination conditions constant during the z-axis scanning._

When illumination components are inserted underneath the sample into the position of the square labeled with one, they are fixed on the same piezo-stage as the sample. Since a plane-wave incidence on the additional illumination component is guaranteed, the sample together with illumination elements can be scanned in the axial (z) direction without changing the illumination conditions of the sample. In this manner we assure to measure 3D amplitude and phase distributions with fixed and specific illumination conditions. Figure 3.4 shows examples of amplitude and phase distributions under various illuminations without a sample, hence only the illumination is shown. Focused Gaussian beams for a low NA (0.15) and a high NA (0.9) are given in Figs. 3.4(a) and 3.4(b), respectively. Figure 3.4(c) shows the correspondign phase distribution of Fig. 3.4(b). We can see the converging and diverging wavefronts. By blocking 70 % of the central part of the entrance pupil, Bessel-Gauss beams are experimentally realized. Measurements are shown in Figs. 3.4(d) and 3.4(e) for NA = 0.15 and for NA = 0.9, respectively. Figure 3.4(f) presents the corresponding phase distribution of data given in Fig. 3.4(e). A diamond-shape overlapping region of two plane waves is demonstrated as expected. Compared to the focused Gaussian beams in Figs. 3.4(a) – 3.4(c), the longer focal depth of the Bessel-Gauss beams in Fig. 3.4(f) is a clear signature for a strongly

suppressed diffraction and the evolution of the phase in space corresponds to interfering plane waves. Both are properties usually associated with Bessel-Gauss beams. As discussed above, the properties of the Bessel-Gauss beams obtained with our experimental approach are different from Bessel beams obtained for instance by an axicon or a micro-size-opening annular slit [3.8, 3.9], but fully sufficient for our study.
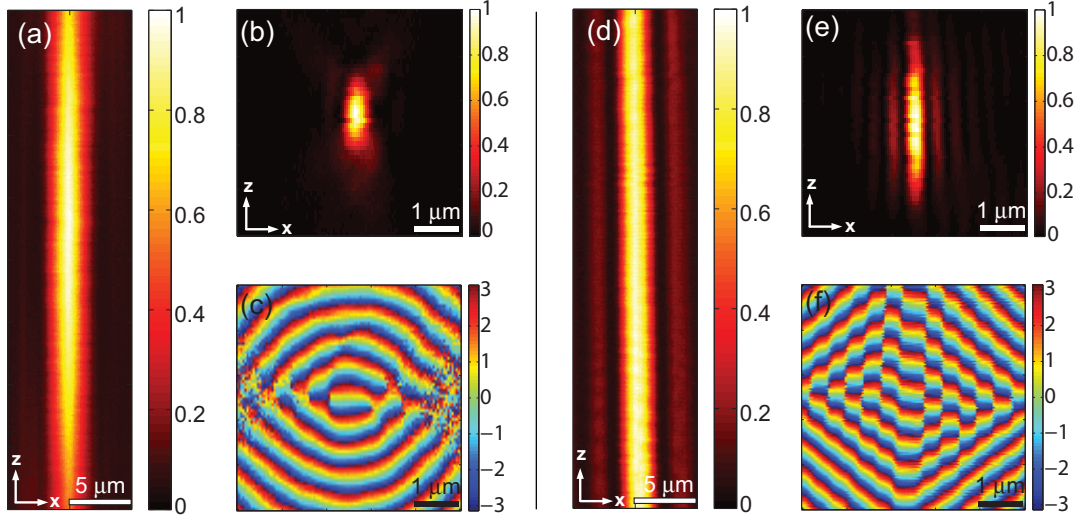

Fig. 3.4: *The x-z slices of the measured 3D intensity and phase distributions of various illuminations. They are measured without a sample. The intensity distributions of focused Gaussian beams of low NA (a) and high NA (b) and corresponding phase distribution (c), The intensity distributions of focused Bessel beams of low NA (d) and high NA (e) and corresponding phase distribution (f). Please note that the scales in low NA and high NA beams are different, which are indicated by a scale bar in each image. Intensities are all normalized.*

3.2 Performance evaluation

The HRIM demonstrates a diffraction-limited resolution for amplitude measurements and a super-resolution for phase measurements [3.4]. Therefore, we minimally describe our instrument as a high-resolution system, which stands for the diffraction-limited performance. Since our research targets, which are presented in chapters 5 - 9, are light fields propagating in a homogenous medium (quasi-free space) rather than physical objects, the measured spots are not broadened by the microscope objective. The small aberrations of the microscope objective have not been considered, because they have no major influence on the measurements. We present now the details of the practical aspects for the resolution in amplitude and phase fields with actual examples.

3.2.1 Nominal lateral and axial resolutions for amplitude measurements

The resolving power, *i.e.,* resolution, of an optical imaging system like a microscope can be limited by several factors such as imperfections in the lenses or misalignments. However, there is a fundamental limitation to the resolution of any optical system which is due to diffraction. An optical system with the ability to produce images with angular resolution as good as the instrument's theoretical limit is said to be diffraction limited [3.10]. Assuming that optical aberrations in the whole optical setup are negligible, the lateral resolution *d* can be stated as [3.11, 3.12]:

$$Abbe\,limit\,(d) = \frac{\lambda}{2NA}, \qquad (3.1)$$

where λ is the operation wavelength and NA is the numerical aperture of the system. This limit has been named in honour of Ernst K. Abbe (Fig. 3.5), who founded the theory of image formation for microscopy. The nominal lateral resolutions for a 100X / NA 0.9 objective and 100X / NA 1.4 objective are calculated at a wavelength of 642 nm by Eq. (3.1) to be 357 nm and 229 nm, respectively. Along the optical axis, the Rayleigh criterion of resolution can be applied with the simplified formula derived as [3.13]:

$$\Delta z = \frac{n \cdot \lambda}{NA^2}, \qquad (3.2)$$

with *n* the refractive index of the immersion medium. The calculated axial resolutions at 642 nm wavelength are 792 nm for the 100X / NA 0.9 objective and 491 nm for the 100X / NA 1.4 immersion objective.
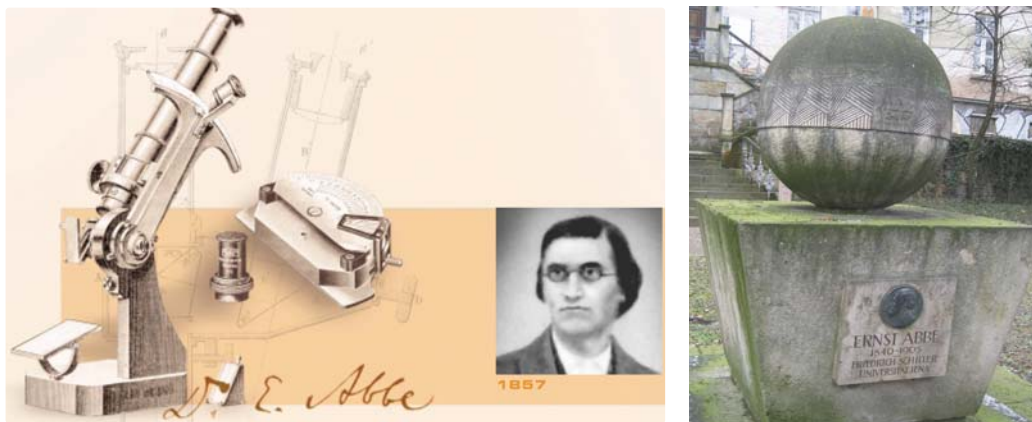

Fig. 3.5: *Ernst K. Abbe [3.14] and the memorial at the Friedrich-Schiller-Universität Jena, Germany.*

3.2.2 Amplitude resolutions in a real application

When the numerical aperture and the refractive index of the object space are fixed, the only variable in Eq. (3.1) is the operation wavelength. Thus, the nominal resolutions are only reference values for the ideal case rather than an absolute ruler. In reality, all the experimental conditions influence the actual resolution. For example, illumination conditions, alignment, quality of the sample and associated optical elements, and their changes with environmental conditions like temperature also influence the resolution. Therefore, it is of preference to study the resolution of the system during the actual investigations by comparing measurements to simulations.

As an example, we verify the actual resolution of the HRIM setup by comparing the measured spot size of photonic nanojets, which has a weakly sub-diffraction spot size [3.15], with rigorous simulation results. The appearance and the position of such scattered hotspots are unique and it is universal for all optical wavelengths. For instance, when a plane wave ($\lambda = 642$ nm) illuminates a glass microsphere (diameter $= 2$ μm; $n = 1.55$), such sphere creates a tiny hotspot on the shadow-side surface of the sphere. Observations with a 100X / NA0.9 objective in the HRIM lead to 3D intensity measurements as shown in Fig. 3.6. Next, we compare these experimental results to rigorous simulations.

The well-known Mie theory for a single sphere can be used to simulate the optical response of the glass microsphere. We give here the general layout of the simulation principles. Simulations were performed in collaboration with S. Mühlig and C. Rockstuhl (Friedrich-Schiller-Universität Jena, Germany) and based on scalar propagation techniques in spatial frequency space. First one calculates the x-component of the electric field $E_x(x,y,z,\omega)$ (that corresponds to the polarization of the incident field) with Mie theory in the x-y-plane at $z = 10$ μm. After Fourier transforming the field to the spatial frequency space [$E_x(k_x,k_y,z{=}10\mu m,\omega)$], all contributions of spatial frequencies (k_x and k_y) whose absolute value is larger than the numerical aperture of the observing objective of the HRIM divided by the incident wavelength are suppressed. This mimics the behavior of the observing objective in the experiments. Afterwards, this modified x-component of the electric field is propagated to the slice of interest in z-direction by means of free space propagation.

In Fig. 3.7, simulations show excellent agreement with experiments seemingly justifies the performance of the HRIM with proper considerations. For instance, the transverse full width at half maximum (FWHM) spot sizes are measured to be 380 nm, 340 nm, and 230 nm for the wavelengths 642 nm, 532 nm, and 405 nm, respectively. Corresponding simulation results are 380 nm, 330 nm, and 250 nm for the wavelength 642 nm, 532 nm, and 405 nm, respectively.

Chapter 3. High-resolution interference microscopy
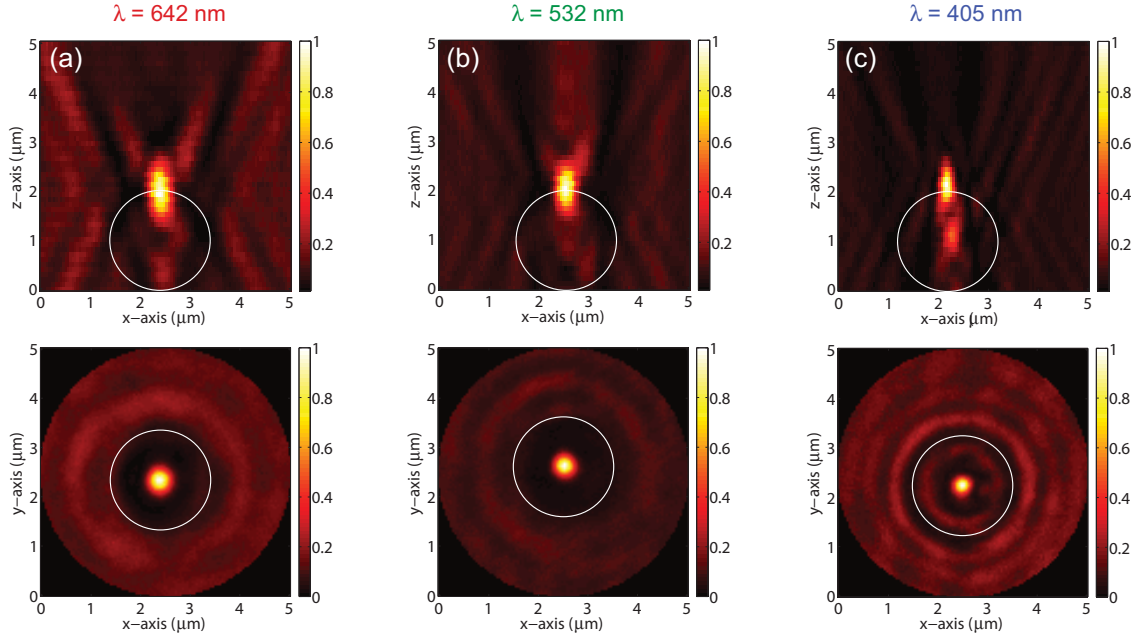
Fig. 3.6: *Measured intensity distributions of photonic nanojets from a 2-μm glass sphere for different wavelengths: (a) 642 nm, (b) 532 nm and (c) 405 nm. The bottom surface of the sphere is set to the z = 0 μm. The white circle indicates the 2-μm sphere. Intensities are all normalized.*
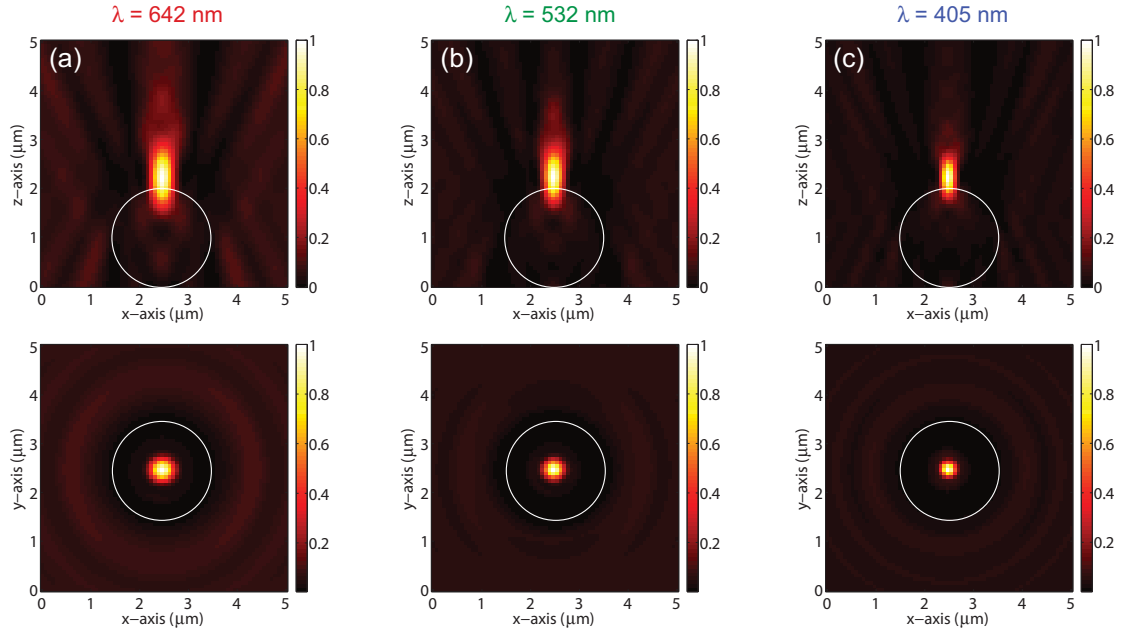
Fig. 3.7: *Corresponding simulations to Fig. 3.6: (a) 642 nm, (b) 532 nm and (c) 405 nm. They are rigorously calculated by the Mie theory and the scalar propagation technique with the consideration of the NA of the observation system. Intensities are all normalized.*

Our experimental system works within the theoretical framework and its performance is reliable with careful considerations of the diffraction limit. The longitudinal (axial) spot size also corresponds to a diffraction-limited imaging performance. The position of the plane of maximum intensity is found very close to the correct position because diffraction limits not the position accuracy but the measurable size of an object for a single object. More details of simulations for the photonic nanojet will be discussed in chapter 8.

3.2.3 Phase resolution

The lateral position accuracy of specific phase features, such as the position of phase jumps or singularities, are not subject to the diffraction limit [3.4]. For example, since singularities are mathematically exact points, measuring their distance or position is only limited by the signal-to-noise ratio, and therefore super-resolution is generally possible. However, this super-resolution does not refer to a physical object but only to particular topological features in the wave-field. Therefore, the resolution in the *x-y* phase plane is in general given by the demagnified size of the pixels from the image (camera) plane to the object plane. The HRIM demonstrated a lateral position accuracy down to 20 nm for the wave-fields [3.16].

Since the phase is obtained by interferometric techniques, the resolution of the interferometric phase measurements depends on the quality of the beams in the reference and object arms. As the HRIM records 2D interferograms, we can easily verify the beam quality of incident waves relative to the reference. The measurement of a known wavefront allows to evaluate wavefront errors, which are considered as the phase resolution of the HRIM. Since the fitting with a plane wave leads to fewer uncertainties than the spherical wave fitting, the best situation is to measure an emerging plane wave and compare it to the ideal plane wavefront.

A lens collimates an incoming spherical wave and transforms it in the ideal case into a plane wave when the focal point of the spherical wave is brought into the focus of the lens. The wavefront errors are obtained by comparing the measured wavefront emerging from the lens with an ideal plane wave. This is one example of typical optical shop testing application of the HRIM [3.3]. By testing a microlens, whose aberrations are negligible, *i.e.,* it is diffraction limited, we can demonstrate the phase resolution of the HRIM. Wavefronts of the collimated beam by the test lens, whose *strehl ratio* [3.10] is close to unity, are measured and wavefront errors are evaluated as shown in Fig. 3.8. Experimental details are given in reference 3.3.

In the lower row of Fig. 3.8, the smallest wavefront errors within the full lens aperture of 20-μm diameter are found to be 0.02λ for 405 nm, 0.02λ for 532 nm, and 0.01λ for 642 nm. We consider the practical resolution limit of the phase measurement is about 0.01λ by taking the result of 642 nm wavelength. The most

critical noise source during the measurements is mechanical vibration in the current HRIM system due to the standing setup confituration, which provides flexibilities for modifying the setup and implementing auxilary techniques, but is less robust to vibration than the in-plane configuration (the setup laid down on the optical table). When ten identical measurements of Fig. 3.8 at 405 nm wavelength are performed, the average is found 0.04λ and the standard deviation 0.014λ. These values are a guideline of the phase resolution of the actual measurement not the absolute resolution limit. Such phase resolution can be improved by using better optical components and proper sample preparation techniques.
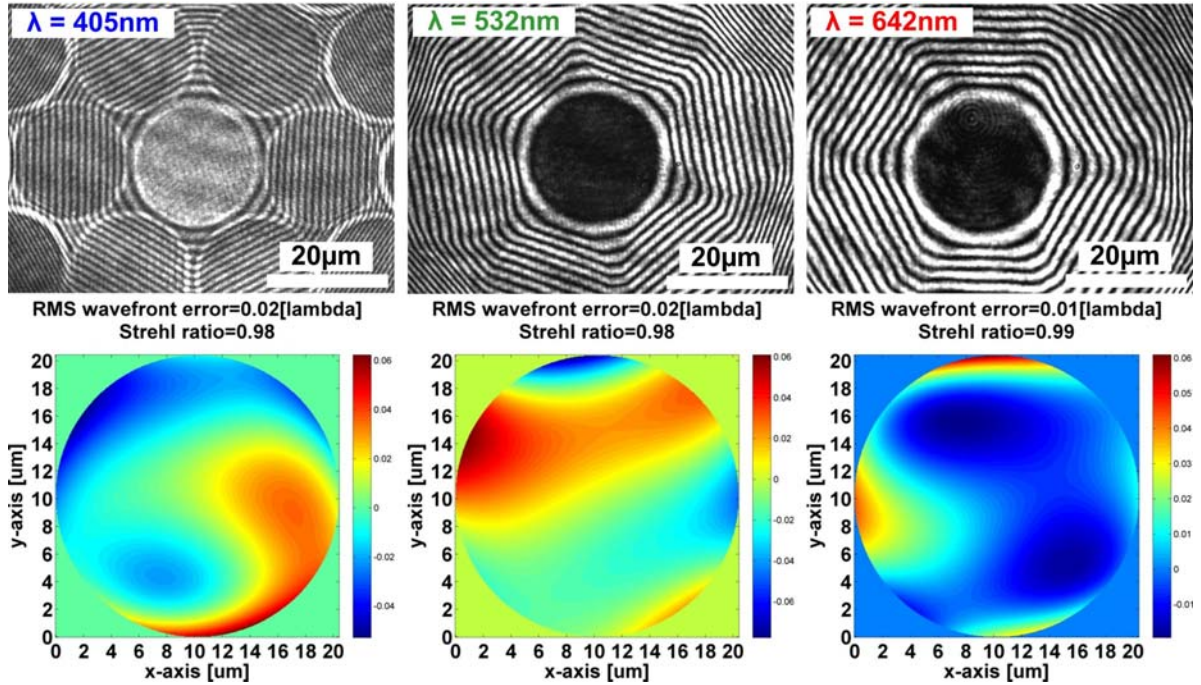
Fig. 3.8: *Interferometric fringe images of microlens illuminated with a spherical wave through its back focus: full field view of the CCD camera (upper row) and measured wavefront deviations from a plane wave within the lens aperture (bottom row) for 405nm (left), 532nm (center), and 642nm (right).*

3.3 Conclusions

We reviewed the three functional blocks of the HRIM, which consists of an optical interferoemter with PSI, an optical microscope, and illumination block that allows to manipulate the illumination and maintain it constant during 3D scanning. First we discussed the nonimal resolution of the system, which is basically derived from Abbe's imaging theory of microscopy. We verify actual amplitude resolution of the system by comparing measuremnts of photonic nanojet with rigorous simulations. In

this way we confirmed that the HRIM works within theoretical frame work of the diffraction limit. Phase resolution of the 2D interferograms is subject to the beam quality. By measureing phase distributions of known wave generated by a diffraction-limited lens, we estimated the actual phase resolution of the HRIM as low as 0.01λ. This can vary depending on actual experimental conditions.

3.4 References

[3.1]   D. Malacara, *Optical Shop Testing* (WILEY, 2007), 3rd ed., Chap. 16.

[3.2]   M.-S. Kim, T. Scharf, and H. P. Herzig, "Amplitude and Phase Measurements of Highly Focused Light in Optical Data Storage Systems," Jpn. J. Appl. Phys. 49, 08KA03 1-5 (2010) .

[3.3]   M.-S. Kim, T. Scharf, and H. P. Herzig, "Small size microlenes characterization by Multiwavelength High Resolution Interference Microscopy," Opt. Express 18, 14319-14329 (2010).

[3.4]   C. Rockstuhl, I. Märki, T. Scharf, M. Salt, H. P. Herzig, and R. Dändliker, "High Resolution Interference Microscopy: A Tool for Probing Optical Waves in the Far-Field on a Nanometric Length Scale," Current Nanoscience 2, 337-350 (2006).

[3.5]   M. Born and E. Wolf, *Principles of Optics* (Cambridge University Press, 1999), 7th ed., Chap.8.

[3.6]   W. Singer, M. Totzeck, and H. Gross, *Handbook of Optical Systems* (Wiley, 2005) Vol. 2, Chap. 25.

[3.7]   F. Gori, G. Guattari, and C. Padovani, "Bessel-Gauss beams," Optics Comm. 64, 491-495 (1987).

[3.8]   J. Durnin, J.J. Miceli and J.H. Eberly, "Diffraction-free beams," Phys. Rev. Lett. 58, 1499-19501 (1987).

[3.9]   G. Indebetouw, "Nondiffracting optical-fields - some remarks on their analysis and synthesis," J. Opt. Soc. Am. A 6, 150-152 (1989).

[3.10] M. Born and E. Wolf, *Principles of Optics* (Cambridge University Press, 1999), 7th ed., Chap. 9.

[3.11] E. Abbe, "Beiträge zur Theorie des Mikroskops und der mikroskopischen Wahrnehmung," Arch. mikrosk. Anat. Entw. Mech 9, 413–468 (1873).

[3.12] H. Köhler, "On Abbe's theory of image formation in the microscope," Optica Acta. 28, 1691-1701 (1981).

[3.13] H. Gross, H. Zugge, M. Peschka, and F. Blechinger, *Handbook of Optical Systems* (Wiley, 2007) Vol. 3, Chap. 30.

[3.14] D. Brocksch, "Ernst Abbe," Innovation, The Magazine form Carl Zeiss 15, 4-7 (2005).

[3.15] A. Heifetz, S.-C. Kong, A. V. Sahakian, A. Taflove, and V. Backman, "Photonic Nanojets," J. Comput. Theor. Nanosci. 6, 1979-1992 (2009).

[3.16] C. Rockstuhl, M. Salt, and H. P. Herzig, "Theoretical and experimental investigation of phase singularities generated by optical micro- and nano-structures," J. Opt. A: Pure Appl. Opt. 6, S271 (2004).

26

Chapter 3. High-resolution interference microscopy

CHAPTER 4

Auxiliary functions of HRIM

In chapter 3, we have reviewed the principle experimental setup and the performances of a high-resolution interference microscope (HRIM). The full potential of the HRIM can be explored when additional functions are applied to meet the correct experimental conditions for each problem under investigation. Although the auxiliary functions discussed in this chapter by themselves are not new, they are not often used in optical interferometry or holographic microscopy due to a lack of flexibilies in conventional instruments.

4.1 Multiple wavelengths for light source

The characteristics of optical elements strongly depend on the operation wavelength. Here, we do not consider nonlinear effects or resonant phenomena, but take general spectral dependency into account. As a wavelength-dependant refractive index causes different colors to refract at different angles, refractive elements like lenses show different behavior mainly due to the dispersion of light. Diffractive elements, such as diffraction gratings, also demonstrate such chromatic behaviors, which are anticipated by the diffraction formular for the grating at normal incidence

$$\sin \theta_m = \frac{m\lambda}{\Lambda},$$
(4.1)

where θ is the diffraction angle, m is the diffraction order, and Λ is the period of a grating. In order to investigate wavelength dependencies in the visible spectrum, we equip the HRIM with light sources of three representative colors of visible light, red at 642 nm, green at 532 nm, and blue at 405 nm. Please note that the goal is not a spectroscopic investigation, but a general study of chromatic behaviours.

A typical case of chromatic effects appears in refractive focusing at different wavelengths. An example of a multiple-wavelength measurement for a microlens with a diameter of 20 μm is given in Fig. 4.1.
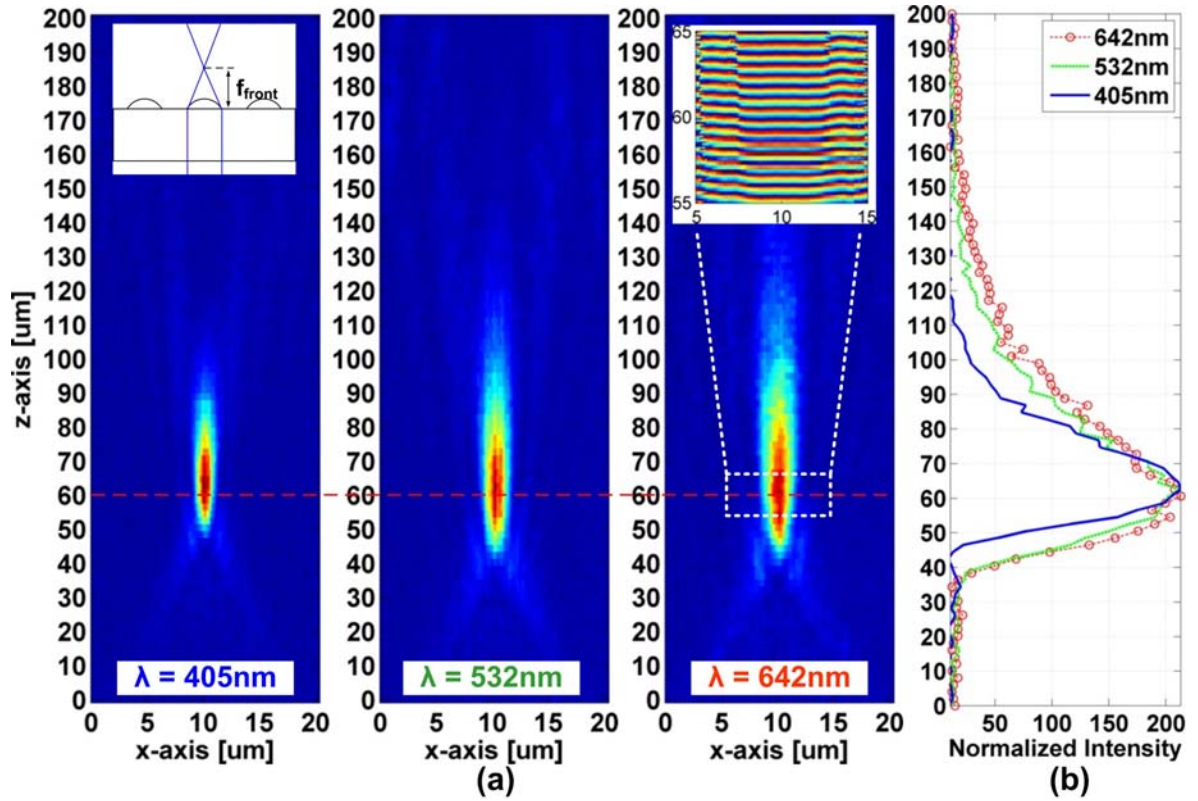

Fig. 4.1: *Measured 3D intensity distributions of the front focus of a 20-μm microlens under plane-wave illumination: (a) the x-z slices for 405 nm (left), for 532 nm (center), and for 642 nm (right) and (b) on-axis intensity profiles for three wavelengths. The substrate surface and the lens rim are located at 0 μm on the z-axis. The experimental geometry of the front focus of a microlens is illustrated in the inset of the 405 nm intensity map. A typical phase measurement is displayed in the inset of the 642 nm intensity map.*

The 3D intensity measurements of the focal spots demonstrate typical chromatic characteristics at the focus. The spot sizes in the transverse and longitudinal directions differ depending on the applied wavelength. Details of the measured sample and experimental geometries are reported in our previous work [4.1].

Chromatic effects on diffractive phenomenon by gratings will be discussed in chapter 7.

4.2 Object space in immersion

In light microscopy, liquid or solid immersion is a technique used to increase the resolution of a microscope. This is generally achieved by filling the space between the objective lens and the specimen with a transparent medium. The HRIM adopts a liquid immersion technique not only to increase the resolution of the system but also to avoid unwanted aberrations when the plane of interest is imbedded in a substrate for particular cases. For example, it is hard to obtain free-standing small-size optical structures, thus they are often fabricated or deposited on a substrate for convenience. One side of the working space of such small samples is often found in the substrate and the substrate would cause aberrations or the plane of interest would not be accessible.

Let's see the example of a small-size microlens. When the size of a lens is small compared to the thickness of the substrate the back focal point often stays in the substrate. In this case we encounter undesired aberrations due to the substrate. We consider two situations. One is illuminating through the substrate and measuring the quality of the back focal point by the spherical-wave test scheme. The other is observing through the substrate for measuring the 3D point spread function of the back focus that stays in the substrate.

4.2.1 Illumination space

We start our discussion with the problems that appear for proper illumination. Wavefront aberrations and optical quality of microlenses are tested by a standard spherical-wave illumination scheme as illustrated in Fig. 4.2(a). If the focal point stays inside the substrate, refraction at the interface between air and the bottom substrate surface causes aberrations of the illumination beam as shown in Fig. 4.2(b). In immersion, which immerses the space between the illuminating objective and the substrate, refraction and resultant aberrations are avoided as shown in Fig. 4.2(c). The influence of such effect becomes significant when the NA of the lens under test is large and the substrate is thick. An example of such situation is presented in Fig. 4.3. Two measurements for the same lens are shown. Figure 4.3(a) is performed in the test geometry like in Fig. 4.2(b) and Fig. 4.3(b) in immersion where the influence of refraction at the substrate surface is eliminated. The fringe images already show severe differences and justify the use of the immersion technique. For high quality measurements it is therefore essential to avoid aberrations caused by the substrates.
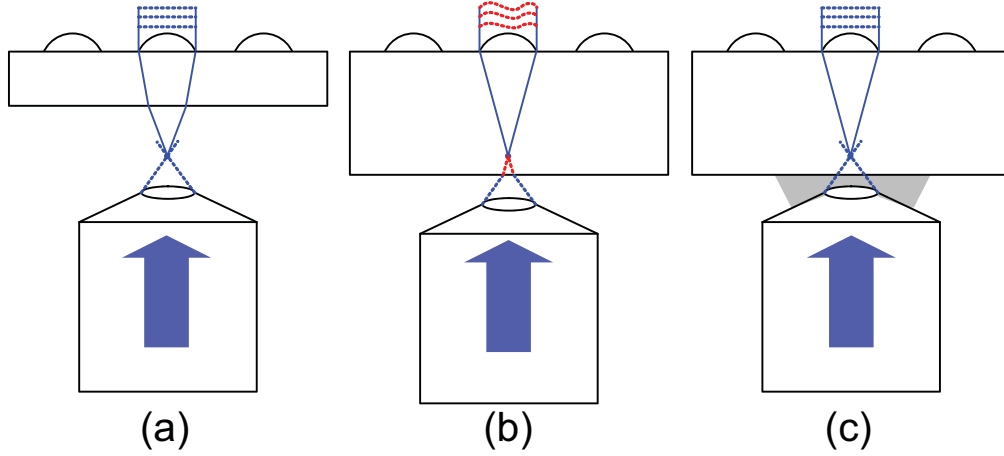
Fig. 4.2: *Lens test scheme with a spherical-wave illumination: a lens converts an incoming spherical wave into a plane wave. (a) The back focus of a microlens stays outside the substrate, (b) the back focus stays inside the substrate and refraction at the bottom surface causes aberrations. (c) The immersion in the illumination suppresses refraction at the lower substrate surface.*
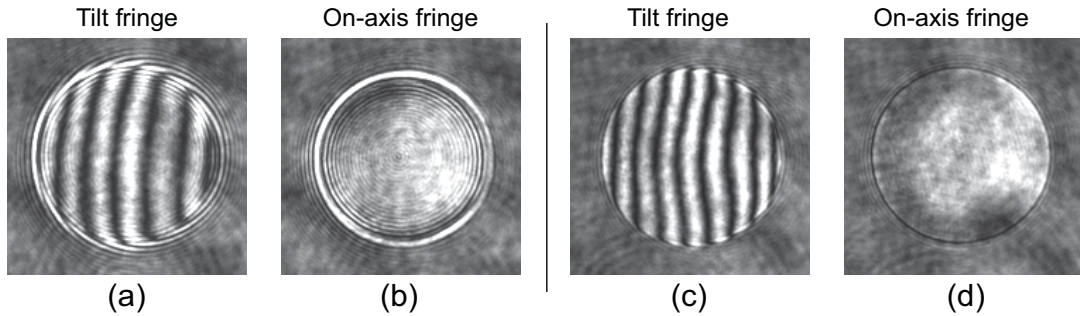

Fig. 4.3: *Example to show the influence of immersion of the illumination space. The sample lens has a diameter of 62 µm, an NA of 0.43 and a back focal length of 100 µm, which stays in the glass substrate of 170 µm thickness. Spherical wave illumination of 642 nm is generated by a 100X / NA 0.9 dry objective in (a) a tilt fringe and (b) an on-axis fringe [Fig. 4.2(b)] and by a 100X / NA of 1.4 oil immersion objective in (c) a tilt fringe and (d) an on-axis fringe [Fig. 4.2(c)].*

4.2.2 Observation space

R. Hooke first discussed the immersion technique to improve the imaging performance of microscopy in 1678 [4.2]. The concept of *homogeneous immersion* had preceded Abbe's pioneering works of oil immersion objectives. However, he constructed the first oil-immersion lens when establishing the imaging theory of microscopy [4.3]. For homogeneous immersion, oil serves as a perfect index matching medium, so that complete homogeneity is obtained. Immersion microscopy generally immerses the space between the objective and the sample in

order to improve the imaging resolution when the object is imbedded in high index medium. Immersion technique equipped in the HRIM finally leads to better measurements not only for the amplitude and but also for the phase of light fields.

4.3 Fourier plane filtering

Spatial filtering and the Fourier plane manipulation play an important role not only in image processing but also in understanding fundamental optics. Abbe pioneered the manipulation of the Fourier plane in order to investigate the image formation of microscopy [4.4]. He created various diffraction experiments and tried to monitor and manipulate the back focal plane of the objective, which is its Fourier plane. Since objectives of his time were not infinity corrected, the removal of the eyepiece and the use of an auxiliary lens permitted the observation of the back focal plane. By such experiments with a series of diffraction gratings, he succeeded in deriving the theory of image formation and the resolution limit of microscopy [4.5, 4.6]. When diffraction elements are under investigation, monitoring and manipulation of the Fourier plane are still an interesting approach. To do so a so-called Bertrand lens or a phase telescope is applied.

Recent optical microscopes are equipped with infinity-corrected objectives and a corresponding tube lens. Depending on models and makers of the microscope, there are generally two options to place an optical component to image the back focal plane. One is to insert it after the tube lens and the other is placing it between the objective and the tube lens. The HRIM employs an intermediate type Bertrand lens (Leica Microsystem) as shown in Fig. 4.4, which is designed to be inserted in between the objective and the tube lens. Integrated diaphragm in the back focal plane of the objective can cut off the higher orders from the rim of the aperture to the optical axis. We insert an additional obstruction disc at the exit pupil plane of the objective to filter diffraction orders arbitrarily. By observing the back focal plane as shown in the insets of Fig. 4.4, which show for three different wavelengths how many diffraction orders of a 2-μm period amplitude grating are collected by the used objective, we can assure which diffraction orders are collected and filtered.

When the filtering by a diaphragm and/or a obstruction disc is not applied, the collected diffraction orders are five (0, ±1, ±2), seven (0, ±1, ±2, ±3), and nine (0, ±1, ±2, ±3, ±4) for 642 nm, 532 nm, and 405 nm illuminations, respectively. Applications of such filterings to the fine amplitude gratings and the details of the experimental arrangements will be discussed in chapter 7.
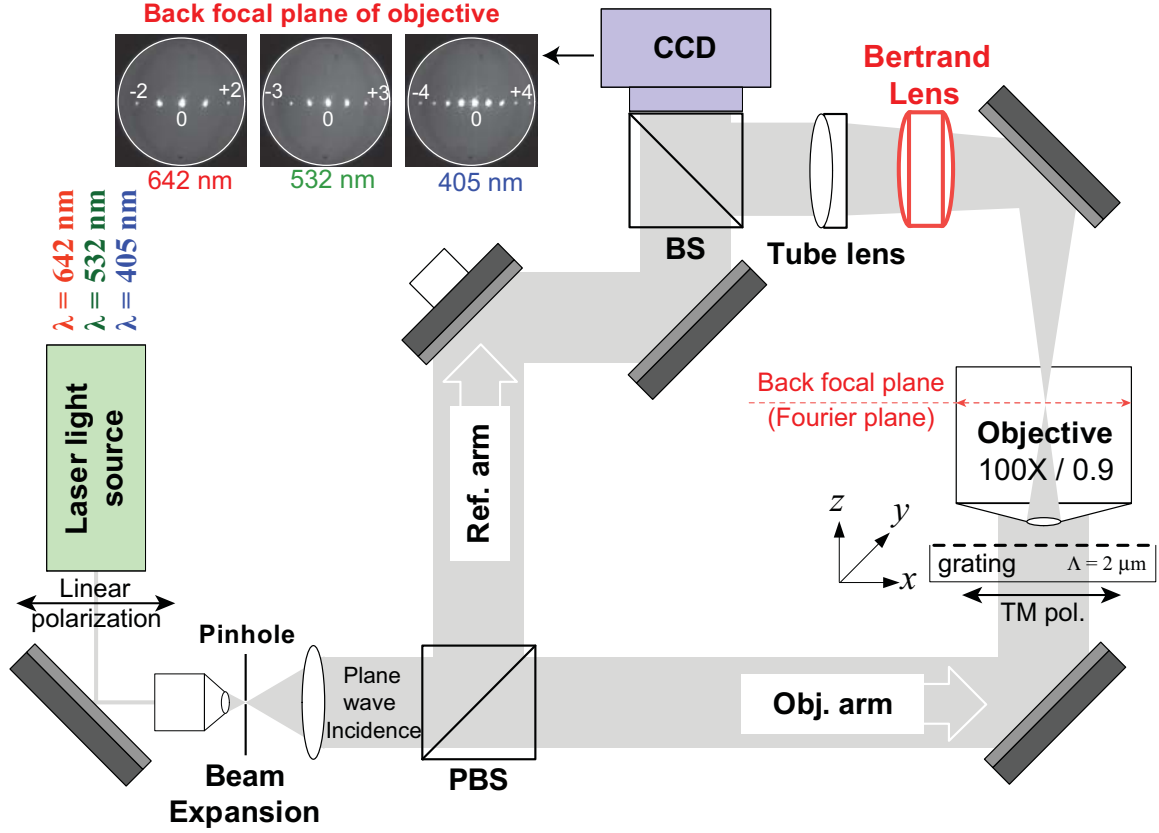
Fig. 4.4: *Schematic of the HRIM with the usage of a Bertrand lens, which images the back focal plane of the objective (Fourier plane). Images of the back focal plane are presented in the insets when a 2-μm amplitude grating is illuminated by a plane wave of three different wavelengths (642 nm, 532 nm, and 405 nm).*

4.4 Differential mode and propagation mode

The scanning of the sample along the optical axis leads to two particular observation conditions depending on the immersion medium, oil or air. The optical arrangement of the Mach-Zehnder interferometer for the HRIM is redrawn in Fig. 4.5(a). When oil immersion is applied, as depicted in Fig. 4.5(b), the scanning of the sample in position with respect to the observation objective leads to an effective variation of the optical path length (OPL) in the object arm as

$$\Delta OPL = (n_{upper} - n_{lower}) \cdot l \,, \tag{4.2}$$

where *l* is the scanning length in the z-axis and *n* is the refractive index of the indicated medium in Figs 4.5(b) and 4.5(c). Such variation of the optical path lengths causes a modulation along the optical axis, which allows to record 3D phase

data as light propagates. We call this observation mode "propagation mode". Note that the axial modulation period by *ΔOPL* is inversely proportional to the index difference $(n_{upper} - n_{lower})$, which is generally about 2 times larger than the operation wavelength for the oil ($n = 1.5$) immersion case.
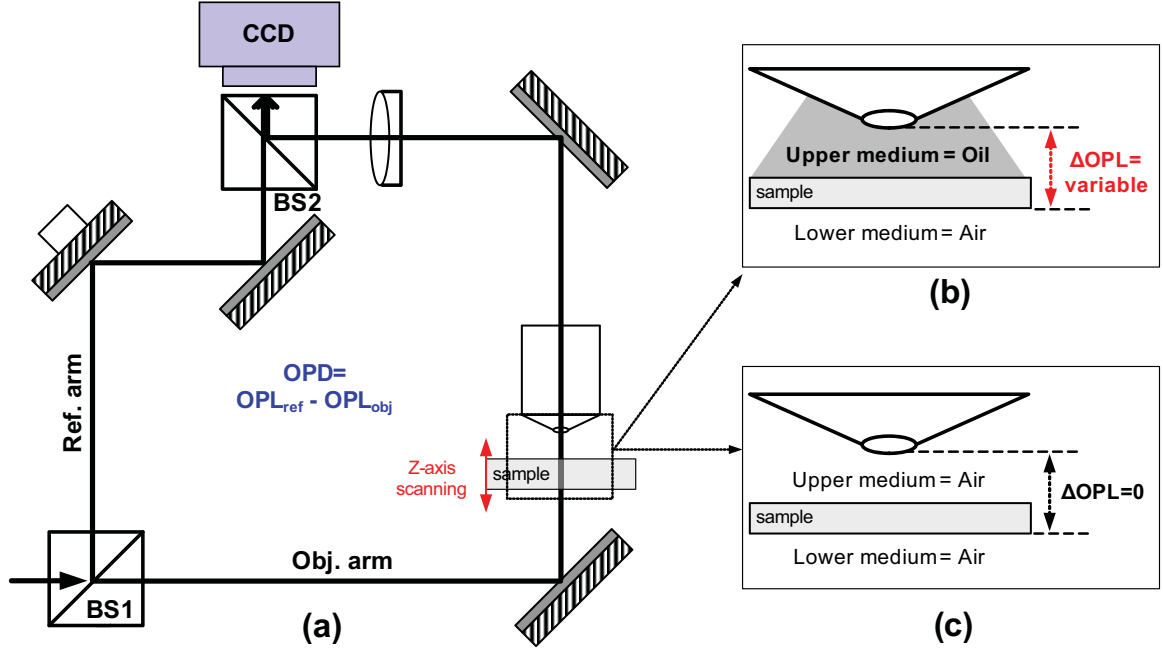

Fig. 4.5: *(a) Simplified schematic of the HRIM and close-up diagrams of the observation space (b) in oil and (c) in air. During the z-axis (optical axis) scanning of the sample, the optical path length (OPL) is variable for (b) and constant for (c).*

When the object space is in air, as in Fig. 4.5(c), the optical path difference does not change during the 3D scanning since the optical path of such an interferometer is constant, *i.e.*, the variation of the OPL is zero. This is because the difference of the refractive indices above and below the sample stays zero even though the sample is moved. In this way, differential interferometry in longitudinal direction can be realized. We call such an observation condition "differential mode". Applications to the highly confined light fields will be discussed in following chapters from 5 to 8.

4.5 Manipulation of incident polarization

An additional degree of freedom for the illumination control in the HRIM, which has already been mentioned in the section 3.1.3, is polarization. Polarization modifying elements like wave plates or polarization converters change an incident polarization to a specific output state of polarization. For example, a liquid-crystal (LC) polarization converter can transform linear into radial or azimuthal polarization

Chapter 4. Auxiliary functions of HRIM

[4.7]. Even though there exists interferometry with a radial or azimuthal polarization, which is termed *spiral interferometry* [4.8], this polarization engineering is applied only to the amplitude measurements of the beam-shaping of the photonic nanojet spots in chapter 9 rather than for the phase measurements. In the object arm of the HRIM a LC radial polarization converter (ARCoptix S.A.) can be inserted as illustrated in Fig. 4.6. With such a component, a doughnut-shape focal spot can be produced when an azimuthal polarization is created due to nonexistence of the longitudinal field component [4.9].
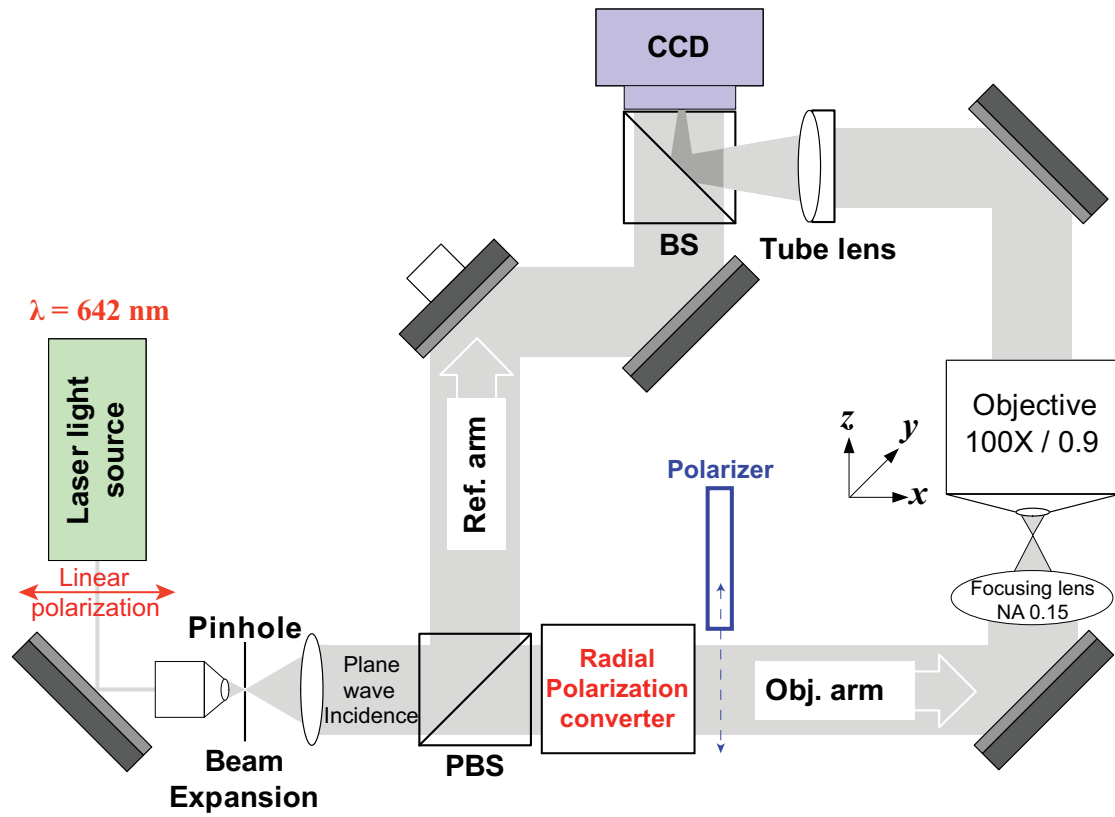

Fig. 4.6: *Schematic of HRIM with the usage of additional polarization controllers in the object arm of the interferometer. A polarizer can be inserted when decomposition of the polarization becomes necessary.*

As an example, a measured focal spot by a low NA (0.15) lens of an azimuthally polarized beam is shown in Fig. 4.7(a). It shows a typical doughnut like intensity distribution in the focal plane. When such polarization beam passes through a linear polarizer set just before the focusing lens, decomposition leads to linear separation of the spot by an extinction line parallel or vertical to the axis of the polarizer. Typically, two-half-lobes spots are formed [4.10]. They are shown in Figs. 4.7(b) and 4.7(c) for the polarizer parallel to the *x*- and the *y*-axes, respectively. The application of this polarization-induced beam shaping will be discussed in chapter 9.
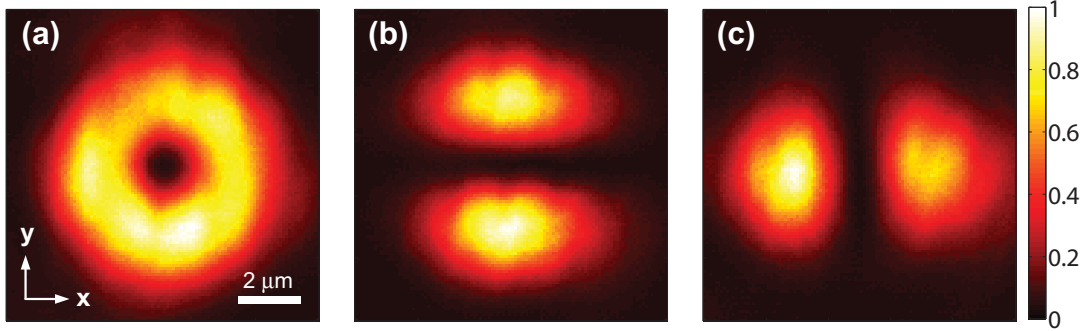
Fig. 4.7: *Measured intensity in the focal plane of a low NA (0.15) lens focusing an azimuthally polarized beam with and without an additional polarizer: (a) without a polarizer a typically doughnut shape intensity appears, (b) with a polarizer parallel to the x-axis, and (c) with a polarizer parallel to the y-axis symmetric intensity lobs are observed. The image size is 10 x 10 μm². Intensities are all normalized.*

4.6 Conclusions

The HRIM can be upgraded with several auxiliary techniques of conventional microscopy. First, our instrument is equipped with red, green, and blue laser sources to cover the visible spectrum for the study of the spectral dependency. The possibility to work in immersion allows higher resolution and moreover avoids measurement related aberrations during the characterization when observation and illumination are done through a substrate. We demonstrated the characteristic features of such upgrades by using small-size microlens as a test object.

More auxiliary functions are added, whose applications will be discussed in following chapters, as summarized below:

- Monitoring and manipulating the back focal plane (Fourier plane) of the objective are still interesting approach to investigate diffractive elements, such as gratings. By help of a Bertrand lens, the HRIM is able to reach the Fourier plane and manipulate diffraction orders in the desired manner in order to investigate roles of each diffracted order in the Fresnel diffraction (near-field diffraction) regime including non-paraxial orders.

- The immersion medium causes an optical path length modulation of the interferometer during the scanning of the sample along the optical axis. A special observation mode can be set up called a propagation mode. In air, differential interferometric measurements along the longitudinal direction are obtainable due to the constant OPD during the scanning. They are particularly interesting to visualize axial phase evolutions, such as the Gouy phase shift [4.11] or other kind of the phase anomaly.

- To creat illumination beams with a specific shape and a finite size, the polarization engineering technique has been equipped in the HRIM. The size of the beam spot is in general controllable by the NA of the focusing lens.

4.7 References

[4.1]   M.-S. Kim, T. Scharf, and H. P. Herzig, "Small size microlenes characterization by multiwavelength high-resolution interference microscopy," Opt. Express **18**, 14319-14329 (2010).
[4.2]   R. Hooke, Lectures and Collections; Microscopium (Royal Society, London 1978).
[4.3]   E. Abbe, "On New Methods for Improving Spherical Correction applied to the Construction of Wide-angled Object-glasses," Journal of the Royal Microscopical Society **2**, 812-824 (1879).
[4.4]   J. W. Goodman, *Introduction to Fourier Optics* (Roberts & Company, 2005), 3rd ed., Chap. 6.
[4.5]   H. Gundlach, "From the History of Microscopy: Abbe's Diffractrion Trials," Innovation, The Magazine form Carl Zeiss **15**, 18-23 (2005).
[4.6]   H. Köhler, "On Abbe's theory of image formation in the microscope," Optica Acta. **28**, 1691-1701 (1981).
[4.7]   M. Stalder and M. Schadt, "Linearly polarized light with axial symmetry generated by liquid-crystal polarization converters," Opt. Lett. **21**, 1948-1951 (1996).
[4.8]   S. Fürhapter, A. Jesacher, S. Bernet, and M. Ritsch-Marte, "Spiral interferometry," Opt. Lett. 30, 1953-1955 (2005).
[4.9]   R. Dorn, S. Quabis, and G. Leuchs, "Sharper focus for a radially polarized light beam," Phys. Rev. Lett. **91**, 233901 (2003).
[4.10] Q. Zhan, "Cylindrical vector beams: from mathematical concepts to applications," Adv. Opt. Photon. **1**, 1-57 (2009).
[4.11] L. G. Gouy, "Sur une propriété nouvelle des ondes lumineuses," C. R. Hebd. Seances Acad. Sci. **110**, 1251 (1890).

CHAPTER 5

Refractive confinement of light by a lens

Light bending at an interface, refraction, is the working principal of a lens, which has been served as a tool for the energy concentration for more than 3000 years [5.1]. In the past, such confinement has been weak due to the lack of the technology. In other words, high NA and high quality lenses were not available. Recent approaches pursue high confinements of light and the advances in technologies now allow us to exceed the NA of a lens by even larger than 2 by solid immersion [5.2]. Among numerous studies for highly focused beams [5.3-5.5], theoretical works have been main research actvities because laboratory experiments are generally limited by the resolution of the measurement system. Even though experimental arrangements are realized, phase measurements are often excluded. Investigations without phase measurements are not fully satisfying the theoretical counter parts, which are generally represented by amplitude and phase features. In this chapter, we experimentally investigate highly focused beams with numerical apertures up to 1.4. The high-resolution amplitude and phase distributions are measured by the HRIM and influences of the variation of the NA on both, the illumination and observation sides are discussed.

5.1 Focused Gaussian beam

As long as we use a laser light source, even if the width of the normal distribution is extremely large, a collimated beam demonstrates a Gaussian intensity distribution. For relatively large beam spots, such a collimated beam is readily considered as a

plane wave in experiments due to its plane wavefronts within the finite experimental space. When such a plane wave emerges from the focusing lens, the field distribution of the focused light will be slightly different from the ideal plane wave case. Therefore, we more realistically call the focusing of the experimental plane wave a *focused Gaussian beam*.

5.2 Focused beam in immersion

The refractive index, which is a measure of the speed of light in a medium, is defined as the ratio between the speed of light in vacuum *c* and the speed *v* at which light travels in that medium [5.6] as:

$$n = c/v. \tag{5.1}$$

When light propagates in a homogenous dielectric (transparent) medium of higher refractive index ($n > 1$), its characteristics differ from them in air or in vacuum as the speed of light is reduced in the optically denser medium. Accordingly, the effective wavelength in the medium is shortened proportional to the refractive index of the medium *n*:

$$\lambda_{medium} = \lambda/n, \tag{5.2}$$

where λ is the vacuum wavelength. However, the frequency of light υ is unchanged because this has its original characteristic written as

$$\upsilon = c/\lambda. \tag{5.3}$$

As anticipated by Eq. (1.2) [$NA = n \cdot sin\theta$], the NA of the objective is directly proportional to the refractive index *n* of the medium between the sample and the front lens of the objective and the sine of one half of the angular aperture of the objective. Since the half angle cannot exceed 90°, the maximum possible numerical aperture is determined by the refractive index of the immersion medium. In practice, the maximum NA of a dry objective is limited to 0.95, and greater values can only be achieved using objectives designed for immersion media. For example, immersion in oil leads to NA = 1.4 and in water to NA = 1.2.

5.3 Experimental geometry

We set the experimental arrangements by using highest NA with commercially available oil immersion objectives from Leica microsystems. We equip the HRIM with two identical oil immersion objectives of 100X / NA 0.7-1.4 (HC

X APO) for both spot creation and observation. A schematic is illustrated in Fig. 5.1. The NA of this objective is variable from 0.7 to 1.4 by a diaphragm which is positioned at its back focal plane. The incidence to the objective is an experimental plane wave of 642 nm wavelength.
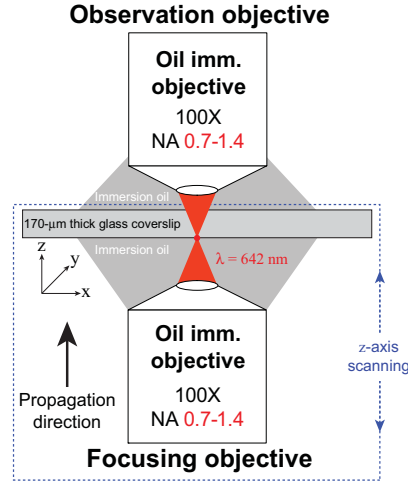

Fig. 5.1: *Experimental geometry of two identical oil immersion objectives to measure highly focused Gaussian beams in immersion. An experimental plane wave of 642 nm propagates in +z direction and two objectives are aligned in confocal position. The NA of the objective is variable from 0.7 to 1.4.*

We immerse the space between two immersion lenses with standard immersion oil and use a glass coverslip of 170-µm thickness in between. First, the focal plane of the focusing lens is set to the bottom surface of the glass coverslip. Then, we bring the focus of the observation objective to the focal position of the focusing lens (at the bottom of the glass coverslip). Now these two objective lenses are in a confocal situation. 3D measurements are realized by scanning the focusing lens together with the glass cover slip, which is depicted in a blue dotted square of Fig. 5.1. As we apply the immersion objective to the experiments, the phase distributions are measured in the propagation mode because of OPD modulation above the cover slip [see chapter 4, section 4.4]. Please note that the period of the axial modulation is approximately two times that of the operation wavelength as explained in the section 4.4.

5.4 Measured amplitude and phase distbributions

Varying the NA of the objective for focusing and/or for observing, will be applied to demonstrate how the NA influences on the field distributions near the focus. We create four experimental situations for the variation of the NA:

- NA = 0.7 for focusing *vs* NA = 0.7 for observing,

- NA = 0.7 for focusing *vs* NA = 1.4 for observing,

- NA = 1.4 for focusing *vs* NA = 0.7 for observing,

- NA = 1.4 for focusing *vs* NA = 1.4 for observing.

The *x-y* and *x-z* slices throught the peak intensity point of the measured 3D data are presented in Fig. 5.2.
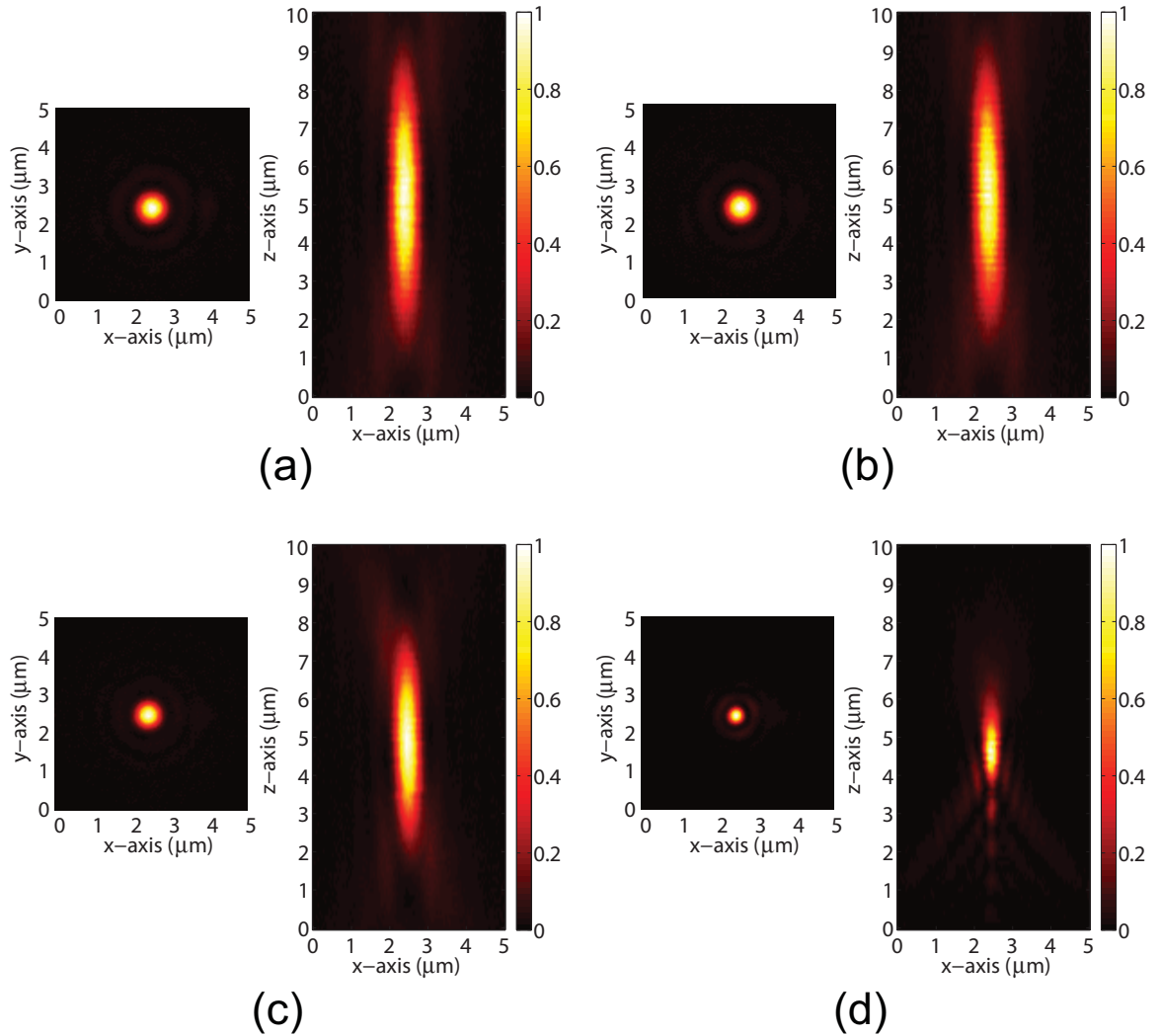

Fig. 5.2: *The x-y and x-z slices through the peak intensity point of measured 3D data: (a) NA 0.7 focusing vs NA 0.7 observing, (b) NA 0.7 focusing vs NA 1.4 observing, (c) NA 1.4 focusing vs NA 0.7 observing, and (d) NA 1.4 focusing vs NA 1.4 observing. Intensities are all normalized. The image sizes are 5 x 5 μm² (x-y) and 5 x 10 μm² (x-z).*

Figures 5.2(a) and 5.2(b) show almost the same results. For the same test object (let's say the NA 0.7 focal spot), an increase of the resolution of the observation lens does not lead to more details. In other words, when the test object is unchanged, the high NA system can measure it more precisely, but the results do not reveal more details because there are none. The third case, NA 1.4 focusing and NA 0.7 observation in Fig. 5.2(c), reveals different results compared to the former two cases. The spot sizes in the *x-y* directions are found 15% smaller than the former cases. We assume that the non-identical experimental situations in focusing and observing led to such discrepancy even if two identical objectives are used in this experiment. The last situation has been assigned to use the maximum NA for both focusing and observation, *i.e.*, NA = 1.4. As we expect, a relatively smal spot is observed as shown in Fig. 5.2(d). The measured FWHM spot sizes in the *x*-and *y*-directions are 306 nm, 295 nm, respectively. The theoretical FWHM spot size is calculated to be 280 nm as the half of the Airy disc size calculated as

$$Airy\ disc\ size = 1.22 \frac{\lambda}{NA}\,, \tag{5.4}$$

when NA = 1.4 and λ = 642 nm. For NA = 1.4 in Fig. 5.2(d), the *x-z* intensity disbribution reveals longitudinal asymmetry. We presume that experimental errors cause spherical aberrations, which generally lead to larger focal spots for both focusing and measuring situations. Moreover, high-NA focusing suffers in general much more from spherical aberrations in its longitudinal distribution, proven by the asymmetry in Fig. 5.3.
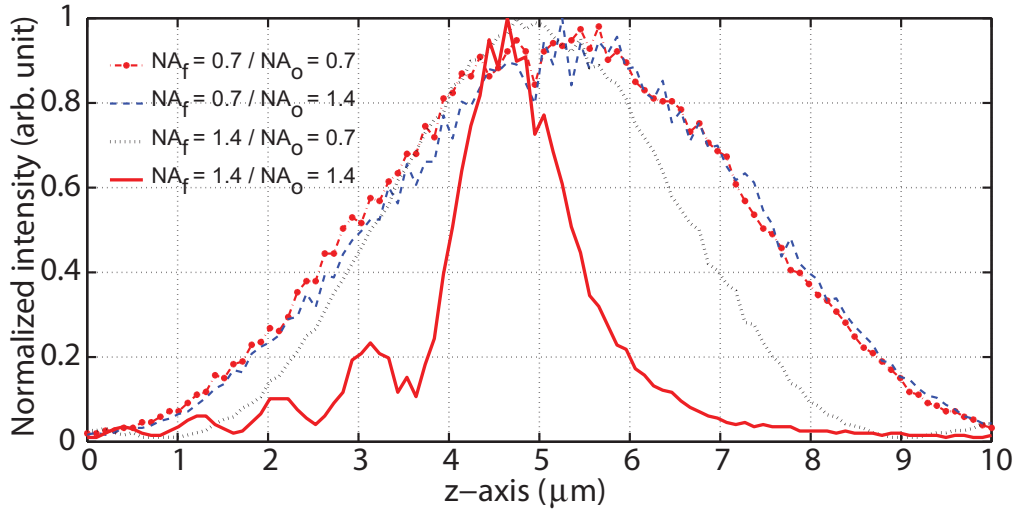

Fig. 5.3: *The longitudinal intensity profiles along the optical aixs (z-axis): red dashed line with a point for NA 0.7 focusing vs NA 0.7 observing, blue dashed line for NA 0.7 focusing vs NA 1.4 observing, black dotted line NA 1.4 focusing vs NA 0.7 observing, and red solid line for NA 1.4 focusing vs NA 1.4 observing. Intensities are all normalized.*

In Fig. 5.3, we can measure the longitudinal spot size as *Rayleight unit* [5.7], within which the peak intensity has decreased to 80%. This is also called the depth of focus given by Eq. (3.2) [$\Delta z = n \cdot \lambda / NA^2$]. The experimental and theoretical *x-, y-,* and *z*-direction pot sizes are summarized in Table. 5.1.

Table 5.1: *Summary of the experimental and theoretical spot sizes.*

	$NA_f = 0.7$ $NA_o = 0.7$	$NA_f = 0.7$ $NA_o = 1.4$	$NA_f = 1.4$ $NA_o = 0.7$	$NA_f = 1.4$ $NA_o = 1.4$
Exp. FWHM spot size (*x*-axis)	579 nm	585 nm	499 nm	306 nm
Exp. FWHM spot size (*y*-axis)	561 nm	569 nm	481 nm	295 nm
*Half of Airy disc size	560 nm	560 nm	560 nm	280 nm
Exp. Rayleigh unit (*z*-axis)	2.5 μm	2.3 μm	2 μm	606 nm
*Rayleight unit [**Eq. (3.2)]	1.96 μm	1.96 μm	1.96 μm	491 nm
Exp. size of Airy disc (*x*-axis)	1.3 μm	1.25 μm	1.15 μm	720 nm
Exp. size of Airy disc (*y*-axis)	1.2 μm	1.2 μm	1.1 μm	620 nm
*Airy disc size [Eq. (5.4)]	1.12 μm	1.12 μm	1.12 μm	560 nm

* The hlaf of Ariy disc size are calculated by taking the half value of Eq. (5.4) for the minimum NA of the system (either the NA of the focusing lens or of the observing lens).

** The Rayleigh unit is calculated with $n = 1.5$ for oil immersion by Eq. (3.2).

Intensity measurements of such highly focused beams are a rather conventional approach and only shape and size of the focal spot can be found. The crucial information of propagation of light is hidden in the phase, which represents snapshots of wavefronts and how light evolves during propagation. Under the same experimental conditions the phase distributions are measured and the results are shown in Fig. 5.4. The *x-y* slices are taken through the plane containing the phase singularities, at which the wavefronts stay plane between converging and diverging spherical wavefronts. The *x-z* slices are extracted through the center of the Airy disc, which is presented as a central iso-phase disc in the *x-y* slice.

As the lens focuses an incoming plane wave, light converges toward the focus with a form of a spherical wave. This is clearly visible in the bottom half of the longitudinal phase distributions of Fig. 5.4 for each measurement. In the focal plane, which is licated in the middle of the longitudinal map, spherical wavefronts are converted to a plane wavefront just before diverging. In the focal plane, the stereotype phase image of the focal spot, *i.e.,* the Airy pattern is formed. Compared

to the transverse intensity distributions in Fig. 5.2, the transverse phase distributions clearly illustrate not only the central Airy disc but also the side lobes of the Airy pattern. The lateral extension of the central iso-phase disc represnets the size of the Airy disc that can be calculated by Eq. (5.4). The data analysis of the Airy disc sizes is included in the bottom of Table 5.1.
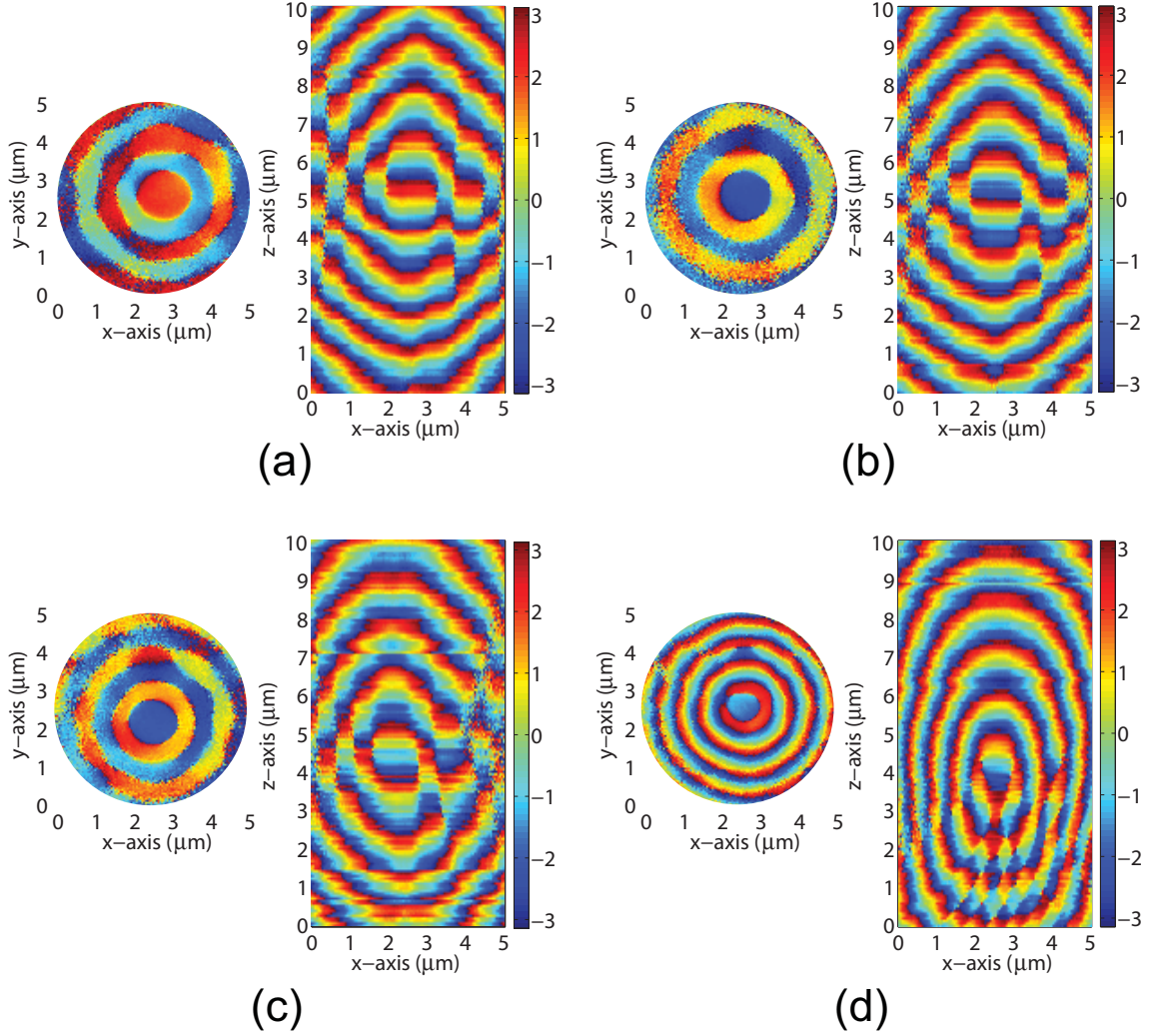

Fig. 5.4: *The x-y and x-z slices of measured 3D phase distributions: (a) NA 0.7 focusing vs NA 0.7 observing, (b) NA 0.7 focusing vs NA 1.4 observing, (c) NA 1.4 focusing vs NA 0.7 observing, and (d) NA 1.4 focusing vs NA 1.4 observing. The image sizes are 5 x 5 μm² (x-y) and 5 x 10 μm² (x-z).*

The Airy function that describes the intensity in the focal spot has several dark rings where its amplitude falls to zero. The rings have different phases and there is a π-phase jump between adjacent Airy patterns. Such phase jumps are explained as phase singularities or dislocations [5.8, 5.9]. In our experiments singularities appear

near the center of the plane phase island in the middle of the *x-z* phase distributions of Fig. 5.4. Because of the experimental errors and noises, the exact value of π shift is difficult to measure, but the evolution of phase along the propagation axis gives intuitive impression of how wavefronts evolve and the Airy pattern is formed at the focal plane. When the overall aberrations of the system are negligible the converging space and diverging space are symmetrically separated by the focal plane, where the Airy pattern is embedded, and show identical spherical wavefronts with opposite sign of curvature as presented in Figs. 5.4(a) - 5.4(c). When spherical aberrations affect the fields near the focus like the situation in Fig. 5.4(d), the phase distributions are perturbed as demonstrated in the bottom half of the longitudinal phase map. The ripples in the wavefronts correspond to strong intensity fields of side lobes appearing in the bottom half of the longitudinal intensity map [see Fig. 5.2(d)].

5.5 Conclusions

The classical way of light confinement, refractive focusing, has been studied by measuring the amplitude and phase distributions in real 3D space near the focus by the HRIM. The highest available liquid immersion system, such as NA 1.4 in oil immersion, was applied to generate a focus of 300-nm FWHM spot size. We investigated the influence of the NA variation on the focusing and observing objectives. As expected, the NA equivalently limits the resolution in all cases. When the NA of the observing lens is larger than the NA of the object (in our case, a focued Gaussian beam), the measurement system can resolve the object. For the opposite case, the response of the system relies on the NA of the observation system. From the intensity measurements, the shape and size of the focal spot are main information to be retrieved. The phase distributions show the evolution of the wavefronts, which follows the conventional concept as converging wave reaches the focal plane and diverges with opposite sign of curvature. In the focal plane, the Airy pattern is observed as separated by phase rings, where the wavefronts are retained to be plane. The central phase disc represents the Airy disc, which is surrounded by a phase singularity ring due to zero amplitude.

5.6 References

[5.1]   Wikipedia, "Nimurd lens," http://en.wikipedia.org/wiki/Nimrud_lens.
[5.2]   M. Shinoda, K. Saito, T. Kondo, M. Furuki, M. Takeda, A. Nakaoki, M. Sasaura, and K. Fujiara, "High-density near-field readout using solidimmersion lens made of KTaO$_3$ monocrystal," Jpn. J. Appl. Phys. **45**, 1332-1335 (2006).
[5.3]   J. J. Stamnes, *Waves in Focal Regions* (Taylor & Francis, 1986).

[5.4] A. Boivin and E. Wolf, "Electromagnetic Field in the Neighborhood of the Focus of a Coherent Beam," Phys. Rev. **138**, B1561-B1565 (1965).

[5.5] H. P. Urbach and S. F. Pereira, "Focused fields of given power with maximum electric field components," Phys. Rev. A **79**, 013825 (2009).

[5.6] Wikipedia, "Refractive index," http://en.wikipedia.org/wiki/Refractive_index.

[5.7] H. Gross, H. Zugge, M. Peschka, and F. Blechinger, *Handbook of Optical Systems* (Wiley, 2007) Vol. 3, Chap. 30.

[5.8] A. Boivin, J. Dow, and E. Wolf, "Energy Flow in the Neighborhood of the Focus of a Coherent Beam," J. Opt. Soc. Am. **57**, 1171-1175 (1967).

[5.9] C. Rockstuhl, I. Märki, T. Scharf, M. Salt, H. P. Herzig, and R. Dändliker, "High Resolution Interference Microscopy: A Tool for Probing Optical Waves in the Far-Field on a Nanometric Length Scale," Current Nanoscience **2**, 337-350 (2006).

Chapter 5. Refractive confinement of light

CHAPTER 6

Diffractive confinement of light by a single circular object

The wave theory of light explains how light interacts with objects, a phenomena usually called diffraction. E. Hecht tells an interesting behind story of discovery of the wave nature of light and its consequence, which is named the spot of Arago or Poisson's bright spot [6.1]:

> *In 1818 Augustin Fresnel submitted a paper on the theory of diffraction for a competition sponsored by the French Academy. His theory represented light as a wave, as opposed to a bombardment of hard little particles, which was the subject of a debate that lasted since Newton's day. Siméon Poisson, a member of the judging committee for the competition, was very critical of the wave theory of light. Using Fresnel's theory, Poisson deduced the seemingly absurd prediction that a bright spot should appear behind a circular obstruction, a prediction he felt was the last nail in the coffin for Fresnel's theory.*
>
> *However, Dominique Arago, another member of the judging committee, almost immediately verified the spot experimentally. Fresnel won the competition, and, although it may be more appropriate to call it "the Spot of Arago," the spot goes down in history with the name "Poisson's bright spot" like a curse.*

When light diffracted by an object interferes constructively in the same space by virtue of a suitably chosen geometry, symmetry, or periodicity, confinement of light in small volumes occurs. For single object the best example is the spot of Arago [6.1-6.4] that appears behind a circular obstacle (amplitude object). For periodic objects Talbot images [6.5] can be considered as a good example. All these examples are well-known results of

the constructive interference happening close to the object in the Fresnel (near-field) diffraction region. Therefore, the Fresnel diffraction theory has been widely applied to understand and simulate such phenomena [6.1-6.3]. For the theoretical studies, since the Fresnel approximation fails to represent the fields' information close to the obstacle, more precise calculations were performed by rigorous solutions [6.6-6.8]. On the other hand, photographical investigations of diffraction patterns in far field were earlier experimental approaches [6.9, 6.10]; more precise experimental studies have been followed by applying a microwave of 10 cm wavelength to the illumination [6.11], which was aimed for easier measurements of the near-field diffraction patterns, and a large-size disc to the obstacle for an optical wavelength [6.12, 6.13], which was for a short-wavelength approximation (size of obstacle >> λ) [6.7]. For small objects, non-paraxial diffracted fields, which have propagation angles over 30° with respect to the optical axis [6.2] and comparably strong intensity, become significant and a paraxial approximation is not valid anymore. High-resolution measurement techniques are therefore required to experimentally study the diffracted light fields of small objects. We demonstrate the abilities of the HRIM to study not only amplitude but also phase fields including non-paraxial fields in the Fresnel (near-field) diffraction regime of micro-structures for a single object in this chapter and for periodic objects in chapter 7.

6.1 The spot of Arago

The existence of the spot of Arago can be readily explained by the Huygens' principle [6.14]. When a plane wave illuminates a circular obstacle, *e.g,* a steel sphere or an opaque disc, every point along the circumference serves as a new point source of light as illustrated in Fig 6.1(a).
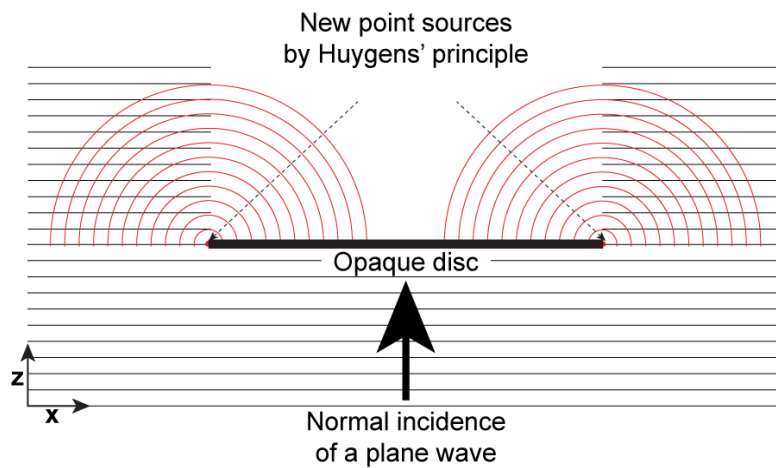

Fig. 6.1: *When an opaque disc is normally illuminated by a monochromatic plane wave, each point of the edge of the obstacle is the starting point for a new point source emitted. Black horizontal lines are a snapshot of a plane wave traveling in the +z direction and red circular lines are for a spherical wave emerging from a point source.*

One half of the light emerging from each of these secondary point sources on the circumference of the obstacle propagates towards the center of the geometric shadow of the obstacle, which travels exactly the same optical path length. Finally, all the light arrives in phase on the central line of the shadow (the optical axis) and constructively interferes as illustrated in Figs. 6.2(a) and 6.2(b). A bright spot appears in the shadow, which is a canonical proof of the wave nature of light by means of diffraction and interference. This is a very interesting phenomenon, but the potential application has survived only as a textbook curiosity [6.1-6.3] rather than a practical reality because of the low brightness (low efficiency) and poor resolution due to the smoothing effect of the rather prominent ring structure surrounding such spot [6.4].
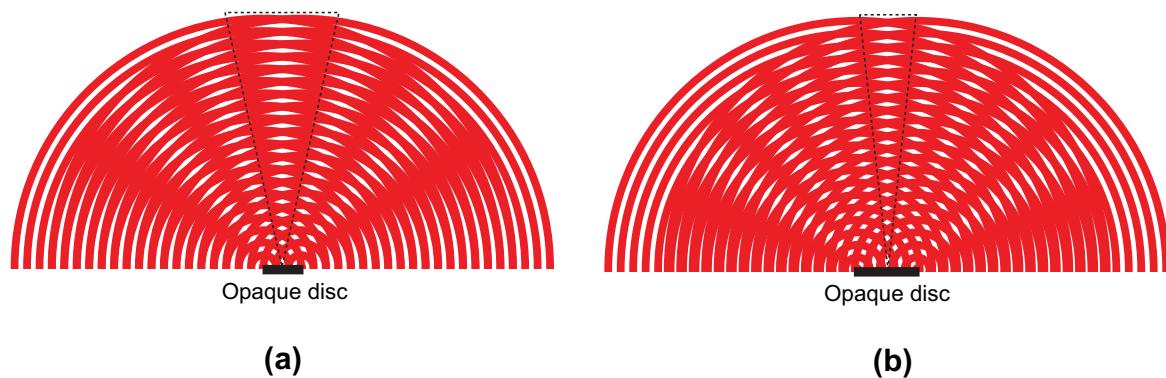

Opaque disc

(a)

Opaque disc

(b)

Fig. 6.2: *Typical two-point-source interference leads to an on-axis bright spots in the shadow of the obstacle due to the constructive interference: (a) for small disc and (b) for large disc.*

We are interested in how amplitude and phase fields are distributed just after such obstacles of only a few micrometers size. Especially we would like to investigate the axial phase evolution. To do so, the HRIM is equipped with a 100X / NA 0.9 objective to measure the longitudinal-differential phase distributions. Two sizes of objects are investigated in order to verify the influence of the size on the field distribution of the Arago spot. We present here the results from a relatively small obstacle (4-µm diameter disc) and a largeer obstacle (10-µm diameter disc).

6.2 Small obstacle: 4-µm disc

The 3D field distributions emerging for uniformly illuminated normally incident plane wave diffracted by a 4-µm metallic (150 nm thick, Cr coating) disc are measured by the HRIM. The longitudinal slices of amplitude and phase data are presented in Fig. 6.3. As anticipated, a bright spot appears in the shadow of the obstacle before it diverges like in the two-point-source interference indicated in the dashed point-down triangles of Figs. 6.2(a) and 6.2(b). Since over 100 years such intensity distributions are studied and imaged, but the axial phase evolution has never been seriously investigated. Differential phase mode [see chapter 4, section 4.4] of the HRIM allows to measure the evolution of the fields in real

space and results are shown in Fig. 6.3(b), which is recorded as a differential phase map along the propagation direction. In the phase measurements, there exists an inevitable phase drift during scanning which results in a phase drift along the scanning direction. This is mainly due to mechanical vibrations and light source instability. If the object however is small compared to the field of view, it can be safely assumed that a plane wave propagates far away from the object under investigation. Therefore, we can correct the original differential phase with respect to a plane wave far away from the opaque disc. For plane wave illumination, the differential phase far away is considered to be constant; completely independent on the position on the z-axis. Technically, an appropriate subtraction of the raw phase can easily assure this constant value. The differential phase after this correction is shown in Fig. 6.3(b). Figure 6.3(c) finally shows a phase map which is wrapped with the phase of the incident field to provide an impression of the pure phase evolution in space.
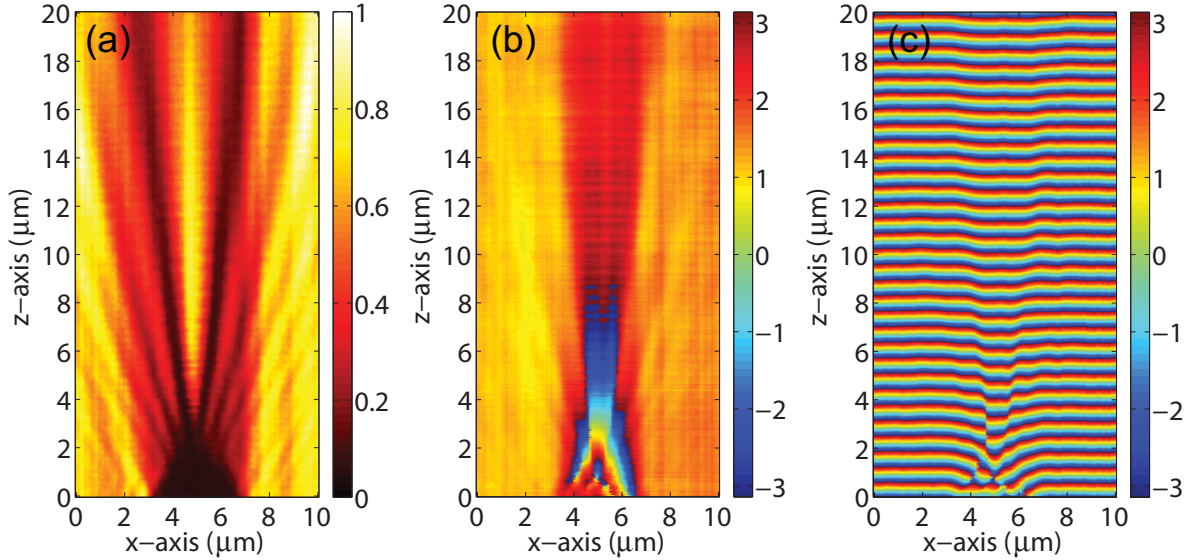

Fig. 6.3: *The longitudinal slices of the measured 3D amplitude and phase distributions of light emerging from the 4-µm diameter metallic disc. (a) Intensity map. (b) Longitudinal map of differential phase with respect to the plane wave far away from the obstacle. (c) The final wrapped phase that adds the phase advance of the plane wave to the differential phase. Intensity is normalized and the image size is 10 x 20 µm². The disc is located at z = 0 µm.*

While the intensity fields do not show much information except the existance of the bright spot, phase distributions reveal much more detailed features in spatial domain, where only some intensity is detectable, and a peculiar evolution along the optical axis. For example, in Fig. 6.3(b), we can directly observe the evolution of the phase compared to the plane wave, which is considered to be constant along the propatation direction for the differential phase map. To visualize the amount of the axial values of intensity and phase, the longitudinal (along the z-axis) profiles through the center of the disc are taken from Figs. 6.3(a) and 6.3(b) and plotted together in Fig. 6.4. The profile of the differential phase shift has been unwrapped and plotted in units of the wavelength λ (642 nm). The theoretical curve in Fig. 6.4, the on-axis phase evolution can be calculated by simply evaluate the

optical path difference (OPD) between a propagating plane wave along the *z*-direction and the diffracted waves. To do so, we consider the path difference between a ray coming from the rim of the disc with radius *r* which travels $\sqrt{r^2 + z^2}$ and the distance to the disc which is just *z*. We find the path difference as

$$OPD_{plane\,wave-diffracted\,wave} = \sqrt{r^2 + z^2} - z . \qquad (6.1)$$

At the disc surface $z = 0$ µm, Eq. (6.1) leads to the maximum phase shift, which is identical to the radius of the obstacle [6.13]. The measured axial phase shift in Fig. 6.4 shows excellent agreement with the theoretical curve.
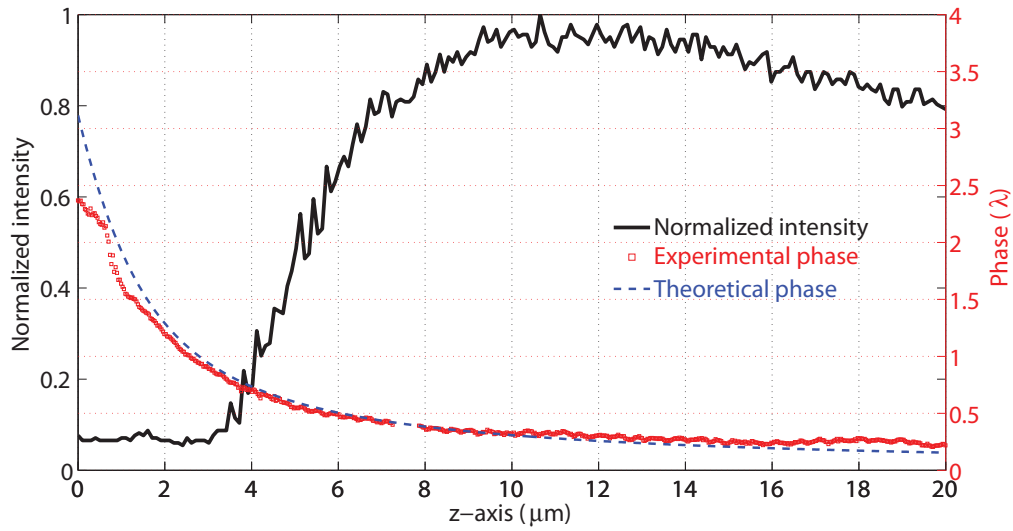

Fig. 6.4: *The axial intensity and phase profiles at the center of the disc are taken from Figs. 6.3(a) and 6.3(b). The experimental phase is unwrapped and plotted in wavelength unit. The dark solid line is the normalized intensity and the blue dashed line is the theoretical phase calculated by Eq. (6.1).*

In the axial intensity profile, an intensity maximum can be found and afterwards a very low intensity decrease due to the divergence of the Arago spot. The wrapped two dimensional phase map of Fig. 6.3(c) allows to identify more features such as phase singularity. When the on-axis axial phase shift reaches a π difference with respect to adjacent lobes or a propagating plane wave that passes far away from the obstacle, the phase singularities can occur due to destructive interference where zero amplitude is found. In Fig. 6.3 such a singularity is found at around z = 3 µm. For larger propagation distances, as can be seen in Fig. 6.4, the slope of the axial phase shift becomes very small above z = 8 µm and such effects fade out.

Please note that due to the experimental limitations, such as the NA of the observation system and the size of the object or quality of the metallic disc, the fields in the close vicinity of the object [z = 0 - 1 µm] are difficult to resolve in both intensity and phase. However, they contain no crucial information in the abovementioned analysis and

improvement of experimental conditions or rigorous numerical simulations can recover such missing information [6.6-6.8].

6.3 Large obstacle: 10-µm disc

As demonstrated in Fig. 6.2(b), the larger obstacle leads to more optical path length from the secondary point sources at the edges of the obstacle, which leads to more numerous nodes of the interference. Therefore, more complex field distributions behind the obstacle are expected for larger obstacles. While all other experimental conditions are remained the same, the diameter of the obstacle is now set to 10 µm. Figure 6.5 presents the measured 3D field distributions just after the 10-µm metallic disc when it is uniformly illuminated by a normal incidence of a monochromatic plane wave (λ = 642 nm). The longitudinal intensity map is shown in Fig. 6.5(a). The differential phase and wrapped phase maps in the *x-z* plane are shown in Figs. 6.5(b) and 6.5(c). Similar to the 4-µm disc case, the intensity map proves the existence of the bright spot in the shadow. This time there exist more side lobes around the central bright spot due to the longer path length from each edge of the disc. In other words, the more interference nodes cause the more side lobes.
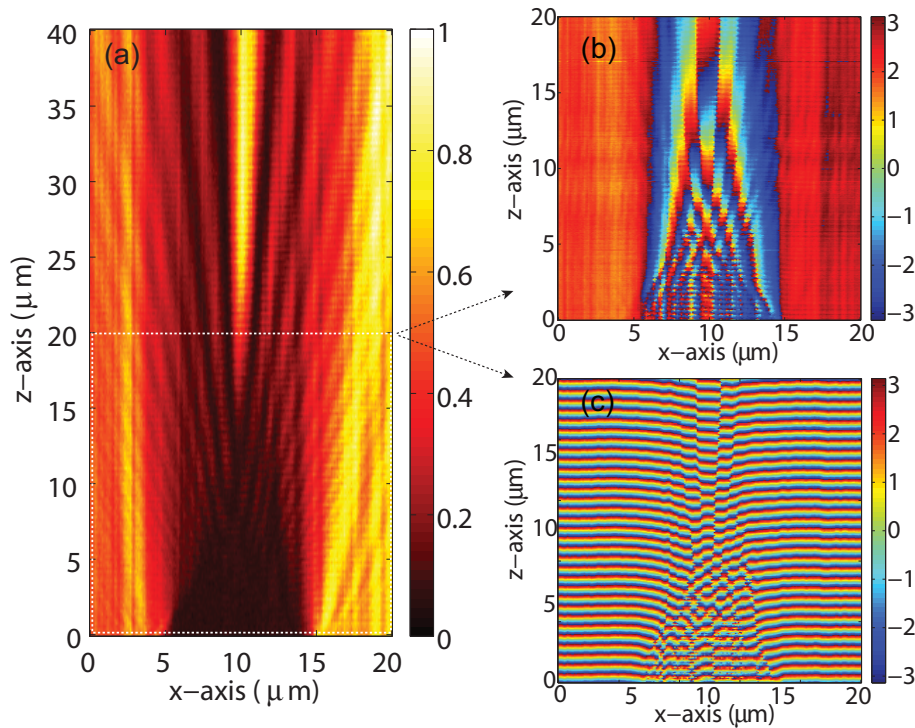

Fig. 6.5: *The longitudinal slices of the measured 3D amplitude and phase distributions of light propagating behind a the 10-µm diameter disc: (a) intensity map (20 x 40 µm²), (b) differential phase, and (c) wrapped phase maps (20 x 20 µm²). Intensity is normalized. The disc is located at z = 0 µm.*

Since the peculiar phase evolution along the optical axis is concentrated on the space close behind the obstacle, the phase fields are zoomed only in the bottom half of the intensity map. As anticipated, interference also leads to complex phase distributions. When we compare Fig. 6.3(b) to 6.5(b), we can see that the complexity proportionally increases as more numbers of side lobes emerge. In the wrapped phase distributions of Fig. 6.5(c), numerous numbers of phase singularities are observed because of the more numerous interference nodes and the more axial phase shifts than in the 4-μm case. Moreover, in Fig. 6.5(b) the axial phase shifts of the side lobes are observed, too. The longitudinal profiles through the center of the disc are taken from Figs. 6.5(a) and 6.5(b) and plotted together in Fig. 6.6. The profile of the differential phase shift has been unwrapped and plotted in wavelength units. The theoretical phase shift is calculated by Eq. (6.1); in this case the maximum phase shift is around 8λ that is equal to the radius of the obstacle $r = 5$ μm. Due to experimental limitations under low light conditions the phase measurement does not resolve fields near to the obstacle between $z = 0$ μm and 3 μm, the experimental result shows anyhow good agreement with theory.
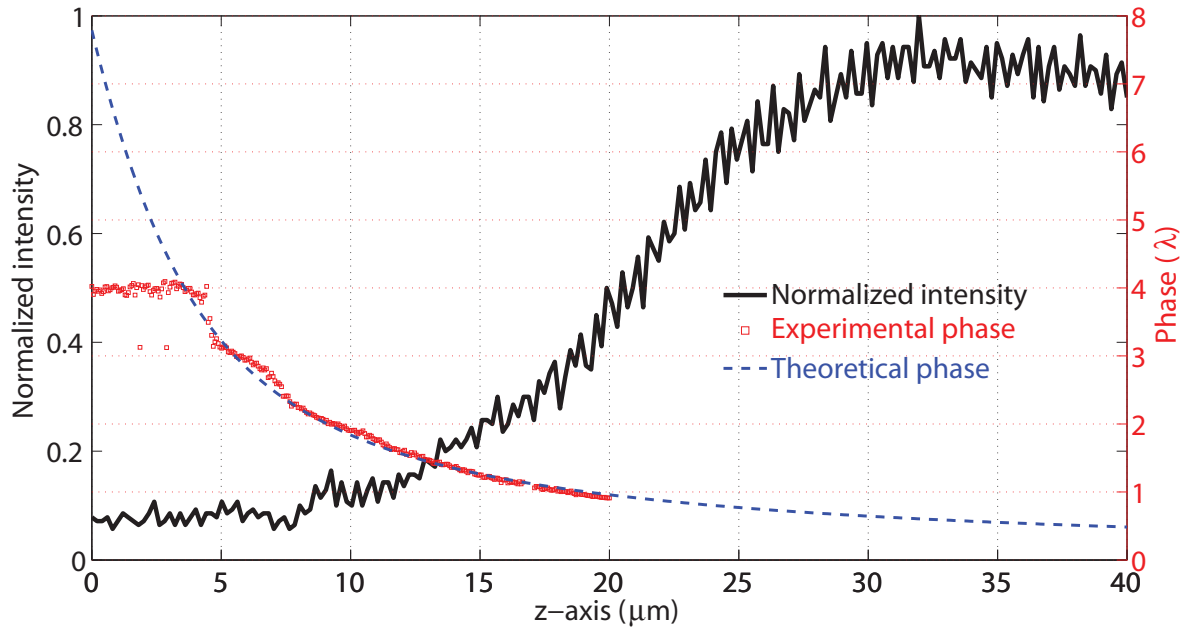

Fig. 6.6: *The axial intensity and phase profiles through the center of the disc taken from Figs. 6.5(a) and 6.5(b). The experimental phase is unwrapped and plotted in wavelength unit until z= 20 μm. The dark solid line is the normalized intensity and the blue dashed line is the theoretical phase calculated by Eq. (6.1)*

6.4 Conclusions

We investigated the diffractive light confinement by 4-μm and 10-μm metallic discs. The result of such light confinement is called the spot of Arago or the Poisson's bright spot. The HRIM measures the 3D amplitude and phase distributions of diffracted light behind such

obstacles. The intensity measurements prove the existance of the spot of Arago appearing in the shadow of the obstacle. The phase measurements reveal the peculiar evolution of the axial phase, which is found to be larger than several wavelengths. For the first time, such longitudinal-differential phase measurements are applied. A simple calculation of the geometrical optical path difference provides insight into the on-axis phase evolution of the Arago spot. By studying two different sizes of obstacles, we could show the influences of the size on the field distribution of the Arago spot. The larger obstacle leads to more interference nodes due to a longer optical path length, and such increased numbers of interference nodes create more complex field distributions behind the disc. The derived equation for the phase difference by using the concept of the OPD shows excellent agreement with experimental phase data and shows that the maximum phase difference with respect to the propagating plane wave is equal to the radius of the obatacle. Such axial phase evolutions can be interpreted as *Superluminal wavefront propagation* [6.13].

6.5 References

[6.1] E. Hecht, *Optics* (Addison Wesley, 1987), 2nd ed., Chap. 10.

[6.2] A. E. Siegman, *Lasers* (Univerty Science books, 1986), Chap. 18.

[6.3] M. Born and E. Wolf, *Principles of Optics* (Cambridge University Press, 1999), 7th ed., Chap. 8.

[6.4] J. E. Harvey, and J. L. Forgham, "The Spot of Arago - New Relevance for an Old Phenomenon," Am. J. Phys. **52**, 243-247 (1984).

[6.5] F. Talbot, "Facts relating to optical science. No. IV," Philos. Mag. **9**, 401-407 (1836).

[6.6] G. D. Gillen and S. Guha, "Modeling and propagation of near-field diffraction patterns: A more complete approach," Am. J. Phys. **72**, 1195-1201 (2004).

[6.7] R. L. Lucke, "Rayleigh–Sommerfeld diffraction and Poisson's spot," Eur. J. Phys. **27**, 193-204 (2006).

[6.8] M. Gondran and A. Gondran, "Energy flow lines and the spot of Poisson-Arago," Am. J. Phys. **78**, 598-602 (2010).

[6.9] F. S. Harris, Jr., "Light Diffraction Patterns," Appl. Opt. **3**, 909-913 (1964).

[6.10] R. E. English, Jr. and N. George, "Diffraction patterns in the shadows of disks and obstacles," Appl. Opt. **27**, 1581-1587 (1988).

[6.11] I. Chung, C. L. Andrews, and L. F. Libelo , "Near-field diffraction on the axes of disks," J. Opt. Soc. Am. **67**, 1561-1566 (1977).

[6.12] K. Uno, M. Suzuki, and K. Fujii, "Experimental Analysis of Classical Arago Point with White-Light Laser," Jpn. J. Appl. Phys. **40**, L872-L874 (2001).

[6.13] M. Vasnetsov, V. Pas'ko, A. Khoroshun, V. Slyusar, and M. Soskin, "Observation of superluminal wave-front propagation at the shadow area behind an opaque disk," Opt. Lett. **32**, 1830-1832 (2007).

[6.14] C. Huygens, *Treatise on Light* (Dover, 1962 (1690)).

CHAPTER 7

Diffractive confinement of light by a periodic object

Periodic structures diffract incident light and such diffracted light periodically interferes with each other. Finally, this leads to a periodic light confinement according to the peroid of the diffracting object. The simplest example of a periodic structure is an amplitude diffraction grating. For such gratings the so-called Talbot effect is observed [7.1]. Contrary to the spot of Arago (chapter 6), the Talbot effect has been intensively studied both in theoretical and experimental means because there are numerous applications in imaging, sensing and lithography [7.2-7.5]. In general, the period of the examined grating was relatively large because high-resolution measurement systems are required for fine gratings whose periods are comparable to the operation wavelength. Scanning near-field optical microscopy (SNOM), which provides a well-known sub-diffraction-limited resolution, was applied to measure the amplitude and phase distributions emerging from a 1-μm-period grating [7.6]. Although SNOM assures an increased resolution, scanning in the axial direction is somewhat difficult and filtering of diffraction orders is not possible.

We apply the HRIM to investigate the diffraction of light in the near-field diffraction (Fresnel diffraction) regime close to the grating. High-resolution amplitude and phase fields are measured for different wavelengths. The contributions of diffraction orders to the Talbot effect in the Fresnel diffraction regime are probed by filtering the diffraction orders in the back focal plane (Fourier plane) of the observing objective. We discuss the influence of wavelengths and the number of diffraction orders. For fine gratings, the diffraction angle, calculated by Eq. (4.1), becomes large and the higher diffraction orders exceed the paraxial and Fresnel approximations [7.7, 7.8]. We present experimental data for such cases with one-dimensional amplitude gratings. Since the slits of gratings are aligned along the y-axis, the x-z slices of the 3D data provide insights of the Talbot effect.

7.1 Talbot effect, images and length

In 1836, Talbot observed the self-imaging effect of a periodic structure, which was then called *Talbot effect* named in honor of his discovery [7.1]. Later, Lord Rayleigh showed that its origin is the interference of the diffracted beams and found that the regular repeat distance of such self-images, the so-called *Talbot length Z_T*, can be expressed as [7.9]

$$Z_T = \frac{\lambda}{1 - \sqrt{1 - \left(\frac{\lambda}{\Lambda}\right)^2}}, \qquad (7.1)$$

where Λ is the grating period and λ is the wavelength of the incident light. He also suggested the simplification of Eq. (7.1) when λ^2 is considered to be small in comparison to Λ^2. The Talbot length can be approximated by

$$Z_T = \frac{2\Lambda^2}{\lambda}. \qquad (7.2)$$

Sub-Talbot images are also found in fractions of the Talbot length along the optical axis [7.10, 7.11]. The Talbot length for different grating periods is plotted in Fig. 7.1 and a comparison between Eqs. (7.1) and (7.2) is given for a wavelength of 642 nm.
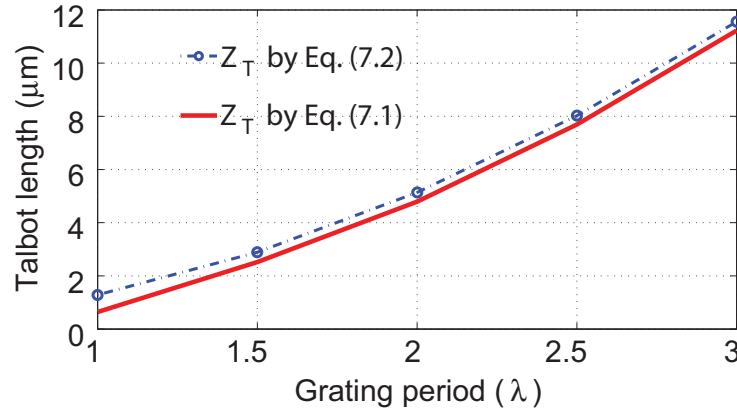

Fig. 7.1: *Ttalbot length comparison between Eqs. (7.1) and (7.2) for the wavelength (λ) = 642 nm and the period (Λ) = 1λ - 3λ.*

Supprisingly, the simplified equation for the Talbot length are sufficiently accurate for fine gratings whose period becomes comparable to the wavelength. For instance, the difference of the Talbot lengths for a grating of 1.5λ period, which are calculated by Eqs. (1) and (2) at a wavelength of 642 nm, is smaller than 300 nm. This is often negligible in experiments because the axial resolution of the far-field measurement system is in general much larger than such value. Therefore, Eq. (7.2) is suitable for comparison with experimental results.

7.2 Spectral dependency of Talbot images

Three different wavelengths are applied to investigate the spectral dependency of the diffraction angle and the Talbot length. We considered as illumination a plane wave propagating along the positive z-direction and being polarized in the x-direction, which is the TM case of the grating. The optional Bertrand lens (chapter 4, section 4.3 [see Fig.4.4]) allows to visualize the back focal plane and shows the contributing diffraction orders. The insets of Fig. 4.4 show diffraction orders of a 2-µm grating for illumination of three different wavelengths observed with a 100X / 0.9 dry objective. The periodic patterns in the axial direction, *i.e,* the Talbot images, are measured as presented in Fig. 7.2, where the *x-z* slices of the measured 3D intensity maps are shown. Refering Fig. 4.4, for a 2-µm-period grating at normal incidence one finds the angle of the first diffraction order as 19° for 642 nm, 15° for 532 nm, and 12° for 405 nm. The observing objective has a numerical aperture of NA = 0.9 corresponding to a maximum acceptance angle of 64°. In the experiments, the diffraction orders from 0th to $\pm 2^{nd}$ are collected by such an objective at 642 nm. For 532 nm and 405 nm illuminations, higher diffraction orders up to $\pm 3^{rd}$ and $\pm 4^{th}$ are collected, respectively. The effect of the slit width leads to an intensity fall off for large angles.
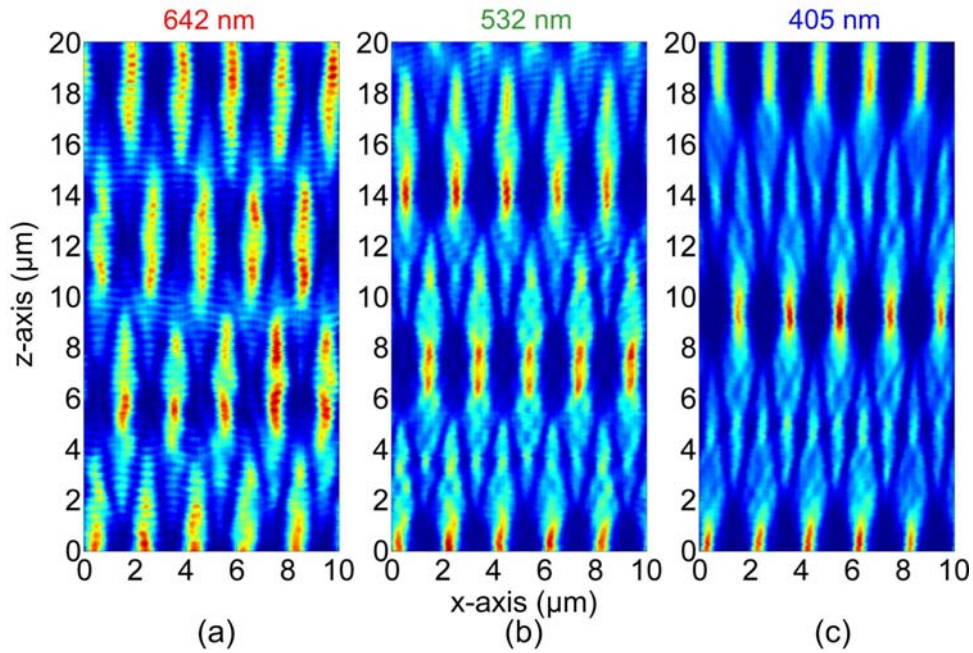

Fig. 7.2: *The x-z slices of measured 3D intensity distributions (10 x 20 µm²) emerging from a 2-µm grating: (a) 642 nm, (b) 532 nm, and (c) 405 nm. Determining the Talbot lengths in these images when only intensity fields are analyzed is subjected to experimental uncertainty because of the diffraction-limited observation. Grating surface is set to z = 0 µm.*

Better contrast and higher resolution are obtained for the intensity measurement at a shorter wavelength, in our case 405 nm, thanks to the contribution of higher orders. This corresponds to the conventional concept that a shorter wavelength leads to a better

resolution. By analyzing Fig. 7.2, the Talbot lengths are found $Z_T = 12$ μm for 642 nm, $Z_T = 14$ μm for 532 nm, and $Z_T = 20$ μm for 405 nm. The calculated Talbot lengths from Eq. (7.2) are 12.5 μm for 642 nm, 15 μm for 532 nm, and 19.8 μm for 405 nm. Experimental values show good agreement with the analytical values from Eq. (7.2). One observes self-images at Z_T and half-period shifted self-images at the half of the Talbot length ($Z_T/2$) as expected from theory [7.10]. The visibility of the smaller fractions and sub-Talbot images differs because the number of collected diffraction orders varies for different wavelengths. As expected from the Eqs. (4.1), (7.1) and (7.2), the operation wavelength alters the diffraction angle and the Talbot length.

7.3 Talbot images in immersion

As we can see in Eq. (5.2) [$\lambda_{medium} = \lambda/n$], the wavelength of light in a optically dense medium becomes shorter inversely propotional to the refractive index of the medium. When the grating is immersed in a medium, the effective diffraction angle at the operation wavelength will be smaller than in air. The HRIM is now applied to compare the grating in air with the same grating in immersion. The illumination is a plane wave of a single wavelength ($\lambda = 642$ nm). For immersion, the space between the observing objective and the grating is filled with immersion oil. We use a 100X / NA 0.7-1.4 oil objective from Leica Microsystems to collect light with different numerical apertures which can be adjusted between NA = 0.7 and 1.4 continuously. Figure 7.3 gives comparative schematics and results.
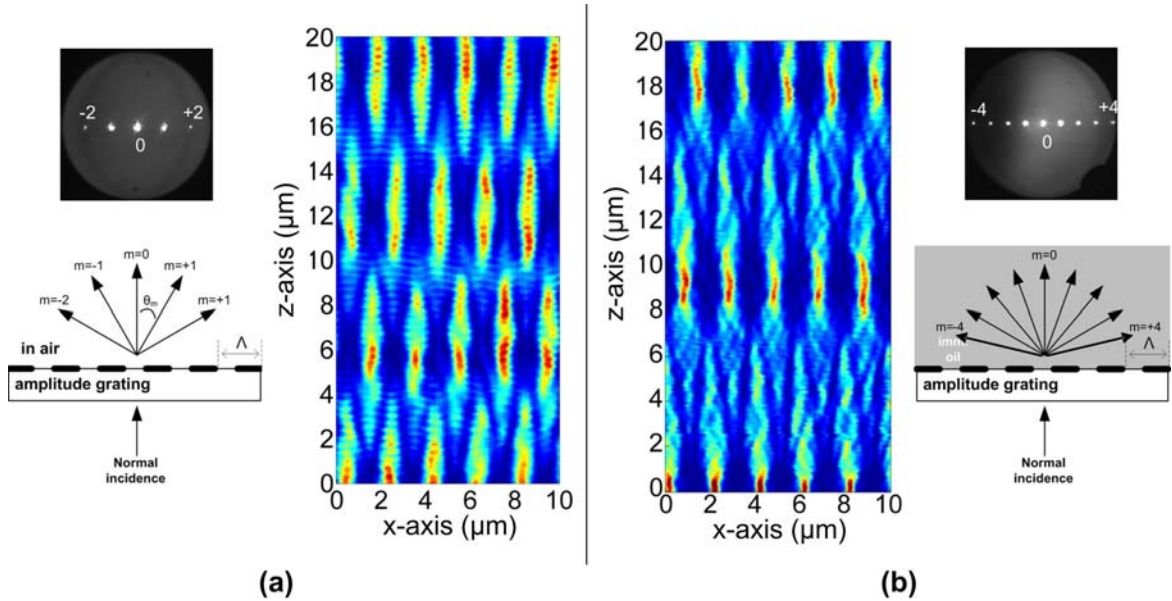

Fig. 7.3: *Experimental arrangements for a 2-μm period grating (a) in air and (b) in immersion. The insets show the back focal plane of the objective, where we can see different diffraction angles due to immersion, which leads to an increased number of diffraction orders and a higher resolution in the longitudinal intensity image.*

In Fig. 7.3(b), more diffraction orders pass through the HRIM than in the case shown in Fig. 7.3(a) and contribute to form sub-Talbot images. This is exactly the same principle that a shorter wavelength leads to a better resolution because more diffraction orders contribute to the image formation. For example, the immersion effect allows identifying the sub-Talbot image planes, which proves the achievement of better resolution. These planes show structured light fields with the double of the periodicity of the original grating amplitude, here 2 μm. In Fig. 7.3(b), sub-Talbot planes are found at about $z = 5$ μm and $z = 15$ μm distance from the grating surface ($z = 0$ μm).

7.4 Talbot images *vs* NA of the objective

We can adjust the numerical aperture with our immersion objective without changing other experimental conditions *in situ*. In order to study the relationship between the NA of the observing objective and the resolution in Talbot images, we vary the NA of the objective by adjusting a diaphragm, which is an integral part of the objective. It is instructive to see how the resolutions in intensity and phase fields increase when switching from NA = 0.7 to NA = 1.4. Figure 7.4 provides an example for such arrangements with the 2-μm amplitude grating in oil, which is the same arrangement shown in Fig. 7.3(b) except the NA variation.
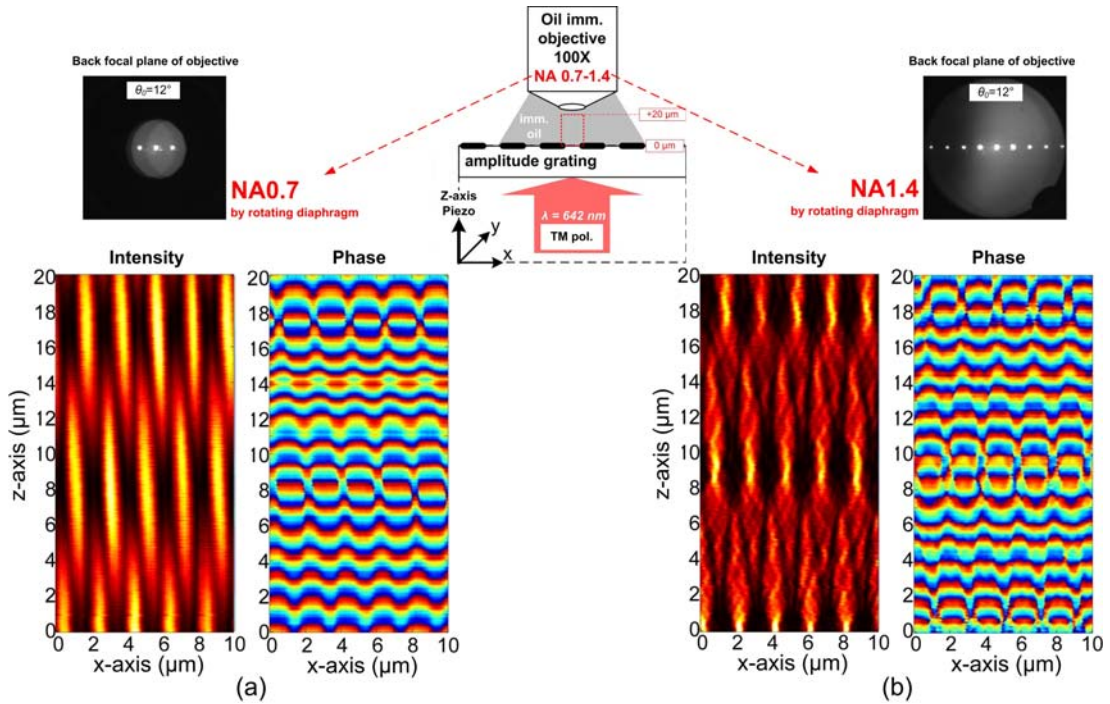

Fig. 7.4: *Influence of the NA on the amplitude and phase measurements of Talbot images from a 2-μm grating. All measurements are performed in immersion: (a) NA = 0.7 and (b) NA = 1.4. The CCD images of the back focal plane for each case are shown in the insets. The experimental geometry close to the grating is illustrated in the top center.*

In immersion (n = 1.51 at λ = 642 nm) the effective wavelength inside the medium becomes λ_{medium} = 425 nm (= λ/n). To evaluate the Talbot distance under such consideration we apply this effective wavelength in Eq. (7.2) and find the Talbot distance Z_T= 18.8 µm. Having a close look on Fig. 7.4(a), we see that the intensity images suffer from a reduced resolution and a smoothing, which is a consequence of the decreased resolution. Although the phase fields are also smoothed, they still keep the crucial information like the position of phase singularities, which occur only in the self-images that appear in multiple of the half Talbot length. When we evaluated the Talbot lengths by phase fields in both cases of NA 0.7 and 1.4, we could not find a substantial difference larger than the measurement precision, which is assumed to be the double of the z-axis pixel size (= $\lambda/20$) of the 3D measurement. Therefore, the axial distance of the planes containing such phase singularities can serve as the precise measure of the Talbot length even in the lower resolution measurement situations.

7.5 Artifical Talbot images by Fourier plane filtering

When two-plane-waves interfere, linear fringes like *Moiré patterns* along the optical axis are found as illustrated in Fig. 7.5 [7.12, 7.13]. To create periodic patterns in the propagation direction, a minimum of three orders (waves) are required and then Talbot images are formed [7.6].
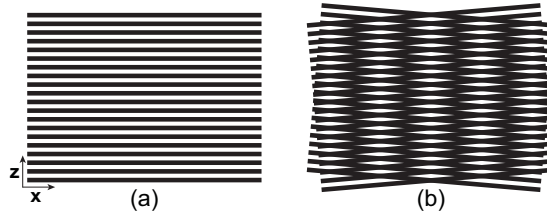

Fig. 7.5: *(a) A single grating represents a snapshot of a plane wave propagating in the positive z direction. (b) Moire patterns are formed as tilt fringes of the two-plane-wave interference.*

The roles of diffraction orders in the Talbot image formation can be studied by filtering the orders systematically. Moreover, the non-paraxial orders, whose diffraction angles are greater than 30° with respect to the optical axis at normal incidence, can be individually characterized by filtering the lower orders (< 30°). In this experiment, a plane wave of 642 nm illuminates normally a 1-µm-period amplitude grating. The space behind the grating is immersed in oil in order to provide the highest effective numerical aperture and the best resolution. For the 1-µm period grating in immersion, the diffraction angle of the first order for 642 nm wavelength is calculated to be 25° due to the effective wavelength λ_{medium} = 425 nm. In this case, the propagating diffraction orders are five from the 0th up to $\pm 2^{nd}$ orders according to the *Ewald-sphere* criterion [7.14, 7.15]. Since the maximum half angle of the acceptance cone for the NA1.4 immersion objective is 64°, these all five propagating orders are collected by the HRIM as shown in Fig. 7.6(a). With five contributing orders, the measured intensity and phase distributions are shown in the Figs. 7.6(b) and 7.6(c). Figure

7.6(c) shows the phase, as directly recorded by propagation-mode interferometry in the HRIM [see chapter 4, section 4.4]. Sub-Talbot images are detectable in Fig. 7.6(b) as a result of the contribution of the $\pm 2^{nd}$ orders. In the phase distribution in Fig. 7.6(c), phase singularities are found in the self-image planes that is a precise indication of the location of the Talbot plane (self-image plane).
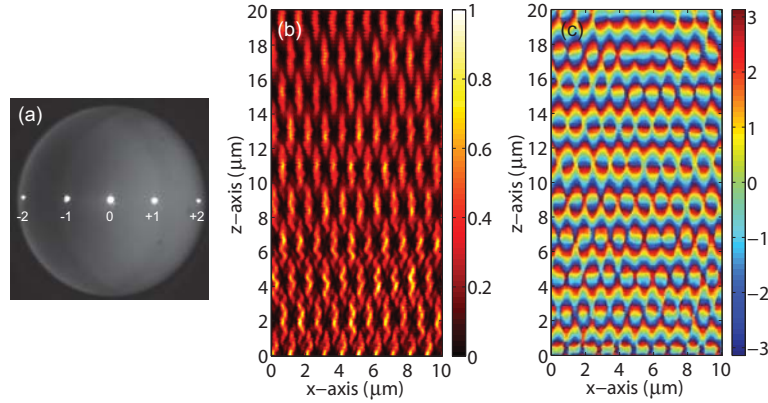

Fig. 7.6: *Measured amplitude and phase field distributions emerging form a 1-µm grating at 642 nm wavelength in oil immersion, when five propagating orders are collected. (a) The CCD image of the back focal plane of the objective to illustrate the participating diffraction orders. Longitudinal (b) intensity and (b) phase distributions. Intensity is normalized and the grating surface is at z = 0 µm.*

With these results as reference, different filtering situations will be simulated in the following sections. For easier interpretations, we monitor the contributing diffraction orders in the artificial Talbot images for each experimental arrangement. Please note that the images presented in the following sections are not real Talbot images from the grating sample; they are artificially manipulated and the results are the interference between selected diffraction orders. In order to individually block diffraction orders, we insert opaque blockers of arbitary shapes in the back focal plane of the objective. The higher diffraction orders can also be symmetrically filtered out by the objective diaphragm.

7.5.1 A single diffraction order: the 0th order

By closing the objective diaphragm, we cut off all higher orders (the $\pm 1^{st}$ and $\pm 2^{nd}$ orders) except the 0th order as shown in Fig. 7.7(a). With no surprise, just one order does not create any image since it is just a propagating wave without disturbance by the grating. This is in line with Abbe's diffraction trials [7.16, 7.17], if only one order of the diffraction spectrum of a periodic object is allowed to pass through the system, no object structure can be recognized. Although we demonstrated it with the 0th order, regardless of the order number a single diffraction order cannot render an image of the illuminated object. The only differences among the images obtained by different orders are the propagation angle of the beam with respect to the optical axis and the relative intensity due to the effect of the slit width.
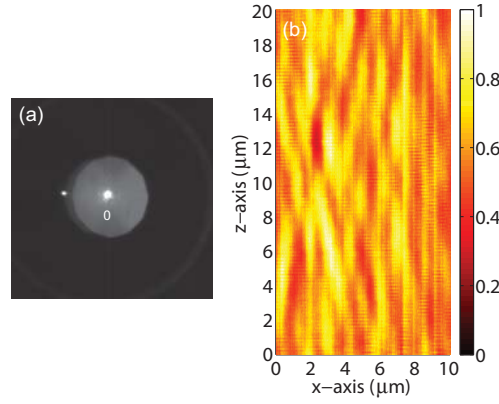
Fig. 7.7: *When only the 0th order passes through the HRIM, the measured intensity field emerging form a 1-µm grating at 642 nm wavelength in oil immersion is unspecific. (a) The CCD image of the back focal plane of the objective and (b) the longitudinal intensity distribution. Intensity is normalized and the grating surface is at z = 0 µm. The diaphragm cuts off the higher orders except the 0th order.*

7.5.2 Two adjacent orders: the 0th and $+1^{st}$ or the $+1^{st}$ and $+2^{nd}$

By letting two adjacent orders pass through the observation system, we obtain resolvable images of the sample (the 1-µm-period grating). Figures 7.8 and 7.9 present the results if two adjacent diffraction orders, for example, the 0th and $+1^{st}$ or the $+1^{st}$ and $+2^{nd}$ orders pass through the HRIM. The CCD images show which diffraction orders are passing. Typical tilt fringes of a two-plane-wave interference are created as shown in Figs. 7.8(b) and 7.9(b). For illustration, corresponding schematic snapshots of the two-plane-wave interference are drawn in Figs. 7.8(c) and 7.9(c).
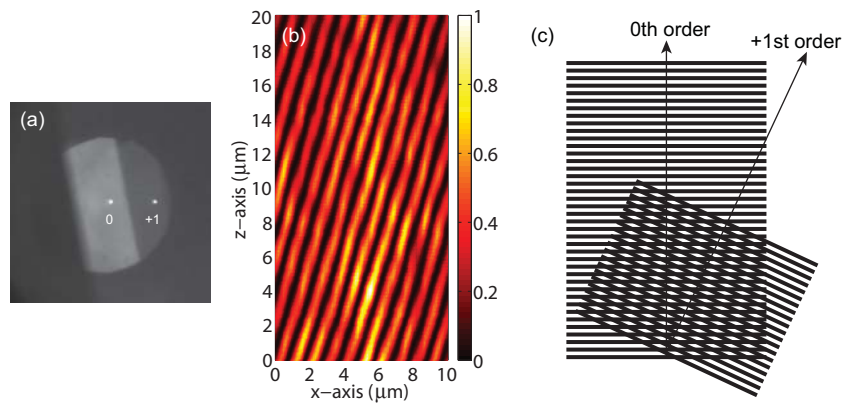

Fig. 7.8: *The 0th and $+1^{st}$ orders pass through the HRIM. (a) The CCD image of the back focal plane, (b) the longitudinal intensity distribution where the grating surface is at z = 0 µm, and (c) a schematic snapshot of the two-plane-wave interference. Arrows indicate the propagation direction of each diffraction order. Intensity is normalized. Dark obstruction blocks the -1st order and the diaphragm cuts off the $\pm 2^{nd}$ orders.*

Since they are two adjacent orders, the period of transverse images correspond the period of the grating sample. This agrees well with the Abbe's theory of image formation in a microscope [7.17], which states that a faithfully represented structure of an object can only be recognized when at least two adjacent orders of the diffraction spectrum are allowed to pass through the imaging system. The principle direction of the Moiré patterns lies on the middle of two orders as seen in the schematics of Figs. 7.8(c) and 7.9(c). Such tilted Moiré patterns lead to a continuous lateral shift of the transverse grating images during the 3D measurement, when the observation plane is scanned along the optical axis.
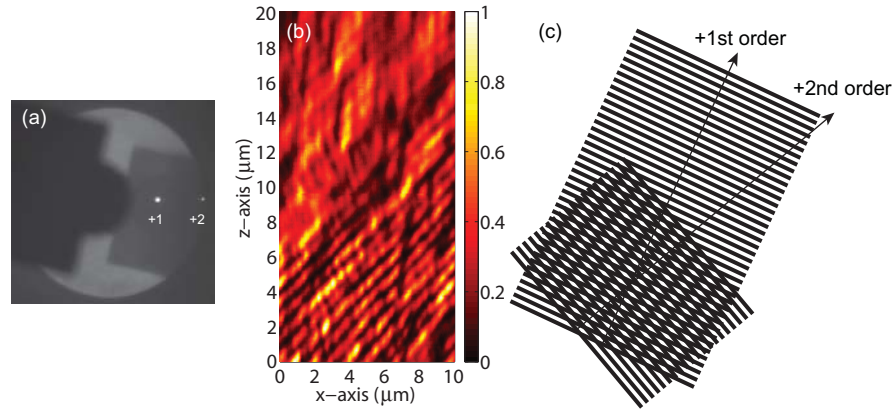

Fig. 7.9: *The +1st and +2nd orders pass through the HRIM. (a) The CCD image of the back focal plane, (b) the longitudinal intensity distribution where the grating surface is at z = 0 μm, and (c) a schematic snapshot of the two-plane-wave interference. Arrows indicate the propagation direction of each diffraction order. Intensity is normalized. Dark obstruction blocks the 0th, -1st, and 2nd orders.*

7.5.3 Non-adjacent two orders

When the intensity difference between two diffraction orders is relatively large, the image contrast is too low to provide useful information. Thus, we simulate the situation of non-adjacent two diffraction orders with symmetric ones only, which have equivalent intensity. For example, the ±1st orders are shown in Fig. 7.10 and the ±2nd orders in Fig. 7.11. Since they are not adjacent, the angle between two orders is proportional to the absolute difference of the order number (m_d) as $m_d = |+1 - (-1)| = 2$ for the ±1st orders and $m_d = |+2 - (-2)| = 4$ for the ±2nd orders. The diffraction angle for the 1st order has been calcualted to be 25° (Eq. (4.1)). Therefore, the angles between two orders are 50° for the ±1st orders and 100° for the ±2nd orders.

In contrary to the previous section, Figure 7.10(b) shows the Moiré patterns appear parallel to the optical axis due to the symmetry of the diffraction orders. The period of the transverse image is the half of the original grating as if a twice smaller grating is imaged by two adjacent diffraction orders. The phase of Moiré patterns shows a π difference between adjacent bright stripes as shown in Fig. 7.10(c).
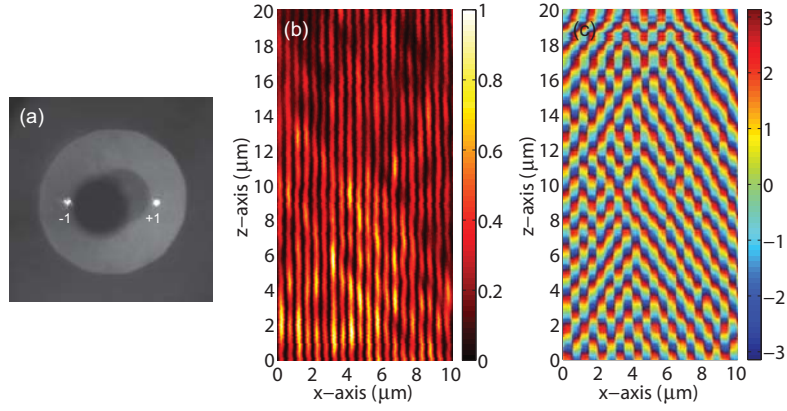
64

Chapter 7. Diffractive confinement of light by periodic objects

Fig. 7.10: *The ±1st orders pass through the HRIM. (a) The CCD image of the back focal plane, (b) the longitudinal intensity distribution where the grating surface is at z = 0 μm, and (c) the corresponding longitudinal phase distribution. Intensity is normalized. Dark obstruction blocks the 0th order and the diaphragm cuts off the $±2^{nd}$ orders.*
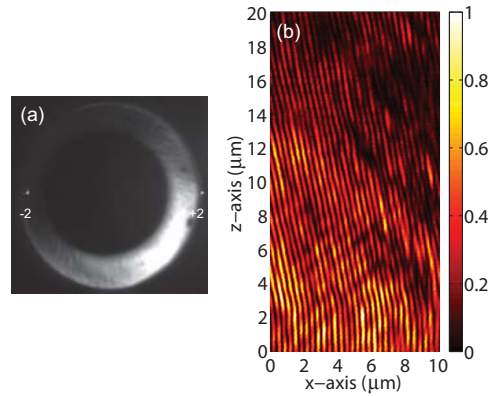

Fig. 7.11: *The $±2^{nd}$ orders are passing. (a) The CCD image of the back focal plane, (b) the longitudinal intensity distribution where the grating surface is at z = 0 μm. Intensity is normalized. Dark obstruction blocks the 0th and the $±1^{st}$ orders.*

When the $±1^{st}$ orders interfere with the 0th order which is the on-axis propagating plane-wave, they are presumed to form the self-Talbot images, which appear in the multiple of the half-Talbot length. Since the higher diffraction orders contain information of smaller features, they are much more sensitive to dimension variation and fabrication errors of the grating. The contrast and quality of the measurement in Fig. 7.11 are therefore different from Fig. 7.10. However, the case of the $±2^{nd}$ orders clearly demonstrates the expected Moire patterns with a smaller period due to the larger angle between two contributing orders, which is 100°. In general, the transverse period of the Moiré patterns is proportional to the angle difference between two plane waves. These orders are far away from the paraxial approxiamtion because the propagation angle is 50° with respect to the optical axis. However, they still fall in the case of the two-plane wave interferece, which can be understood by Fourier optics, such as a plane-wave decomposiotion.

7.5.4 Non-adjacent four orders: the $\pm 1^{st}$ and $\pm 2^{nd}$ orders

When the $\pm 1^{st}$ and $\pm 2^{nd}$ orders pass through the HRIM while and the 0th order is excluded, intensity and phase distributions are measured as shown in Fig. 7.12. Since the orders are symmetric with respect to the optical axis, on-axis Moiré fringes appear. Since the intensity of the 2nd orders is much weaker than the first orders, the dominant contributions for the lateral period come from the first orders [compare Fig. 7.10(b) with Fig. 7.12(b)]. Contributions of the 2nd orders lead to weaker modulations with a larger angle. The phase distribution shown in the Fig. 7.12(c) is also analogous to Fig. 7.10(c). In the transverse direction, we can still observe the π phase differences between the Moiré fringes.
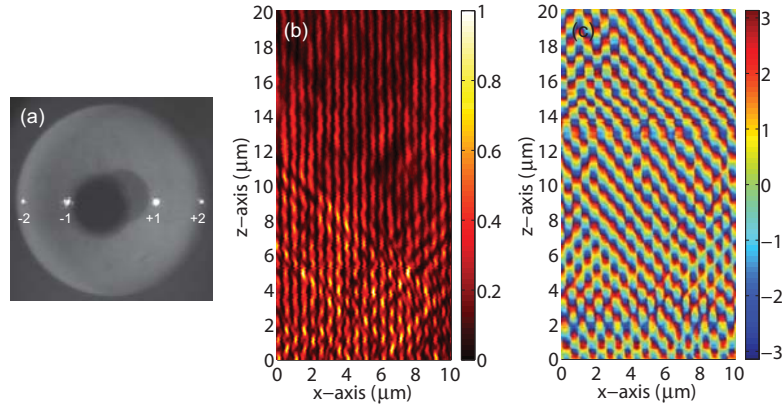

Fig. 7.12: *The $\pm 1^{st}$ and $\pm 2^{nd}$ orders pass through the HRIM. (a) The CCD image of the back focal plane, (b) the longitudinal intensity distribution where the grating surface is at z = 0 μm, and (c) the corresponding longitudinal phase distribution. Intensity is normalized. Dark obstruction blocks the 0th order.*

7.5.5 The adjacent three orders

As predicted and proven by previous experiments, the Talbot effect only occur if a minimum of three adjacent diffraction orders are involved to form an image. Figure 7.13 shows results when the 0th, $+1^{st}$, and $+2^{nd}$ orders are collected by the HRIM. As we showed in the previous section, the intensity of the 2nd orders (higher orders) is weaker than other lower orders. Therefore, their contributions to the interference are not sufficient to create pronounced axial periodic features in Fig. 7.13(b), which shows almost same intensity distributions as Fig. 7.8(b).

In general, the lower diffraction orders carry a majority of energy. We now let only three central diffraction orders, such as the 0th and $\pm 1^{st}$ orders, pass through the HRIM by closing the diaphragm of the objective that cuts off the $\pm 2^{nd}$ orders; the result is shown in Fig. 7.14. Due to the lack of the 2nd orders, less complex Talbot images are observed compared to Fig. 7.6. This has been already predicted in Fig. 7.4. The Talbot effect, which creates the axial periodic patterns, is therefore the results of the interference of three main diffraction orders.

66

Chapter 7. Diffractive confinement of light by periodic objects

The intensity balance (contrast) of contributing orders is important to reach destructive interference along the optical axis.
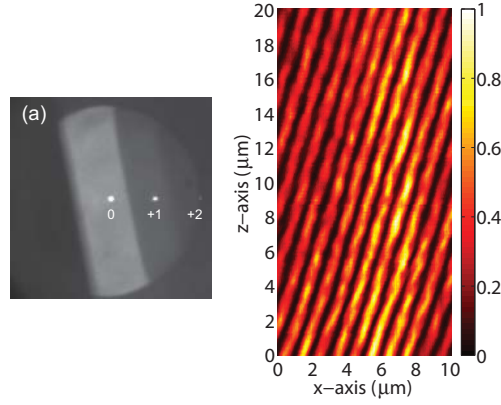

Fig. 7.13: *The 0th, $+1^{st}$ and $+2^{nd}$ orders pass through the HRIM. (a) The CCD image of the back focal plane, (b) the longitudinal intensity distribution where the grating surface is at z = 0 μm. Intensity is normalized. Dark obstruction blocks the -1st and -2nd orders.*
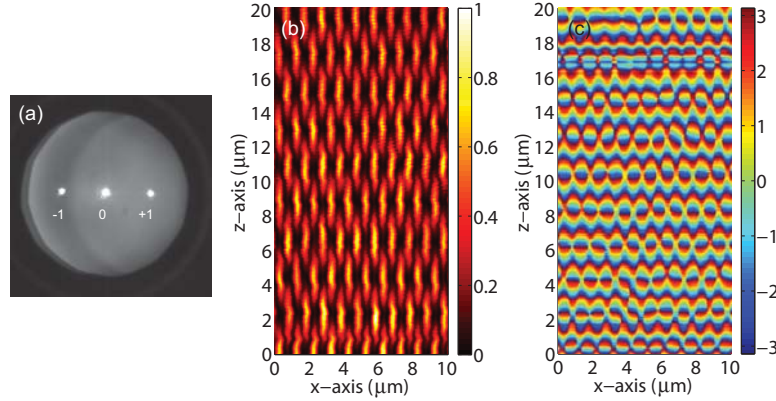
Fig. 7.14: *The 0th and $\pm1^{st}$ orders pass through the HRIM. (a) The CCD image of the back focal plane, (b) the longitudinal intensity distribution where the grating surface is at z = 0 μm, and (c) the corresponding longitudinal phase distribution . Intensity is normalized. The diaphragm cuts off the $\pm2^{nd}$ orders.*

7.6 Conclusions

Periodic objects like gratings confine light in space with repetition in the transverse and longitudinal directions. When the period of the grating approaches the operation wavelength, the diffraction angles become larger and the higher diffraction orders are non-

paraxial. We investigated such extreme situations when 2-µm and 1-µm period gratings diffract visible light and generate Talbot images. Multi-wavelengths measurments provide the wavelength dependency of the diffraction angle and the Talbot length. High-resolution amplitude and phase measurenemts reveal that the contribution of more diffraction orders leads to the sub-Talbot images. When the grating is immersed in the high-index medium, the effective wavelength becomes shorter than in air. Such immersion phenomena influences the diffraction angle and the Talbot length in exactly the same manner as the decrease of wavelength without immersion. The phase distributions show particular feature like phase singularities at the self-image planes, which are a multiple of half the Talbot length. While intensity fields are smoothened for fewer diffraction orders, singularities are observed under all conditions. The position of singularities can serve as a precise indicator of the Talbot length for measurement applications.

The HRIM allows manipulating the back focal plane of the objective by inserting obstructions to individually block diffraction orders. With this Fourier plane filtering ability, we studied the diffraction from the 1-µm period grating immersed in oil and illuminated at normal incidence by a plane wave of 642 nm. The Talbot images, which have axial periodicity, only occur when a minimum of three adjacent orders contribute to form images.

7.7 References

[7.1]   F. Talbot, "Facts relating to optical science. No. IV," Philos. Mag. **9**, 401-407 (1836).

[7.2]   O. Bryngdahl, "Image formation using self-imaging techniques," J. Opt. Soc. Am. **63**, 416-419 (1973).

[7.3]   G. S. Spagnolo and D. Ambrosini, "Talbot effect application: measurement of distance with a Fourier-transform method," Meas. Sci. Technol. **11**, 77-82 (2000).

[7.4]   A. Isoyan, F. Jiang, Y. C. Cheng, F. Cerrina, P. Wachulak, L. Urbanski, J. Rocca, C. Menoni, and M. Marconi, "Talbot lithography: Self-imaging of complex structures," J. Vac. Sci. Technol. B **27**, 2931-2937 (2009).

[7.5]   L. Stuerzebecher, T. Harzendorf, U. Vogler, U. Zeitner, and R. Voelkel, "Advanced mask aligner lithography: fabrication of periodic patterns using pinhole array mask and Talbot effect," Opt. Express **18**, 19485–19494 (2010).

[7.6]   A. Nesci, R. Dändliker, M. Salt, and H. P. Herzig, "Measuring amplitude and phase distribution of fields generated by gratings with sub-wavelength resolution," Opt. Comm. **205**, 229-238, 2002

[7.7]   E. Noponen and J. Turunen, "Electromagnetic theory of Talbot imaging," Opt. Commun. **98**, 132-140 (1993).

[7.8]   S. Teng, Y. Tan, and C. Cheng, "Quasi-Talbot effect of the high-density grating in near field," J. Opt. Soc. Am. A **25**, 2945-2951 (2008).

[7.9]   L. Rayleigh, "On copying diffraction gratings and some phenomena connected therewith", Philos. Mag. **11**, 196 (1881).

[7.10] P. Latimer and R. F. Crouse, "Talbot effect reinterpreted," Appl. Opt. **31**, 80-89 (1992).

Chapter 7. Diffractive confinement of light by periodic objects

[7.11] M. V. Berry and S. Klein, "Integer, fractional and fractal Talbot effects," J. Mod. Opt. **43**, 2139-2164 (1996).

[7.12] S. Yokozeki, "Moiré fringes," Optics and Lasers in Engineering **3**, 15-27 (1982).

[7.13] E. P. Goodwin and J. C. Wyant, *Field Guide to Interferometric Optical Testing* (SPIE, 2006).

[7.14] N. W. Ashcroft and N. D. Mermin, *Solid State Physics* (Saunders college publishing 1976), Chap. 6.

[7.15] A. Nesci, "Measuring amplitude and phase in optical fields with sub-wavelength features," Ph.D. thesis, Chap. 6, University of Neuchâtel, Switzerland, 2001.

[7.16] H. Gundlach, "From the History of Microscopy: Abbe's Diffractrion Trials," Innovation , The Magazine form Carl Zeiss **15**, 18-23 (2005).

[7.17] H. Köhler, "On Abbe's theory of image formation in the microscope," Optica Acta. **28**, 1691-1701 (1981).

CHAPTER 8

Scattering confinement of light

The scattering of light from spherical particles is well described by Mie theory, which has been established more than 100 years ago. Mie theory solves Maxwell's equations with a quasi-analytical solution rigorously [8.1, 8.2]. In consequence, many of the associated effects expected to emerge have been well studied for a long time. Nevertheless, despite this long standing history there is a constant stream of new properties that are revealed and which attract a steady research interest. Most recently, the phenomenon called *photonic nanojet* has been disclosed [8.3]. Photonic nanojets emerge if micron-sized dielectric spherical objects (cylinders or spheres) are suitably illuminated. Photonic nanojets manifest as spatially highly confined field localizations on the rear side of the sphere (or cylinder). Photonic nanojets emerge as narrow and elongated spots with a high field enhancement compared to the incident plane wave. Their existence was first discussed for cylinders in 2004 and for spheres in 2005 [8.3, 8.4]. Numerous simulation and experimental studies have been reported and two themes of research can be distinguished. On the one hand, the photonic nanojet itself was subject to investigations and its dependence on key parameters of the system, such as the refractive index of the sphere and the background medium, the size of the sphere and the wavelength, has been thoroughly investigated. On the other hand, direct applications of photonic nanojets for sensing and metrology, optical trapping, nano-patterning, and optical data storage have been discussed, which are summarized in a recent review paper [8.5]. The direct observation of photonic nanojets is a complicated issue and their observation in the visible has only been reported recently [8.6]. Here, we investigate the fundamental

properties of the field distributions of the photonic nanojet by measuring amplitude and phase fields and comparing them with simulation results.

8.1 Amplitude and phase distributions of photonic nanojet

Since the photonic nanojet is not a resonant phenomenon, for the experimental convenience we work with a monochromatic light of 642 nm. The microsphere investigated in this section is made of borosilicate glass and purchased from Duke Scientific Inc. Its refractive index is $n = 1.55$ at 642 nm and the diameter is 2 μm. Spheres are dispersedly deposited on the glass substrate and well isolated single spheres are the target of our study. A linearly polarized weakly focused Gaussian beam is used as illumination (NA < 0.01). It can be safely approximated by a plane wave in the relevant spatial domain. The photonic nanojets appear on the shadow-side surface of the microspheres and propagate to air. These transmitted fields will be measured in real space with all complexities, *i.e.,* in amplitude and phase. We use a 100X/NA0.9 objective (Leica Microsystems, HC PL FLUOTAR) for this study. The measured fields are low-pass filtered and the achievable spatial resolution for the amplitude fields is subject to the diffraction limit of the observing objective in use as discussed in the section 3.2.2.

In order to verify the experimental results and to provide a further understanding of the measured amplitude and phase distributions, we compare the experimental results to rigorous simulations. These simulations were performed in collaboration with S. Mühlig and C. Rockstuhl (Friedrich-Schiller-Universität Jena, Germany) and based on scalar propagation techniques in spatial frequency space. The well-known Mie theory for a single sphere was used to simulate the optical response of the glass sphere at first. A plane wave ($\lambda = 642$ nm) propagating along the positive *z*-direction and being polarized in the *x*–direction is considered as illumination, exactly same as in the experiment. The presence of the substrate is neglected. The order of the spherical harmonics which were considered to expand all fields in Mie theory was chosen to be 20. This large number assures sufficient convergence in the computation [8.8].

The simulation of the optical imaging of the HRIM was performed using scalar propagation techniques in spatial frequency space. At first the *x*-component of the electric field $E_x(x,y,z,\omega)$ (that corresponds to the polarization of the incident field) was calculated with Mie theory in the *x-y*-plane at $z = 10$ μm. After Fourier transforming the field to the spatial frequency space [$E_x(k_x,k_y,z=10\mu m,\omega)$], all contributions of spatial frequencies (k_x and k_y) whose absolute value is larger than the numerical aperture of the observing objective of the HRIM divided by the incident wavelength were suppressed. This mimics the behavior of the observing

objective in the experiments. Afterwards, this modified *x*-component of the electric field is propagated to the slice of interest in *z*-direction by means of free space propagation. So the field in the spatial frequency domain at every *z* position is calculated as follows:

$$E_x\left(k_x, k_y, z, \omega\right) = E_x\left(k_x, k_y, z = 10\,\mu m, \omega\right) e^{ik_z z}. \tag{8.1}$$

The inverse Fourier transformation of this field into the real space provides information on the amplitude and phase. It has to be mentioned that this way of treating the optical image of the HRIM is only an approximation. All further optical elements in the experiments except the observing objective were neglected.

8.1.1 Amplitude field distributions

We briefly pre-demonstrated the intensity distributions of photonic nanojets created by the same glass sphere for the performance evaluation of the HRIM which have been already shown in Figs. 3.6 and 3.7 for measurements and simulations, respectively. Figure 8.1 gives examples of slices in vertical (parallel to the propagation direction) and horizontal direction (perpendicular to the propagation direction) through the peak intensity of the measured 3D data, which is identical to the distribution shown in Fig. 3.6(a) before intensity normalization. The position of the microsphere is indicated by a white circle.
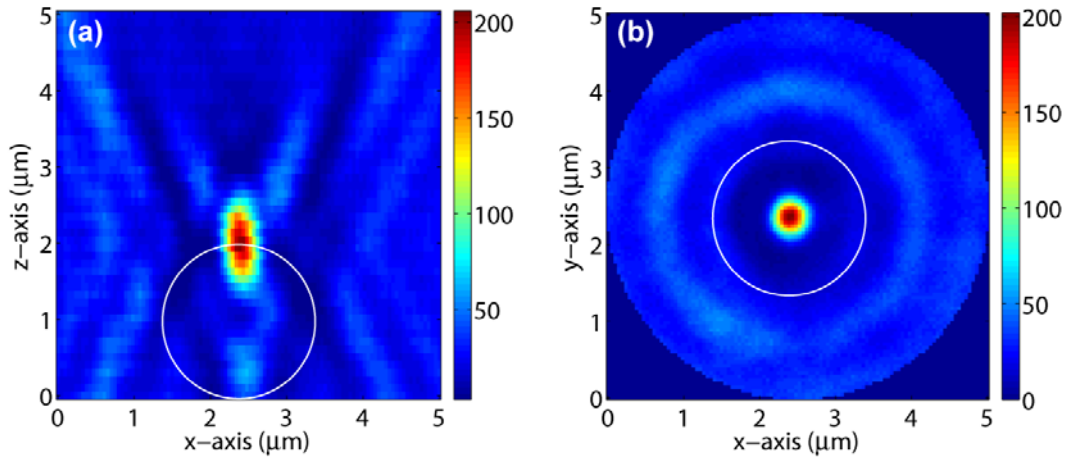

Fig. 8.1: *Measured intensity distributions of a photonic nanojet generated by a 2-μm glass sphere: (a) a vertical slice and (b) a horizontal slice through the center (intensity maximum) of the photonic nanojet. The white circle indicates the 2-μm sphere. This is identical to the distribution shown in Fig. 3.6(a).*

In Fig. 8.1(a) the principal propagating direction is along the positive *z*-axis and the incidence light was polarized in *x*-direction. It has to be mentioned that

measured fields, which appear inside or spatially before the sphere, do not correspond to the fields in real space. They correspond to the back propagated fields which are transmitted in forward direction. The HRIM itself collects light only in transmission, not the internal fields of the sphere. Nevertheless, fields above the termination of the sphere correspond to those in the real space, with the only noticeable exception that their spatial frequency components are low-pass filtered by the optical system, as usual. The horizontal slice of the intensity distribution through the plane of the largest spatial confinement is shown in Fig. 8.1(b). Useful information from such intensity measurements are the spot size and the position of the intensity maximum. Corresponding simulation results are presented in Fig. 3.7(a) with excellent agreement.

8.1.2 Phase field distributions

In addition to the intensity, the phase evolution of the fields can be equally measured in real space and results are shown in Fig. 8.2. The phase is recorded as a differential phase along the propagation direction [see section 4.4 for details].
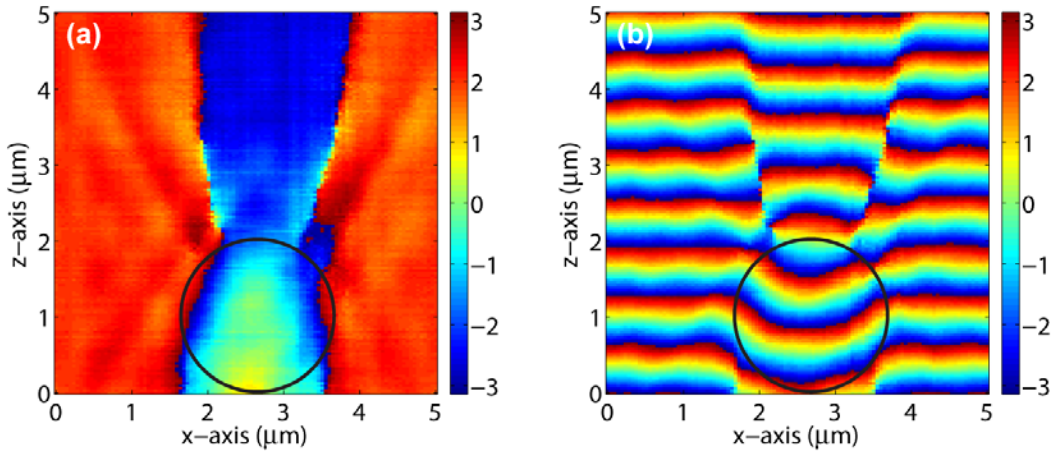

Fig. 8.2: *Measured phase distributions of a photonic nanojet spot along the axial direction. (a) The longitudinal map of the differetial phase with respect to the plane wave far away from the sphere. (b) The final wrapped phase that adds the phase advance of the plane wave to the differential phase. The black circle indicates the 2-μm sphere.*

Since the 3D measurements take several minutes, there exists an inevitable phase drift along the scanning direction due to the mechanical vibrations and light source instability. If the object however is small compared to the field of view, it can be assumed that a plane wave propagates far away from the object under investigation. Therefore, we can correct the original differential phase with respect to a plane wave far away from the sphere. The differential phase of this plane wave is considered to

be constant; completely independent from the position on the *z*-axis. An appropriate subtraction of the raw phase can easily assure this constant value. The differential phase after this correction is shown in Fig. 8.2(a). Figure 8.2(b) finally shows a phase map which is wrapped with the phase of the incident field to provide an impression of the pure phase evolution in space with an operation wavelength of 642 nm.

By abovementioned simulation methods, corresponding field distributions of such a photonic nanojet are calculated. By unwrapping the phase evolution in the propagation direction, the differential phase map is constructed, which is identical to the measured one as shown in Fig. 8.3(a). The absolute phase is shown in Fig. 8.3(b) with an impression of propagation. The good agreement between simulations and experiments seemingly justifies the approximations applied to the imaging function of the HRIM.
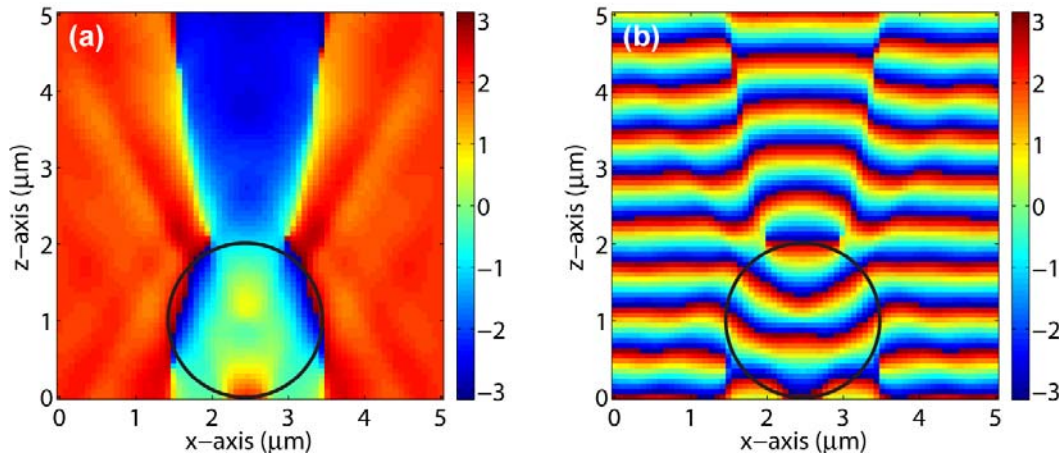

Fig. 8.3: *Corresponding simulation data to Figs. 8.2(a) and 8.2(b), which are calculated by Mie theory and scalar propagation technique: (a) differential phase map and (b) wrapped phase map. The black circle indicates the 2-μm sphere.*

The peak of maximum intensity, indicating the presence of the photonic nanojet, is found just behind the sphere at $z = 2$ μm. At the same position phase singularities appear left and right from the optical axis. Their lateral distance is measured to be 1 ± 0.1 μm and agrees well with the distance found in the simulation of 0.9 μm. We note that the field localization in real space is safely anticipated to be much stronger, since evanescent field components cannot be detected with the present set-up. Moreover, the spatial distance between these phase singularities, which correspond to roots of the intensity, are much larger separated than the full-width at half-maximum; a measure usually used to estimate the field localization in space [8.5]. In measurements and simulations, which consider the numerical aperture of the imaging objective, this FWHM was 0.38 μm. In simulations which do not consider

the imaging process but take the field directly behind the sphere, it was 0.25 μm. This corresponds to a localization of light in space in the order of 0.39 λ.

8.2 Gouy phase anomaly in photonic nanojet

While the intensity distributions in Fig. 8.1 don't reveal much information, the phase distributions in Figs. 8.2 and 8.3 directly demonstrate peculiar evolution of the fields, such as the Gouy phase anomaly [8.9]. Especially, the differential phase images in Figs. 8.2(a) and 8.3(a) show a phase variation with respect to a constant phase far away from the sphere, where the phase appears constant and corresponding to the incident plane wave. The Gouy phase anomaly is a phase shift found along the *z*-axis (at *x=y=0*μm) and for accessing such phenomenon we plot the measured phase shift in Fig. 8.4.
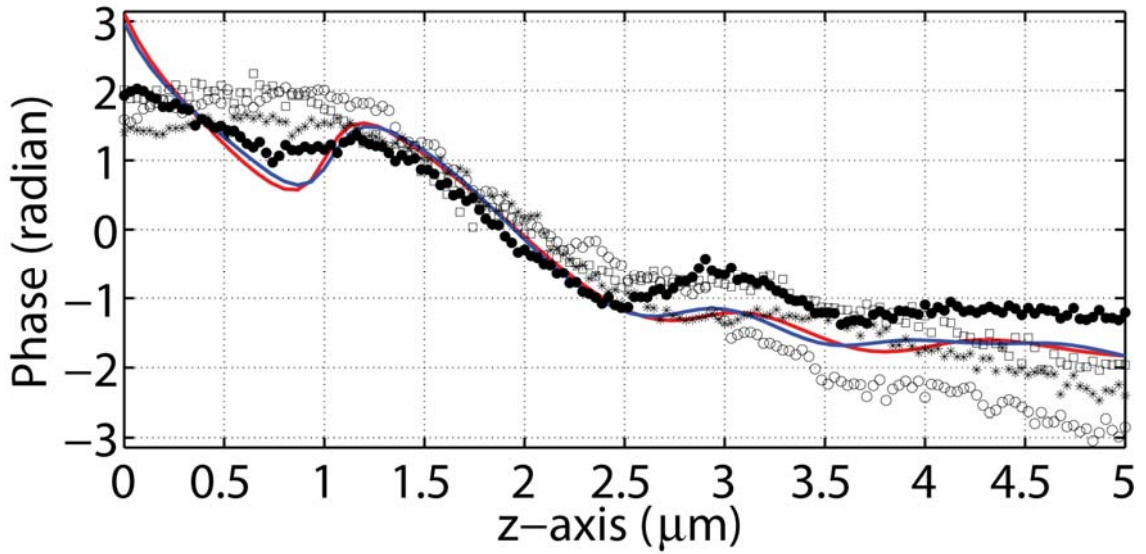

Fig. 8.4: *Profiles of differential phase in the axial direction (z-axis) along a central line of the photonic nanojets. The solid red and blue lines correspond to the rigorous simulations for NA = 0.9 and for NA = 1, respectively, and the various markers correspond to four individual measurements at a 2-μm glass sphere. The filled circles correspond to the experimental results presented in Fig. 8.2(a).*

We explicitly show the differential phase where the advance from the plane wave is excluded, being fully in line with the definition of the Gouy phase anomaly. Experimental data from four individual measurements with 2 μm glass spheres are shown. Since there is no analytical solution of the Gouy phase anomaly for the scattered hotspots, we extract, as a theoretical reference, results from the rigorous simulations for NA = 0.9 [see Fig. 8.3(a)] and NA = 1 and include the results as

solid red and blue lines in Fig. 8.4, respectively. As long as almost all effective fields are captured by a NA = 0.9 acceptance angle, the NA = 1 case does not lead to different results.

Three different regimes can be distinguished along the *z*-axis. (1) Positions close to the substrate [*z* = 0 - 1 μm]: The observation suffers from significant amount of spherical aberration and fields suffering multiple reflections between the substrate and the sphere. This naturally disturbs the measurements and causes experimental uncertainties. (2) Positions inside the sphere, at the intensity hotspot and behind the intensity hotspot [*z* = 1 - 3.5 μm]: The high contrast of interference fringes and small amount of spherical aberration in the upper half of the sphere provide reliable results. A comparison with theory shows very good agreement in this region as expected. (3) Positions far away behind the hotspot [*z* = 3.5 - 5 μm]: As seen in Fig. 8.1(a), there is almost no intensity detectable which leads to a very low contrast of interference fringes and measured phases are subjected to noise. Nevertheless, the very good agreement between simulation and experiment provides confidence that the results are sufficiently exact.

8.3 Transition from nanojet to refractive focal spot

Apart from the photonic nanojet, dielectric spheres of a relative large size fall in a special case of thick lenses in air, which is known as *ball lens* [8.10]. Ball lenses with diameters from a few millimeters to several hundred micrometers have been intensively studied for direct applications, *e.g.,* optical-fiber telecommunications, rather than actual focal properties. When the size of the sphere falls in the micrometer scale, fundamental optical characteristics of spheres start to depart from the prediction of geometric optics. In this case one should invoke the wave nature of light and rigorous theories are required to properly understand the responses [8.11]. As we have discussed in the previous section, for much smaller microspheres (diameter from ~2λ to greater than 40λ [8.12]) that are known to generate photonic nanojet spots, rigorous simulations have already been applied. However, the responses of intermediate-size spheres, *i.e.,* the transition from a photonic nanojet to a refractive focus by a ball lens, have never been discussed in detail.

In this section we investigate optical responses of dielectric spheres with different diameters (from 1 μm to 400 μm). The measured amplitude and phase distributions near the focal point with a plane-wave illumination are presented. By varying the sphere sizes while all other conditions stay the same, we study how the focal spots evolve from a scattered hotspot (a photonic nanojet) to a refractive focal spot (the response of a ball lens).

8.3.1 Optics of ball lens

The optics of ball lenses is well approximated by geometrical or ray optics for analytical solutions of the effective focal length (EFL), the back focal length (BFL), and numerical aperture NA written as [8.10]

$$EFL = \frac{nR}{2(n-1)},$$

$$(8.2)$$

$$BFL = EFL - R,$$

$$(8.3)$$

$$NA = \frac{half\ aperture\,(a)}{focal\ length} = a \cdot \frac{2(n-1)}{nR},$$

$$(8.4)$$

where n is the refractive index of the sphere, R is the radius of curvature, and a is the half aperture of the entrance pupil. The EFL is measured from the center of the ball lens and the BFL is measured from the shadow-side surface. NA varies depending on the size of the entrance pupil as conventional lenses do. We focus on the case that the full entrance pupil is illuminated ($a = R$).

8.3.2 Field disbtibutions of light confinement by various microspheres

For the measurement of the field distributions near the focus of ball lenses, a 100X / NA0.9 objective and a laser with 642 nm wavelength are applied in the HRIM. Due to such broad range of sizes (from 1 μm to 400 μm), it is difficult to commercially obtain them in one single material. Therefore, microspheres studied here were made of borosilicate glass (n = 1.56 at 642 nm) for the size of 2 μm - 22 μm, polystyrene (n = 1.59 at 642 nm) for the size of 1 μm - 100 μm, and soda lime glass (n = 1.51 at 642 nm) for the size of 100 μm - 400 μm. They are purchased from Duke Scientific Inc. Typical amplitude and phase distributions of the focal spot created by a 200-μm glass sphere are shown in Fig. 8.5. In the lower half of Figs. 8.5(a) and 8.5(b), we can observe results of the severe influence of the spherical aberration in both intensity and phase measurements. Aberrations smear out the focal spot and pronounced strong fields in side lobes are found. When the sphere size varies, the field distributions are drastically changed. Figure 8.6 shows transverse intensity and phase maps in the plane of the peak intensity of the spheres of different sizes. First of all, the smaller spheres create a smaller focal spots, which are not predictable by ray optics as the NA by Eq. (8.4) is constant for the full aperture illumination. Phase distributions for the spheres < 3 μm are particular. As their sizes are just a few times larger than the operation wavelength (λ = 642 nm), diffraction rings are not observed

in the spheres body. Finally, an area with nearly no phase variation represents the sphere.
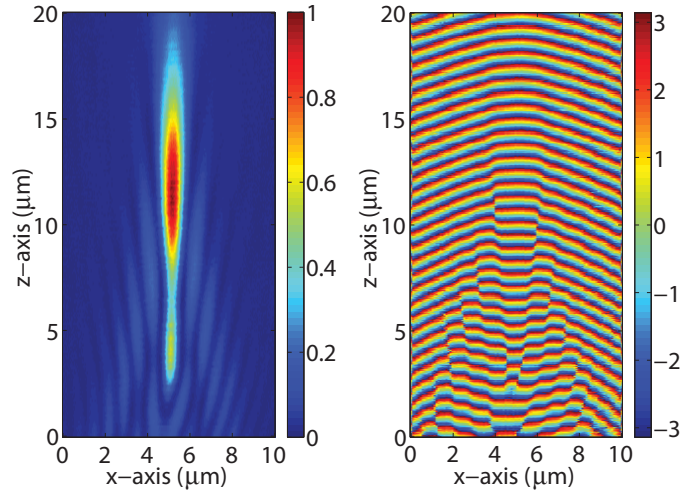

Fig. 8.5: *Measured longitudinal intensity and phase distributions of the focal spot of the 200-µm glass sphere under plane-wave illumination.*
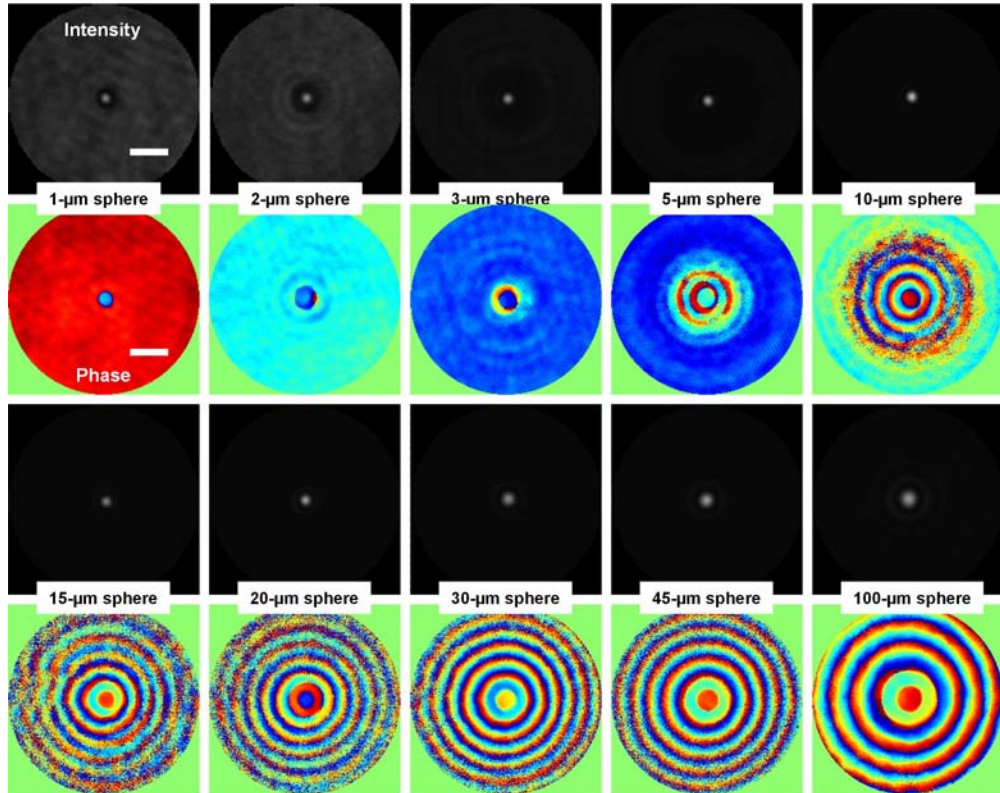

Fig. 8.6: *Measured longitudinal intensity and phase distributions of the focal spot of the 200-µm glass sphere under plane-wave illumination.*

8.3.3 Focal spot size of the ball lens

We found in Fig. 8.6 that the spot size varies depending on the size of the sphere. It is therefore interesting to plot the FWHM spot sizes in the transverse directions of different spheres. This is given in Fig. 8.7 in a semi-logarithmic scale. The different types of spheres and directions are visualized as follows: (1) six-pointed stars are for borosilicate glass spheres of 2 µm – 22 µm diameters, (2) filled circles are for polystyrene spheres of 1 µm - 100 µm diameters, and (3) filled five-pointed stars are for soda lime glass spheres of 100 µm - 400 µm diameters.
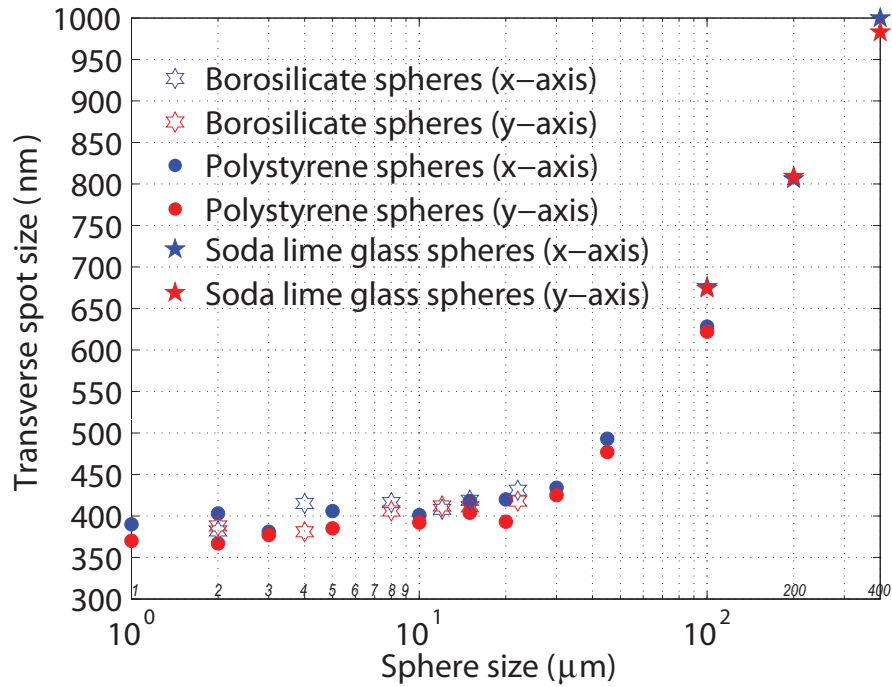

Fig. 8.7: *Measured FWHM spot sizes vs the sphere size (diameter) in the x- and y-axes. Sphere sizes are in logarithmic scale. The legend provides details of spheres and directions.*

For both glass and polymer spheres of sizes below 15 µm the FWHM spot sizes stay close to 400 nm for both x- and y-axes; in this regime the photonic nanojet phenomenon governs the light confinement process. Due to the high confinement, such spots demonstrate a vectorial charasteristic as slightly smaller extension of spot sizes in the orthogonal axis (y) of the polairzation (linearly polarized in the x-axis) could be found. From the-15 µm sphere on, the increment of the spot sizes become noticable compared to the photonic nanojet spots. Equation 8.4 leads to an NA of 0.74 with $n = 1.59$ (polystyrene) at 642 nm, which would result in a theoretical FWHM spot size of 433 nm when aberrations are neglected. The sphere of 30 µm shows the closest spot size as 430 nm, which means that we can exploit the full NA

of the sphere without severe influence of aberrations. As the size of the sphere increases above 30 μm, aberrations drastically degrade the spot sizes. Moreover, asymmetry in the longitudinal direction and strong fields in the side lobes are caused, which are shown in Fig. 8.5.

8.3.4 Focal length of the ball lens

Another key parameter to be considered is the focal length, which is experimentally recognized as the distance of the peak intensity from the reference plane, such as the rear surface of the sphere. We compare the theoretical values with experiemntal results (the distance of the peak intensity) as shown in Fig. 8.8. For the theoretical focal lengths, the BFLs are calculated by Eq. (8.3) for polysterene and soda lime glass spheres. Here the borosilicate glass spheres are excluded due to the small size, which leads to the response of the photonic nanojet. Surprisingly, experimental results show that ray optics is valid for the focal length of micrometer-size ball lenses down to the diameter of 15 μm. For the spheres smaller than 15 μm, the positions of the peak intenxity (= focal points) are found on the surface of the sphere as shown in the inset of Fig. 8.8. As discussed in the analysis of the spot size, such small spheres would already fall in the photonic nanojet regime.
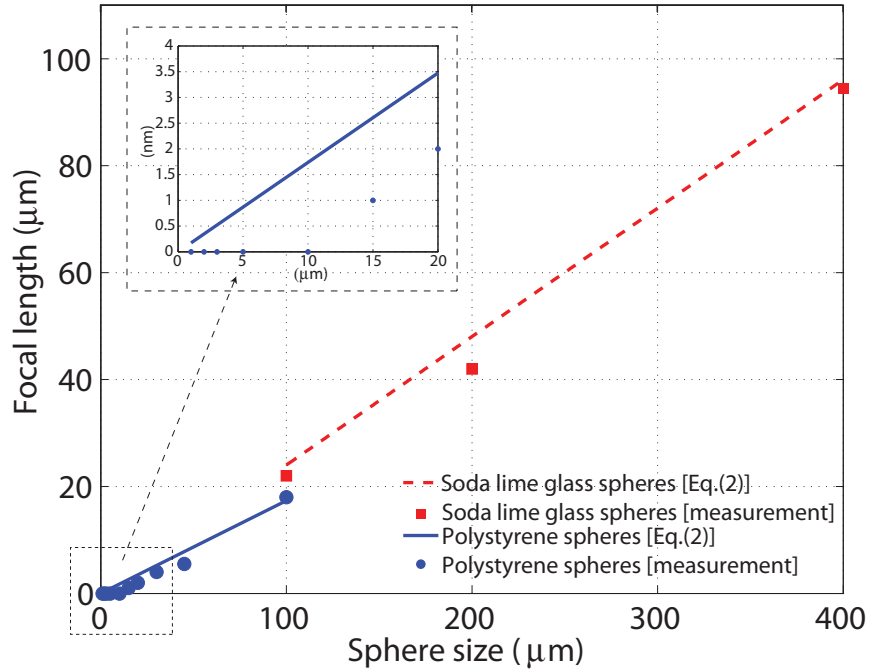

Fig.8.8: *Focal lengths (in experiment, the distance of the peak intensity from the sphere surface) vs the sphere sizes. Blue and red lines are calculated data by Eq. (8.3) for polystyrene and soda lime glass spheres and blue and red markers are measured data for corresponding spheres.*

   Longitudinal slices of the 3D intensity data in Fig. 8.9 confirm the push away of the focal spot from the surface of the sphere beginning from 15-μm sphere size. Upper row shows the intensities in a linear scale and lower row in a logarithm scale to emphasize the low intensity fields. Figure 8.9(a) demonstrates a symmetric spot in the longitudinal direction, which means the spot stays on the surface and therefore the spherical aberration does not occur. In Figs. 8.9(b) - 8.9(d), the lower row shows typical asymmetric longitudinal spots and severe influences of aberration, which are pronounced as the side lobes and ripples in the bottom half of the images. Moreover, the longitudinal spots are stretched due to such aberrations. This gives the possibility to see the transition between the photonic nanojet regime, where the high confinement of light occurs on the rear surface of the sphere and the spot size stays in the smallest value, to the refraction dominant regime. In the latter, the spots are affected by aberrations and larger spots are obtained when the sizes of the spheres are increased. Besides, the focal length follows the theoretical predictions by Eqs. (8.2) and (8.3), which are valid until the size of the sphere reaches up to 15 μm.
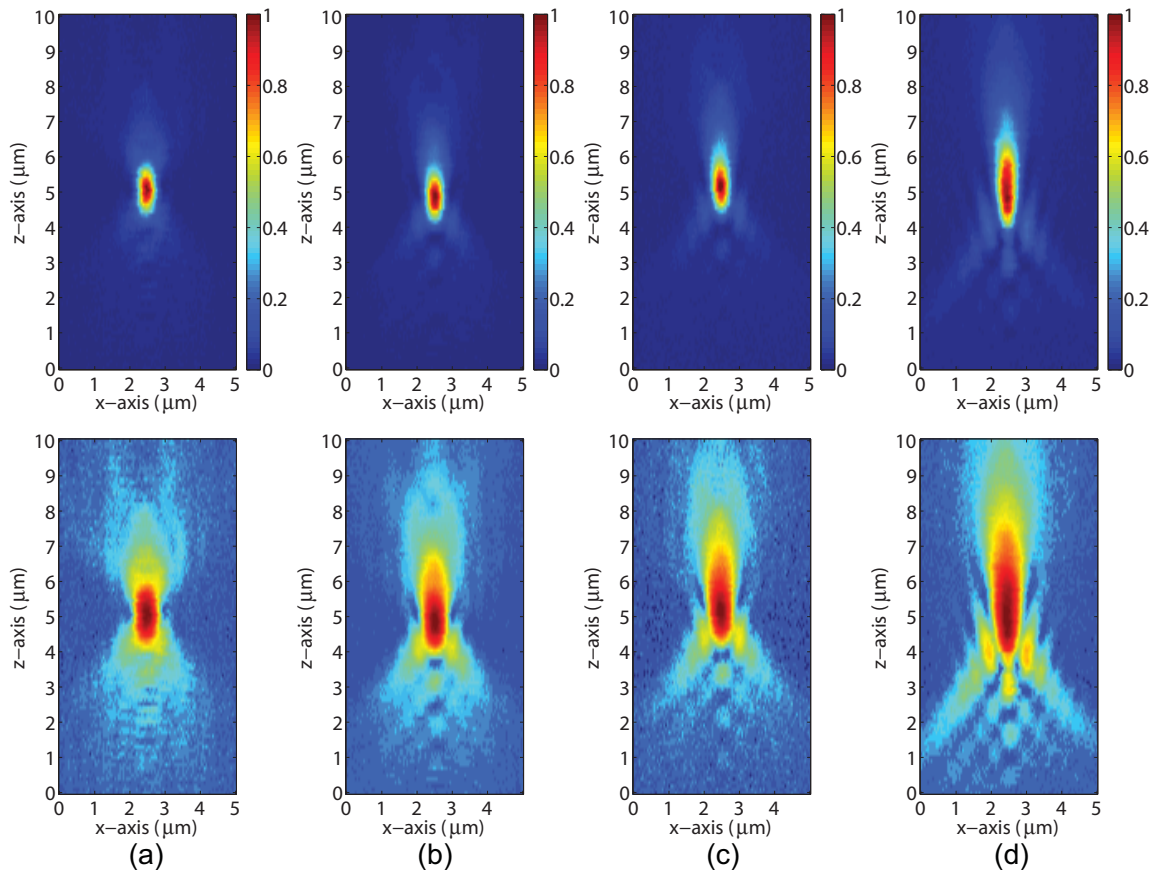

Fig.8.9: *Longitudinal slice of the focal spots created by the polystyrene microspheres of (a) 10-μm diameter, (b) 15-μm diameter, (c) 20-μm diameter, and (d) 30-μm diameter. Intnensity are all normalized and displayed in linear scale and in the lower row in logarithm scale to emphasize the low contrast fields.*

8.4 Conclusions

First, fundamental studies of amplitude and phase of the photonic nanojet are carried out with both experimental and theoretical means. Especially, the longitudinal-differential phase measurement nicely demonstrates the Gouy phase anomaly at regions of the scattering light confinement. Although an absolute discussion is difficult, it can be seen that in a very narrow spatial domain when compared to the wavelength, the phase advance of the field is strongly deviating when compared to that of the respective plane wave. In order to confine the incident light fields in tiny spatial domains corresponding to the photonic nanojets, the evolving wave fronts undergo a sudden transition from a spherical to a plane shape (converging) and from a plane to a spherical shape (diverging). This is comparable to a Gaussian beam which undergoes a focusing in its waist. The modifications to the wave fronts cause locally different propagation distances along the propagation direction. This causes a phase advance different to a plane wave for which the Gouy phase is just a measure. This transition is strongest at the transition from a spherical to plane wave front and vice versa. The wave front locally propagates different distances and these are accumulated along the principal propagation direction causing finally a strong phase shift with respect to the plane wave. Also shown already in several ways for Gaussian beam propagation we demonstrate by experimental and theoretical means that a phase anomaly exists also in scattered photonic nanojets. This supports the fact that the Gouy phase anomaly is a general phenomenon found for all kinds of light confinement in space.

Second, the influence of the size of the sphere until several hundreds of micrometers on such light confinement is studied. Amplitude and phase disrtibutions differ when the sphere sizes are varied. Finally, we disinguish two different regimes for the glass and polymer microspheres: (1) the photonic nanojet regime, where scattering phenomenon leads to the smallest spots and the confinement of light occurs on the surface of the sphere [diameter = 1 μm - 10 μm], and (2) refractive dominant regime, where the hotspts departure from the surface of the sphere and therefore the spherical aberration enlarges the spot sizes and destroies the axial symmetry [diameter = 15 μm - 400 μm]. The latter case, the ball lens optics can be applied to predict the actual properties like a focal length, in experiment, the distance of the peak intensity from the sphere surface. However, the spot sizes are not predictable with analytical solution given by ray optic. Rigorous calculations or high-resolution measurements can only provide the proper insights of the actual properties.

8.5 References

[8.1]   G. Mie, "Beiträge zur Optik trüber Medien, speziell kolloidaler Metallösungen," Ann. d. Physik, **25**, 377-445 (1907).

[8.2]   H. C. Van de Hulst, *Light Scattering by Samll Particles* (Dover, 1981), Chap. 9.

[8.3]   Z. Chen, A. Taflove, and V. Backman, "Photonic Nanojet enhancement of backscattering of light by nanoparticles: a potential novel visible-light ultramicroscopy technique," Opt. Express **12**, 1214-1220 (2004).

[8.4]   X. Li, Z. Chen, A. Taflove, and V. Backman, "Optical analysis of nanoparticles via enhanced backscattering facilitated by 3-D photonic Nanojets," Opt. Express **13**, 526-533 (2005).

[8.5]   A. Heifetz, S.-C. Kong, A. V. Sahakian, A. Taflove, and V. Backman, "Photonic Nanojets," J. Comput. Theor. Nanosci. **6**, 1979-1992 (2009).

[8.6]   P. Ferrand, J. Wenger, A. Devilez, M. Pianta, B. Stout, N. Bonod, E. Popov, and H. Rigneault, "Direct imaging of photonic Nanojets," Opt. Express **16**, 6930-6940 (2008).

[8.7]   M.-S. Kim, T. Scharf, S. Mühlig, C. Rockstuhl, and H. P. Herzig, "Gouy Phase Anomaly in Photonic Nanojets," Appl. Phys. Lett. (2011) (accepted for publication).

[8.8]   C.F. Bohren and D.R. Huffman, *Absorption and Scattering of Light by Small Particles* (Wiley, NY, 1983).

[8.9]   L. G. Gouy, "Sur une propriete nouvelle des ondes lumineuses," C. R. Acad. Sci. Paris **110**, 1251 (1890).

[8.10] F. Träger, *Handbook of Lasers and Optics* (Springer, 2007), Part A, Chap. 2.

[8.11] R. P. Ratowsky, L. Yang, R. J. Deri, J. S. Kallman, and G. Trott, "Ball lens reflections by direct solution of Maxwell's equations," Opt. Lett. **20**, 2048-2050 (1995).

[8.12] S. Lecler, Y. Takakura, and P. Meyrueis, "Properties of a three-dimensional photonic jet," Opt. Lett. **30**, 2641-2643 (2005).

CHAPTER 9

Engineering photonic nanojets

In chapter 8, we theoretically and experimentally studied the characteristics of amplitude and phase distributions of scattering hotspots, *i.e.,* the photonic nanojets. Heifetz gives a definition and the basic properties of such spots [9.1]:

The photonic nanojet is a narrow, high-intensity electromagnetic beam that propagates into the background medium from the shadowside surface of a plane-wave illuminated lossless dielectric microcylinder or microsphere of diameter greater than the illuminating wavelength, λ. Key properties of the photonic nanojet include:

- *It is a non-evanescent, propagating beam that can maintain a subwavelength full-width at half-maximum (FWHM) transverse beamwidth along a path that can extend more than ~2λ beyond the dielectric cylinder or sphere.*

- *Its minimum FWHM beamwidth can be smaller than the classical diffraction limit, in fact as small as ~λ/3 for microspheres.*

- *It is a nonresonant phenomenon that can appear for a wide range of the diameter of the dielectric microcylinder or microsphere from ~2λ to more than 40λ if the refractive index contrast relative to the background medium is less than about 2:1.*

- *It has a high intensity that can significantly exceed that of the illuminating wave.*

The majorities of all investigations rely on a linearly polarized plane wave for illumination due to its convenience in experiments and simulations. There are only a few studies which apply a focused beam to reduce the spot sizes of a photonic nanojet [9.3]. In this chapter we close this gap and investigate systematically how a modified and more complex illumination affects the properties of photonic nanojets.

We experimentally engineer photonic nanojets by manipulating the incident wavefront and/or the polarization. The HRIM allows manipulating the illumination conditions and, at the same time, measuring and monitoring the modified characteristics, such as the wavefront and the polarization of the illumination *in situ*. This is a great advantage since controlling and manipulating the illumination conditions are difficult tasks in other experimental systems, such as scanning near-field optical or a confocal microscopes, where the illumination is usually restricted to an individual experimental condition. This advantage of the HRIM comes at the expense that the field is not probed directly behind the sphere but the fields are measured instead in the far-field in an image plane. First, we apply the illumination engineering, such as spherical-wave illumination and a focused Bessel beam (Bessel-Gauss beam) illumination [refer section 3.1.3]. Second, the polarization-induced beam shaping is applied to create particular illumination spots [refer section 4.5]. A further simulation of the more complicated illumination scenarios, which are considered in this chapter, was not possible since the illumination cannot be characterized with sufficient precision of all parameters as required for a proper simulation. Hence, only experimental results are shown and discussed.

9.1 Photonic nanojet by spherical-wave illumnations

We apply converging and diverging spherical wavefronts generated by a purposely defocusing to tailor the position of maximal intensity, a quantity which is often linked to the focal length of photonic nanojets. For convenience we recall briefly the situation of focusing for a conventional refractive lens. For a lens we find its focal point moving backward and forward from the principal focal plane found for plane wave illumination depending on the curvature of the incident wavefront. That is possible because the curvature induced by the lens simply adds to the curvature of the illumination. We apply this simple mechanism here to adjust the focal length of the photonic nanojet.

To generate spherical-wavefront illuminations with different radius of curvatures, we use a 50X / NA0.9 objective (Leica Microsystems, HXC PL APO). In HRIM, we can precisely measure and control the radius of curvature (ROC) of waves by interferometrically recording phase distributions at each defocusing situation. The 2D phase distributions at the entrance plane are shown in Figs. 9.1(a) - 9.1(d), where

target ROCs were 50 µm, 15 µm, -15 µm, and -50 µm, respectively. The ROC of a converging spherical wavefront is defined to have a negative value. Figure 9.1(e) shows wavefront profiles and measured ROCs derived from Figs. 8.1(a) – 8.1(d), which are obtained by a 2D phase unwrapping process [9.4, 9.5]. ROCs are found to be 52.7 µm, 14.9 µm, -17 µm, and -48.3 µm, respectively. Diverging spherical wavefronts in Figs. 9.1(a) and 9.2(b) show undesired spherical aberrations and ripples in the wavefront profiles. These aberrations are a result of the coverglass correction of the microscope objective which only correctly applies for the lower half space of the illumination conditions in the experimental geometry. These manipulated wavefronts were used to engineer nanojets.
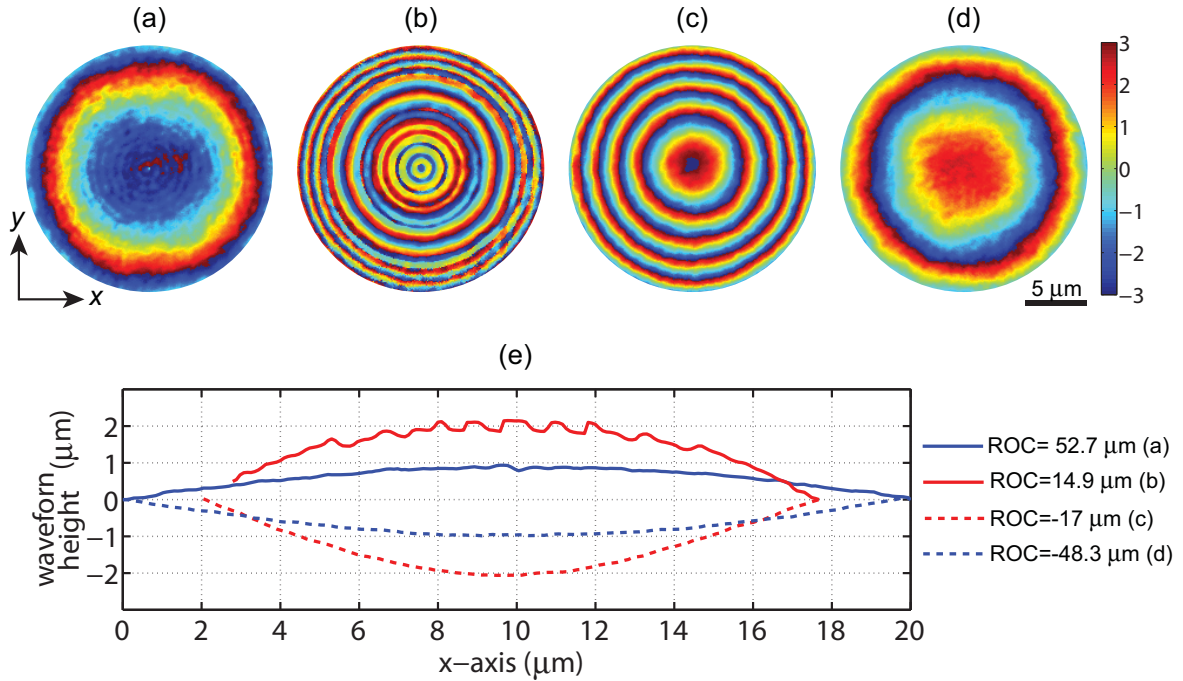

Fig. 9.1: *Measured 2D phase distributions of spherical wavefornts at the entrance plane of the sphere, which are used to engineer photonic nanojets: (a) ROC = 52.7 µm, (b) ROC = 14.9 µm, (c) ROC = -17 µm, and (d) ROC = -48.3 µm. The colorbar scale is radian. (e) Profiles through the center of the wavefront from (a) to (d).*

Figure 9.2 shows the longitudinal intensity distributions of photonic nanojets generated by a glass sphere with a diameter of 12 µm. Engineered nanojets are compared to the nanojet formed by a plane-wave illumination as shown in Fig. 9.2(a). As one would expect from a classical lens system, spherical wavefronts of different curvatures shift the focal plane of the nanojet. For instance, diverging spherical wavefronts pushes the nanojet spot away from its principal focal plane (the shadow-side surface of the sphere) towards the far field as shown in Fig. 9.2(c). This phenomenon was observed with various spheres of different sizes. The corresponding spot sizes were generally found bigger than that of a standard nanojet

created by a plane-wave illumination. Within a certain range, this mechanism allows to adjust the working distance of nanojets. It has to be furthermore stressed that this displacement of the photonic nanojets is stronger the smaller the absolute value of the radius of curvature is. The larger this value is the stronger the illumination resembles a plane wave for which the photonic nanojet is bound to the surface. Continuously adjusting the ROC of the illumination allows to tune this distance, as shown in the measurements, in certain intervals. This may have tremendous implications for the use of such photonic nanojets for high resolution microscopy or also for optical tweezers. There, a free manipulation of the focal position by a suitably chosen illumination would enable the manipulation of trapped objects in space.
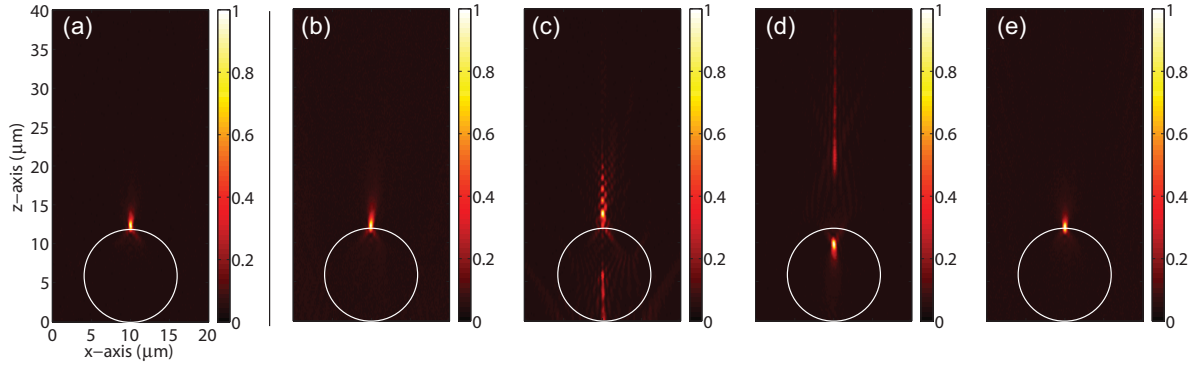

Fig. 9.2: *Longitudinal intensity maps of photonic nanojets generated by a 12-μm glass sphere. (a) Reference measurement with a plane-wave illumination. Engineered nanojets when the sphere is illuminated by (b) diverging wavefront with a ROC of 52.7 μm, (c) diverging wavefront with a ROC of 14.9 μm, (d) converging wavefront with a ROC of -17 μm, and (e) converging wavefront with a ROC of -48.3 μm. The white circle indicates the 12-μm sphere. Intensities are all normalized and the scale of all images is the same.*

9.2 Photonic nanojet generated by Bessel-Gauss beams

A Bessel beam is a non-diffracting beam [9.6, 9.7] with a planar phase evolution in space and a radial amplitude distribution corresponding to a Bessel function. Mathematically, these beams are slightly pathologic since they are infinity extended in space, each ring of the Bessel beam carries the same amount of energy which adds up to infinity, the phase among adjacent rings differs exactly by π, and the Fourier spectrum of such Bessel beam is an infinitely thin ring. Therefore, perfect Bessel beams are inaccessible in a true experiment and their spatial distribution can only be sufficiently approximated within some finite distance. These approximations are experimentally acquired by focusing the parallel annular illumination as explained in chapter 3. As can be seen in Fig. 9.3, where the intensity and the phase

in selected cross-sections of the illumination used in the experiment are shown, the ideal Bessel beam is sufficiently approximated and the beam stretches non-diffracting in a much larger spatial domain than that is of experimental relevance.
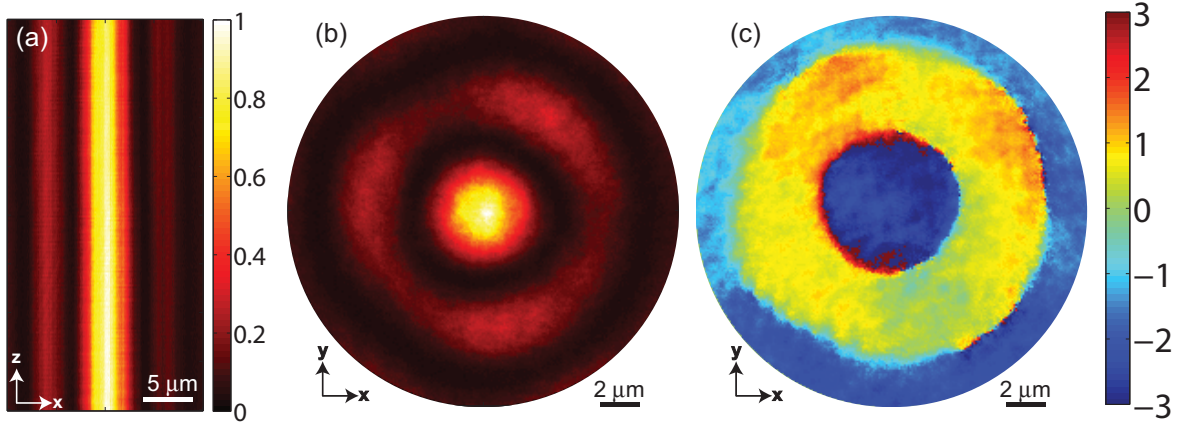

Fig. 9.3: *(a) Measured x-z intensity distribution of a low NA (0.15) focused Bessel beam (the image size is 40 x 20 μm^2). At the plane of z = 0 μm, (b) the x-y intensity and (c) the x-y phase distributions are recorded (the image size is 20 x 20 μm^2). Intenisties are all normalized. The FWHM size of the central lobe is measured to be 4 μm.*

As shown already in Fig. 3.4(f), the wavefronts of such beams are plane but the transverse extension is not continous. Figure 9.3(c) shows a transverse phase distribution, where one observes the discrete wavefronts and their phase difference of π in adjacent rings. Here, our interest is to exploit such discrete-wavefront illuminations. Although there are various experimental configurations, we generalized them and distinguish three cases: (1) a sphere smaller than the central lobe of the Bessel-Gauss beam placed on-axis, (2) a sphere larger than the central lobe placed on-axis, and (3) a sphere placed within two lobes of such a beam (off-axis).

The size of the central lobe of the focused Bessel beam depends on the NA of the focusing lens when the size of the annular pupil is fixed. In our case the central obstraction is 70% of the entrance pupil. Generally, the focal spot that is observed with such illumination is slightly smaller than the focal spot found for the focused Gaussian beams at the same NA since the Bessel function leads to the narrower certral lobe than Airy function [9.8, 9.9]. In order to illuminate the entire surface of the sphere with the central lobe of a Bessel-Gauss beam, we work with a low NA generated by an objective with *NA* = 0.15. The resulting beam characteristics are shown in Fig 9. The FWHM size of the central lobe is measured to be 4 μm. The central phase lobe represents its full size, which is measured to be 7 μm.

9.2.1 On-axis Bessel-Gauss beam

In the first experiment the width of the central lobe is larger than the scattering object, a sphere with a diameter of 2 µm. The longitudinal intensity distribution of the generated nanojet for such a case is shown in Fig. 9.4(a) in a logarithmic intensity scale. Since scattered fields outside the sphere are weak and not observable with a linear intensity scale, a logarithmic scale is used to emphasize the details at low intensity regions. Figure 9.4(b) is a close-up image in the vicinity of the sphere with a linear scale of intensity. The spot size is found to be 360 nm, which stays similar to a plane-wave case (380 nm), and the intensity maximum position is found on the shadow-side surface of the sphere. Since the continuous plane wavefront illuminates the entire surface of the 2-µm sphere, this leads to comparable results as for the plane-wave illumination, as could have been anticipated. Moreover, the self-healing property of the Bessel beam is demonstrated by its rebirth after around 10 µm in the z-axis, clearly identified in Fig. 9.4(a).
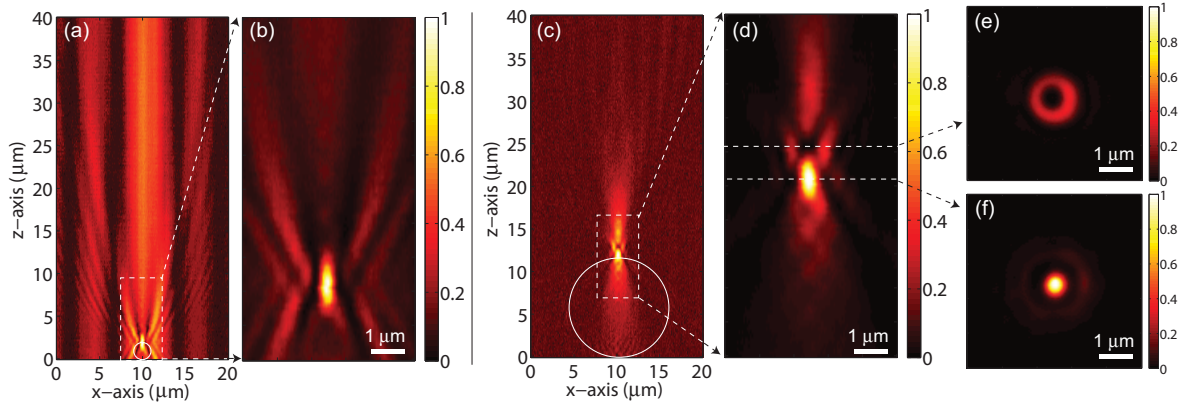

Fig. 9.4: *(a) Measured x-z intensity distribution of a nanojet produced by a 2-µm sphere when the central lobe of the Bessel beam is larger than the sphere and (b) the close-up image of (a). (c) Measured x-z intensity distribution of a nanojet produced by a 12-µm sphere when the central lobe of the Bessel beam is smaller than a sphere and (d) the close-up image of (c). (e) The x-y intensity image at z=13 µm (a dark focus) and (f) the x-y intensity image at z=12 µm (a bright focus). The intensity levels in (a) and (c) are displayed with a logarithmic scale in order to visualize the scattered fields out of the sphere and especially self-healing of the Bessel beam in (a). The white circle indicates the 2-µm sphere in (a) and the 12-µm sphere in (c), respectively. Intensities are all nomalized.*

Now, we examine the nanojet when the central lobe is smaller than the spheres diameter which is chosen to be 12 µm. The measurements are shown in Figs. 9.4(c) - 9.4(f). The dominating spot of the photonic nanojet is formed, as usual, on the surface of sphere with strong intensity confinement. Close to this unique intensity distribution of a nanojet the emergence of a hollow ring is observed. A weak ring-shape intensity lobe, *i.e.,* a dark focus surrounded by regions of higher intensity, is

found between two bright spots. The physical origin of such phenomenon is presumed to be the same mechanism as of an optical bottle beam [9.10, 9.11]. The π phase difference between the central lobe and the 1st lobe of the Bessel beam serves as the annular-shape illumination mask for either phase or amplitude. Similar consequences have been found in Fig. 9.2(c) which can be seen as a chain of optical bottle beams due to the spherical-aberration-induced annular illumination Beams. The formation of such region with a low intensity surrounded by bright regions could find many interesting applications. Examples would be the trapping of particles with a lower index than its surrounding which are known to be pushed towards regions of low intensity [9.12] or for combining possibly microscopes using photonic nanojets with the advantages of a stimulated emission deplection (STED) microscope.

9.2.2 Off-axis Bessel-Gauss beam

To study the case of an off-axis Bessel-beam illumination, a microsphere is placed in between two annulus of an incident Bessel beam, which have a phase difference of π. Since a 2-μm sphere is too small to significantly probe the fields from the two lobes of the given Bessel beam, we work with a 4-μm sphere under the same experimental conditions as pointed out for Fig. 9.4. The optical axis of illumination is shifted away from the sphere (off-axis geometry) as shown in Fig. 9.5(a). The dark ring associated with phase difference divides the illuminating wavefronts in two and finally leads to the emergence of a two-spot nanojet as impressively shown in Fig. 9.5. The longitudinal slices of the measured 3D intensity data are given in Figs. 9.5(c) - 9.5(e). The separation of two bright spots is 220 nm at FWHM, which is about 40% smaller than the measured nanojet spot size at the wavelength of 642 nm. These phenomena are observed with spheres of different sizes and focused Bessel beams of different numerical apertures. Here we experimentally demonstrated the feasibility of beam shaping by specific illuminations when the intensity distributions and wavefronts are not continuous. As we can see in Figs. 9.5(a), 9.5 (b) and 9.5(e), the remaining parts of the illuminating beam outside the sphere are still relatively strong. Nevertheless the phenomenon would be well suited for specific applications such as trapping or patterning. Since the Bessel beam has a self-healing characteristic, manipulating light from the unwanted lobes of the Bessel beam becomes difficult. For many applications only the ratio of confined light intensity to background intensity is important which remains still high in our case. This qualifies our approach to be used for trapping for instance.
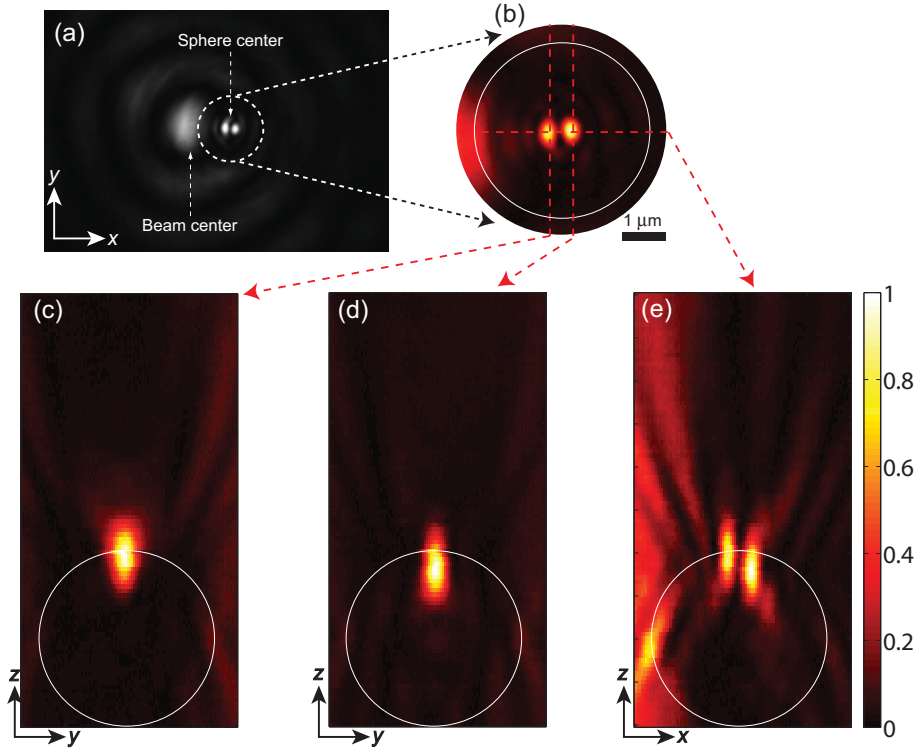
Fig. 9.5: *Measured intensity distributions of the two-spot nanojet from the 4-µm sphere by off-axis Bessel-Gauss beam illumination: (a) a grayscale CCD image of the off-axis Bessel beam and two-spot nanojet, (b) the x-y slice of the 3D intensity distributions at the top of the sphere (c) the y-z slice at the center of the left spot, (d) the y-z slice at the center of the right spot and (e) the x-z slice of the two spots. The white circle indicates the 4-µm sphere. Intensities are all normalized.*

9.3 Beam shaping of nanojets by polarization engineering

As discussed in chapter 4. [see Fig. 4.7], a cylindrical vector beam with an azimuthal polarization is well know to form a doughnut-shape spot when it is focused, and a two-half-circle spot by decomposing with an additional polarizer before the focusing lens. These particular spots do not have side lobes and we can readily control the finite extension of the spot at the entrance plane of the sphere by varying the NA of the focusing lens. The results of experiments with different relations of illumination spot size and sphere size are given in Fig. 9.6. The grayscale CCD images of various illumination spots and engineered nanojet spots for different polarization conditions and sphere sizes are shown. Figure 9.6(a) shows illumination spots recorded at the entrance plane of the sphere without a sphere, which is identical to Fig. 4.7. When the sphere is small, for instance, a 1-µm sphere as in Fig. 9.6(b), only a single section of the illumination, either a bright or a dark part, dominates. A standard nanojet with one spot is observed when setting the

sphere in the bright intensity area where the sphere experiences locally a plane wave illumination. In the case that such a small object is located in the dark part of the illumination, nanojets are not formed and the object is not visible because the sphere is not illuminated with a noticeable strength. Figure 9.6(c) shows the case of a 3-µm sphere, which is covered by both dark and bright parts of the illumination. A hollow nanojet and a two-spot nanojet are generated by corresponding illuminations when polarizations depicted in Fig. 4.7 are used. Since the size of the sphere is smaller than the illumination spot, a part of the direct illumination is still detectable in the focal plane of the nanojet as shown in Fig. 9.6(c). When the sphere is much larger in size than the full extension of the illumination spot, the photonic nanojet takes the form of the illumination as presented in Fig. 9.6(d). To profit best from the beam shape control by polarization the size of the sphere should be larger than or eaqual to the illumination spot size.
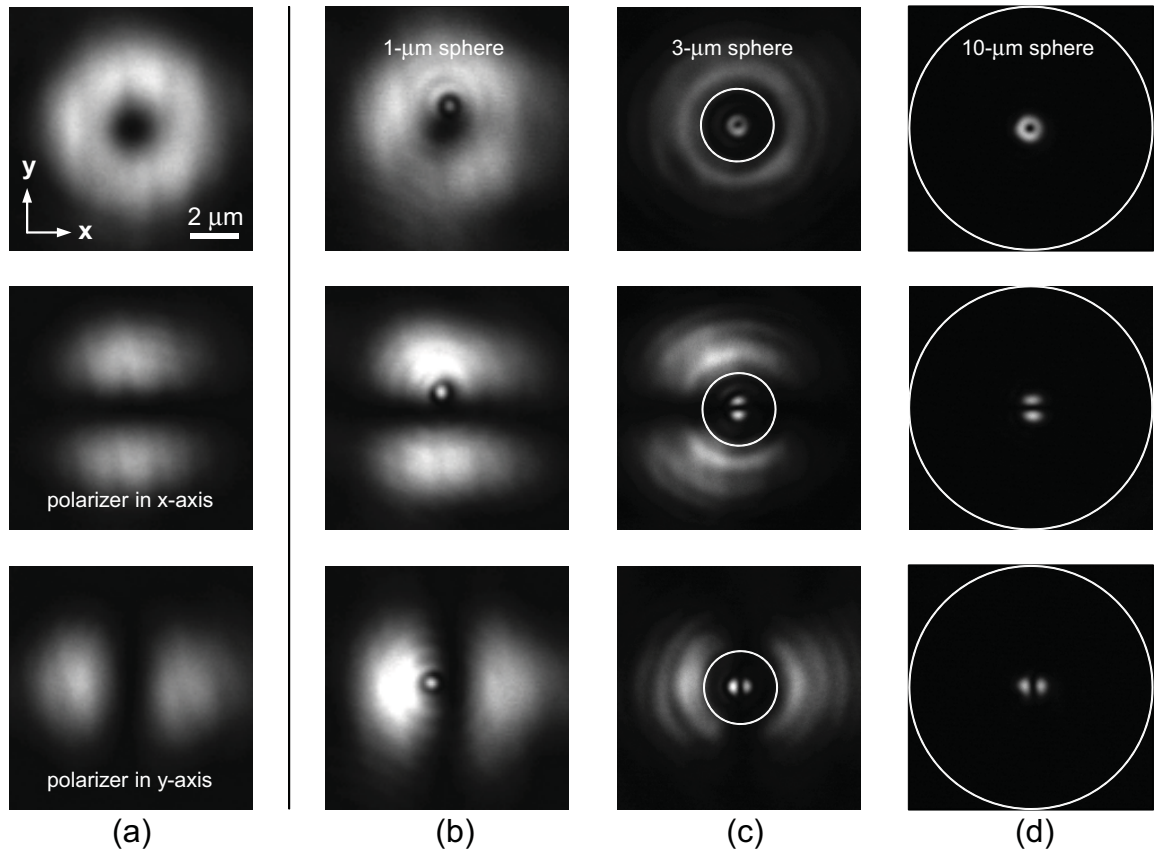

Fig. 9.6: *Grayscale CCD images of particular illumination spots and corresponding engineered nanojet spots by spheres of different size: (a) illumination spots at the entrance plane without a sphere (same as Fig. 4.7), (b) with the 1-µm sphere, (c) with the 3-µm sphere, and (d) with the 10-µm sphere. The image size is 10 x 10 µm^2.*

Figure 9.7 presents the transverse and longitudinal intensity distributions of the hollow nanojet created by the 10-µm sphere, which is shown in the top of Fig. 9.6(d). They demonstrate the extinction of bright spots at the center along the optical axis. The FWHM size of this extinction gap of the hallow nanojet and the two-half-circles nanojet is measured to be around 200 nm, which is 50% smaller than the size of a standard nanojet spot for a given sphere size and wavelength. A possible application for such two-spot nanojets would be direct-write lithography. Scanning these particular intensity distributions of nanojets can allow creating structures with line widths that are much smaller than the diffraction limit but at larger distance. Moreover, super-resolution lithography applicationes can be imagined when two wavelengths are used in illumination, such as done in STED microscopy and absorbance modulation assisted lithography [9.13, 9.14].
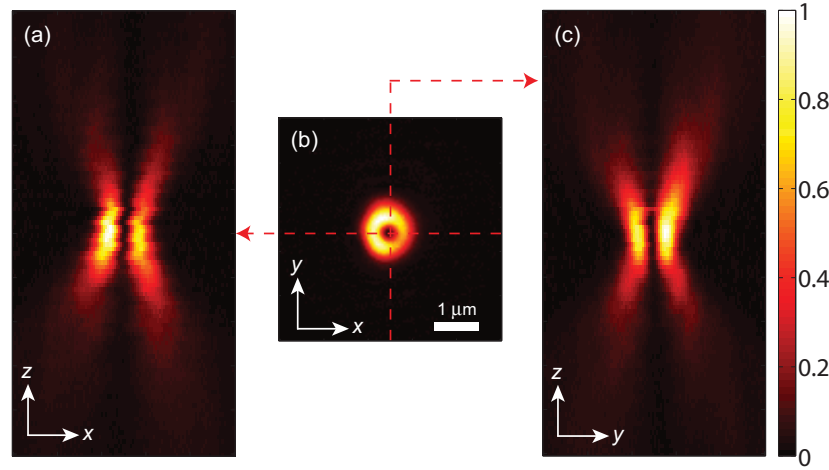

Fig. 9.7: *Measured 3D intensity distribution of the hollow nanojet generated by the 10-µm sphere. This is the same result as shown in the top image of Fig. 8.6(d): (a) the x-z slice, (b) the x-y slice at the focal plane, and (c) the y-z slice of 3D measurement data. The FWHM size of the central dark area is measured to be around 200 nm. The illumination here was an azimuthally polarized beam. Intensity is normalized.*

9.4 Conclusions

When the nanojet has its intensity maximum plane on the back surface of the sphere, it is difficult to utilize in practical applications because of the small distance of the sample and the sphere. To get access to the spot positions we applied spherical wavefront illumination with different radius of curvature. We found that a diverging spherical wavefronts can push the focal plane several micrometers away from the surface of the sphere at the expense of a slightly larger spot size.

The interesting case of a non-diverging beam was studied by applying Bessel-Gauss-beam illumination. We considered two cases: when the central lobe of the Bessel beam is larger or smaller than the sphere. The former leads to the similar response as found in the plane-wave case. The latter, a particular nanojet spot is generated that is larger than the central lobe and resembles an optical bottle beam.

We demonstrated that off-axis Bessel-Gauss beam illumination can create a two-spot nanojet, if the sphere is placed between two intensity lobes. We applied polarization-induced beam shaping to create specific illumination spots, such as a doughnut shape and a two-half-circle shape. nanojets supprisingly reproduce the illumination spot in appearance and transform itself to the hollow nanojet and a two-spot nanojet for the aforementioned cases. In the two-spot nanojet the separation of two spots is approximately 200 nm at 642 nm wavelength, which is smaller than the diffraction limited spot size of the highest NA objective. Our study clarifies different technical aspects of photonics nanojet which are important for its use in different structuring techniques or ultra-resolution applications.

9.5 References

[9.1] A. Heifetz, S.-C. Kong, A. V. Sahakian, A. Taflove, and V. Backman, "Photonic Nanojets," J. Comput. Theor. Nanosci. **6**, 1979-1992 (2009).

[9.2] M.-S. Kim, T. Scharf, S. Mühlig, C. Rockstuhl, and H. P. Herzig, "Engineering photonic nanojets," submitted to Opt. Express (April 2011).

[9.3] A. Devilez, N. Bonod, J. Wenger, D. Gérard, B. Stout, H. Rigneault, and E. Popov, "Three-dimensional subwavelength confinement of light with dielectric microspheres," Opt. Express **17**, 2089-2094 (2009).

[9.4] R. M. Goldstein, H. A. Zebken, and C. L. Werner, "Satellite radar interferometry: Two-dimensional phase unwrapping," Radio Sci. **23**, 713–720 (1988).

[9.5] D. C. Ghiglia and M. D. Pritt, *Two-Dimensional Phase Unwrapping: Theory, Algorithms and Software* (Wiley, 1998).

[9.6] J. Durnin, J.J. Miceli and J.H. Eberly, "Diffraction-free beams," Phys. Rev. Lett. **58**, 1499-19501 (1987).

[9.7] G. Indebetouw, "Nondiffracting optical-fields - some remarks on their analysis and synthesis," J. Opt. Soc. Am. A **6**, 150-152 (1989).

[9.8] M. Born and E. Wolf, *Principles of Optics* (Cambridge University Press, 1999), 7th ed., chap. 8.

[9.9] W. Singer, M. Totzeck, and H. Gross, *Handbook of Optical Systems* (Wiley, 2005) Vol. 2, chap. 25.

[9.10] J. Arlt and M. J. Padgett, "Generation of a beam with a dark focus surrounded by regions of higher intensity: the optical bottle beam," Opt. Lett. **25**, 191–193 (2000).

[9.11] G. M. Philip and N. K. Viswanathan, "Generation of tunable chain of three-dimensional optical bottle beams via focused multi-ring hollow Gaussian beam," J. Opt. Soc. Am. A **27**, 2394-2401 (2010).

94

[9.12] K. T. Gahagan and G. A. Swartzlander, Jr., "Optical vortex trapping of particles," Opt. Lett. **21**, 827-829 (1996).

[9.13] T. F. Scott, B. A. Kowalski, A. C. Sullivan, C. N. Bowman, and R. R. McLeod, "Two-Color Single-Photon Photoinitiation and Photoinhibition for Subdiffraction Photolithography," Science **324**, 913-917 (2009).

[9.14] T. L. Andrew, H.-Y. Tsai, and R. Menon, "Confining Light to Deep Subwavelength Dimensions to Enable Optical Nanopatterning," Science **324**, 917-921 (2009).

CHAPTER 10

Conclusions

The experimental study of highly confined light fields in small volumes with high resolution has been carried out. To do so a special instrument was developed. We presented the details on the uses and developments of a multi-functional high-resolution interference microscope (HRIM), which has been built and evaluated to investigate amplitude and phase of highly confined light fields in a small volume. As light has a wave nature and is characterized by amplitude and phase, experimental probing of this requires coherent detection methods, such as interferometry; the ideal concept to measure the amplitude and phase of light. In addition to the interferometric technique, a microscopic imaging system with the highest numerical apertures helps to measure objects with high resolution. Therefore, the HRIM consists of two main units, such as an optical interferometer and an optical microscope, for studying highly confined light fields in small volumes with high resolution.

As long as the imaging system stands for an optical microscope, the performance of the amplitude measurement is diffraction limited. Therefore, the numerical aperture of the observation objective governs the nominal lateral resolution, which is given by the Abbe limit (= $0.5\lambda/NA$). Actual resolution has been verified by comparing measurements of photonic nanojet spots, which have a particular size and position of the intensity maximum, with rigorous simulation results when the NA of the system is included in the calculations. The longitudinal resolution is derived by the Rayleigh unit (= $n\lambda/NA^2$) along the optical axis, which also falls in the concept of the diffraction limited performance. The phase resolution of the HRIM has been evaluated as the minimum detectable variation of phase across the measurement

plane, which is measured to be 0.01λ at 642 nm wavelength. Such actual resolutions in amplitude and phase measurements depend on the experimental conditions; therefore, they can be improved by better optical elements and sample preparation techniques.

For the refractive confinement of light, the highest available liquid immersion system, such as NA = 1.4 in oil immersion, was applied to generate a focus of 300-nm FWHM spot size at 642 nm wavelength. We investigated the influence of the NA variation on the focusing and observing objective. As expected the NA equivalently limits the resolution in all cases. When the NA of the observing lens is larger than the NA of the object (focusing), the measurement system can resolve the object. For the opposite case, the response of the system relies on the NA of the observation system. From the intensity measurements, the shape and size of the focal spot are the main information to be retrieved. The phase distributions show the evolution of the wavefronts, which follows the conventional concept as a converging wave reaches the focal plane and diverges with the opposite sign of curvature. In the focal plane, the Airy pattern is observed as a form of phase rings, where the wavefronts are retained to be plane. The central phase disc represents the Airy disc, which is isolated by phase singularities.

The diffractive confinement has been studied with single circular objects of two different sizes (4 μm and 10 μm) and periodic structures, *i.e.*, fine amplitude gratings whose periods are comparable to the operation wavelength. For the single objects' case, the spot of Arago serves as the footprint of light confinement. The intensity measurements prove the existence of the Arago spot appearing in the shadow of the obstacle. In addition, the phase measurements reveal the peculiar evolution of phase along the optical axis. The larger obstacle (10 μm) creates more complex field distributions and a greater axial phase shift. For the gratings, the Talbot effect and corresponding Talbot images demonstrate diffractive light confinements with peroidicity of the transverse and longitudinal directions. The multiple-wavelength measurements show the wavelength dependency of the diffraction angle and the Talbot length. The phase distributions show particular feature like phase singularities at the self-image planes, which are a multiple of half the Talbot length. While intensity fields are smoothened for fewer diffraction orders, singularities are observed under all conditions. The position of singularities can serve as a precise indicator of the Talbot length for measurement applications. With the Fourier plane filtering ability of the HRIM, we studied the diffraction from the 1-μm period grating immersed in oil and illuminated at normal incidence by a monochromatic plane wave. We empirically learned that such effect is originated by interference between diffracted fields in the Fresnel (near-field) diffraction regime even for the non-paraxial orders. The Talbot images, which have axial periodicity, only occur when a minimum of three adjacent orders contribute to form images. Higher diffraction orders contribute to form sub-Talbot images.

The specific scattering confinement by a single dielectric microsphere, the photonic nanojet phenomenon, has been studied. Especially, the longitudinal-differential phase measurements lead to insights of its axial phase evolution along the propagation direction. The axial phase shift is comparable to the Gaussian beam case, *i.e.,* the Gouy phase shift. We investigated the influence of the size of the sphere untill several hundreds micrometers on such light confinement. Amplitude and phase disrtibutions differ when the sphere sizes are varied. Finally, we distinguished two regimes for dielectric microspheres: (1) photonic nanojet regime, where scattering phenomenon leads to small spots and the confinement of light occurs on the surface of the sphere [diameter = 1 µm - 10 µm], and (2) a refractive dominant regime, where the hotspots are at distance from the surface of the sphere and has spherical aberration that enlarge the spot sizes and destroys the axial symmetry [diameter = 15 µm - 400 µm]. In the latter case, ball lens optics can be applied to predict the actual properties like a focal length (distance of the peak intensity from the sphere surface). However, the spot sizes are not predictable by ray optics. Rigorous calculations or high-resolution measurements only can provide the proper understanding of the actual properties.

The HRIM allows to manipulate the illumination conditions, for wavefronts and polarization status. Such abilities serve to broden the range of experiments for given samples. We applied the illumination engineering techniques to modify and engineer the properties of the photonic nanojets. We found that a diverging spherical wavefronts can push the focal plane several micrometers away from the surface of the sphere at the expense of a slightly larger spot size. The shape of illumination beams lead to particular shapes of the nanojet spots. For example, the polarization-induced beam shaping, which creates a doughnut shape and a two-half-circle shape, has been applied to form a localized illumination beam on the bottom of the sphere (where we define the entrance plane of the sphere) with such shapes. Created nanojets by these specific illuminations supprisingly reproduce the illumination spot in appearance and transform itself to the hollow nanojet and a two-spot nanojet. In the two-spot nanojet the separation of two spots is approximately 200 nm at a 642 nm wavelength, which is smaller than the diffraction limited spot size of the highest NA objective. These engineered nanojets provide the guidelines for different structuring techniques or ultra-resolution applications.

The 3D measurements of the amplitude and phase of highly confined light fields under various situations have been demonstrated. Its capability of measuring phase distributions in 3D with two different modes, propagation and longitudinal-differential, makes it very attractive for the study of peculiar behaviors of light fields along the axial direction, *e.g.,* axial phase shifts or phase anomalies. An experimental proof of the existence of the Gouy phase shift in scattered hotspots has been for the first time found out thanks to such longitudinal-differential phase measurements. To the best of our knowledge, for such highly confined light fields

the differential phase measurements in the real 3D object space are the first demonstration, and this is the unique performance of the HRIM compared to other interference microscopes. Furthermore, its functionalities have been extended by employing the auxiliary techniques of conventional light microscopy in order to meet the proper experimental conditions for different samples and structures. Therefore, this instrument, the multi-functional HRIM, may be helpful in several domains, particularly, for understanding the fundamentals of light interactions with micro- or nano-structures.

List of abbreviations

2D two dimensional

3D three dimensional

BFL back focal length / **EFL** effective focal length

BS beam splitter / **PBS** polarizing beam splitter

CCD a charge-coupled device

FWHM a full width at half maximum

G-T Gland- Taylor polarizer

HRIM high-resolution interference microscopy

HWP half wave plate

NA numerical aperture

OPL optical path length

PSI phase shifting interferometry

PZT a piezoelectric transducer

ROC radius of curvature

SNOM scanning near-field optical microscopy

STED a stimulated emission deplection microscope

List of publications

Peer reviewed journals

- M.-S. Kim, T. Scharf, S. Mühlig, C. Rockstuhl, and H. P. Herzig, "Gouy Phase Anomaly in Photonic Nanojets," Appl. Phys. Lett. **98**, 191114 (2011).

- M.-S. Kim, T. Scharf, S. Mühlig, C. Rockstuhl, and H. P. Herzig, "Engineering photonic nanojets," Opt. Express **19**, 10206 (2011).

- M.-S. Kim, T. Scharf, and H. P. Herzig, "Small size microlens characterization by Multiwavelength High Resolution Interference Microscopy," Opt. Express **18**, 14319-14329 (2010).

- M.-S. Kim, T. Scharf, and H. P. Herzig, "Amplitude and Phase Measurements of Highly Focused Light in Optical Data Storage Systems," Jpn. J. Appl. Phys. **49**, 08KA03 1-5 (2010) .

SPIE Proceedings

- T. Scharf, M.-S. Kim, and H. P. Herzig, "Measuring amplitude and phase of light emerging from microstructures with HRIM," Proc. of SPIE Vol. 8082, 80821O (2011).

- M.-S. Kim, T. Scharf, S. Mühlig, C. Rockstuhl, and H. P. Herzig, "Photonic Nanojet engineering: Focal point shaping with scattering phenomena of dielectric microspheres," Proc. of SPIE Vol. 7941, 794115 (2011).

Conferences and workshops

- H. P. Herzig, M.-S. Kim, and T. Scharf, " Measuring amplitude and phase of light emerging from microstructures with HRIM," EOS Conference on Manufacturing of Optical Components (EOSMOC), Munich, Germany, 2011.

- Myun-Sik Kim, Toralf Scharf, Stefan Mühlig, Carsten Rockstuhl, and Hans Peter Herzig, "Photonic Nanojet engineering: Focal point shaping with scattering phenomena of dielectric microspheres," Photonics West, San Francisco, USA, 2011.

- Myun-Sik Kim, "Measuring 3D amplitude and phase distribution of sub-wavelength diffraction phenomena," EPFL Photonics Day, Lausanne, Switzerland, 2010.

- Myun-Sik Kim, Toralf Scharf, Hans Peter Herzig, Stefan Mühlig, and Carsten Rockstuhl, "Amplitude and Phase fields of Photonic Nanojets," EOS Annual meeting, Paris, France, 2010.

- Myun-Sik Kim, Toralf Scharf, and Hans Peter Herzig, "Measuring amplitude and phase of light emerging from microstructures with the high resolution interference microscope," 8th Fraunhofer IISB Lithography Simulation Workshop, Hersbruck, Germany, 2010.

- Myun-Sik Kim, Toralf Scharf, and Hans Peter Herzig, "MEASUREMENTS OF LIGHT FIELDS EMERGING FROM FINE AMPLITUDE GRATINGS," Optical MEMS and Nanophotonics, Sapporo, Japan, 2010.

- Myun-Sik Kim, Toralf Scharf, and Hans Peter Herzig, "Multiwavelength High Resolution Interference Microscopy (HRIM) for the characterization of small size microlenes," Annual Conference of Association des Scientiques Coréens en France (ASCoF), Rennes, France, 2010.

- Myun-Sik Kim, Toralf Scharf, and Hans Peter Herzig, "High Resolution Interference Microscopy: 3D measurement of focused light at 405nm applied to optical disc," International Symposium on Optical Memory (ISOM), Nagasaki, Japan, 2009.

- Toralf Scharf, Myun-Sik Kim, and Hans Peter Herzig, "Characterization of small size microlenses by high resolution interference immersion microscopy," 15th Microoptics Conference (MOC), Tokyo, Japan, 2009.

- Myun-Sik Kim, Toralf Scharf, and Hans Peter Herzig, "Interferometric Measurement on a Nanometric Length Scale," Atelier LEA-Microtechnique (Laboratorie Européenne Associé en microtechnique), Arc-et-Senans, France, 2008.

Acknowledgements

I would like to express my gratitude to people, whose helpful supports, discussions and advices led to the completion of my thesis and successful accomplishments.

First of all, I wish to thank my theiss director, Prof. *Hans Peter Herzig*. When I contacted first time for the one-year visit for the internship research in 2004, he willingly gave me the chance to work with his group (*Omar Manzardo*). This first helpful event made me to start my Ph.D. study with him in 2008. He was always open to my fundamental questions and discussions to find out solutions of encountered problems, not only scientific ones but also personal ones.

I want to thank my thesis co-director, Dr. *Toralf Scharf*. During the first business trip together, he gave me a clue that brought my success of this thesis work: "Power Distance Index (PDI)" which explains difficulties of communications and gaps between a higher one and a lower one, *e.g.*, a boss and an employee or a professor and a student. In Germany, this index is fortunately quite lower, *i.e.*, easy to communicate between people regardless of the power difference. I was knocking on his door almost everyday even during the weekend by e-mail. He was naturally ready to discuss and come down to teach me in the cleanroom (I guess due to the low PDI culture).

I express my gratitude to the other mbembers of the Jury, Prof. *Oliver Martin*, Prof. *Christian Depeursinge*, Prof. *Paul Urbach*, and Prof. *Carsten Rockstuhl*, for their critical review of my theiss and examining my work.

When I had difficulties for numerical calculations and theoretical considerations, the collaboration with *Stefan Mühlig* and *Carsten Rockstuhl* releaved me from the desert of doubts. Finally, this made two peer reviewed journal papers published.

Special thanks to *Wataru Nakagawa* who did the phone interview for my Ph.D. position in 2007. After I started my Ph.D work, he gave me helpful advices for my study and personal life in Switzerland, which were the seeds of my success.

I am very grateful to *Marcel Groccia*, who helped me not only for the electronic devices but also for lab. affairs, and *Iréne Philipoussis* for the fabrications and replications of the samples.

104

Myunsik KIM

EPFL STI IMT OPT
Rue A.-L. Breguet 2, 2000 Neuchâtel
Tel. (work): +41 (0)32 718 3279
Web: http://people.epfl.ch/myunsik.kim

Av. des Alpes 11, 2000 Neuchâtel,
Tel. (cell phone): +41 (0)76 584 3940
E-mail: myunsik.kim@epfl.ch
    myunsik@hotmail.com

Eduacation

2008-2011…………École Polytechnique Fédérale de Lausanne (EPFL), Switzerland, **Doctor of Science in Photonics** (Ph.D.), thesis entitled "*On the characteristics of highly confined light fields: A high-resolution interference microscopy study*".

2002-2004…………Gwangju Institute of Science and Technology (GIST), Korea, **Master of Science in Mechatronics** (M Sc.), thesis entitled "*Design and fabrication of a self-aligned microlens on the sidewall of 45°-angled optical fiber*". (GPA : 3.72 / 4.5)

1996-2002…………Kookmin University, Korea, **Bachelor of Science in Automotive engineering**. (Early graduation with *Summa cum laude* equivalent GPA : 4.12 / 4.5)

Professional Experience

2008-2011…………École Polytechnique Fédérale de Lausanne (EPFL), Switzerland, **Research Assistant.**
• **SU**per-**R**esolution **P**hotonics for **A**dvanced **S**torage **S**ystems (SURPASS)
 funded by Euroapean Comission's Seventh Framework Programme (FP7)

2006-2008…………Seoul Semiconductor Co. LTD, Korea, **Overseas Sales.**
• LED (light emitting diode) manufacturing company
• Job function : exporting affairs and international customer relations

2005-2006…………CERAGEM Salud España, Spain, **Sales and Marketing.**
• Automatic massage machine distributor in Spain
• Job function : importing affairs and domestic sales in Spain and marketing

2004-2005…………Institute of Microtechnology, University of Neuchâtel, Switzerland, **Visiting Researcher.**
• Development of parallel AFM with optical heterodyne detection method
• Color measurements with a MEMS-type spectrometer

2002-2004…………Gwangju Institute of Science and Technology (GIST), Korea, **Research Assistant.**
• Development of illumination system to miniaturize SNOM datastorage
• Development of a micromachined (MEMS) optical switch for telecommunication

2000 Spring…..……Korea Electric Power Corporation (KEPCO), Korea, **Assistant Technician.**
• Reparing and maintenance of steam power generators
• Maintenance for the control and measurement sensors (flow, pressure, and temperaturte)

1997-1999…………Military Service at 1st Division of Korean Army, Korea, **Sergeant.**
• Military service
• Award by the division commander / Served as a squad leader for training

Volunteer Work

1993-1996…………Red Cross Youth (RCY), Korea.
• Services at orphanages, elderly care facilities, and deaf-mute schools
• Monthly street-campaign for the blood donation

Technical Training

2004 December……Handling and Assembly of MOEMS, Neuchâtel, Switzerland.
• at Fondation Suisse pour la recherche en microtechnique (FSRM)

2003 July…..……Training Course of Semiconductor Processes, Seoul, Korea
• at Inter-university semiconductor research center (ISRC) at Seoul National University
• CMOS processes (Ion implantation, Phptolighography, CVD, Etching, Metallization, and *etc*.)

Langueage and Hobby

• **Korean**: mother tongue
• **English**: fluent
• **Spanish**: fluent
• **French**: intermediate

• **Sports**: Ski, Tennis, Karate, and
    Horse back riding.
• **Traveling**
• **Fishing**

Curriculum Vitae: Myunsik KIM

Awards

2004-2005…………Korean Government scholorship for overseas internship for 1 year.

2002-2004…………Korean Government scholorship for the Master degree study.

2002………..………Early graduation with *Summa cum laude* equivalent.

2000-2002…………Listed in the dean's list with scholarship during the Bachelor study.

1999………..………1st grade award by the division commander at the squad leader training (Military service).

Publication List

Peer reviewed journals

• M.-S. Kim, T. Scharf, S. Mühlig, C. Rockstuhl, and H. P. Herzig, "Gouy Phase Anomaly in Photonic Nanojets," Appl. Phys. Lett. **98**, 191114 (2011).

• M.-S. Kim, T. Scharf, S. Mühlig, C. Rockstuhl, and H. P. Herzig, "Engineering photonic nanojets," Opt. Express **19**, 10206 (2011).

• M.-S. Kim, T. Scharf, and H. P. Herzig, "Small size microlens characterization by Multiwavelength High Resolution Interference Microscopy," Opt. Express **18**, 14319 (2010).

• M.-S. Kim, T. Scharf, and H. P. Herzig, "Amplitude and Phase Measurements of Highly Focused Light in Optical Data Storage Systems," Jpn. J. Appl. Phys. **49**, 08KA03 (2010) .

• M.-S. Kim, K.-W. Jo, and J. H. Lee, "Design and fabrication of a microlens on the sidewall of an optical fiber with a metallized 45° end face," Appl. Opt. **44**, 3985 (2005).

• K.-W. Jo, M.-S. Kim, J. H. Lee, E.-K. Kim, and K.-H. Park, "Optical Characteristics of a Self-aligned Microlens Fabricated on the Sidewall of a 45°-angled Optical Fiber," Photon. Technol. Lett. **16**,138 (2004).

SPIE Proceedings

• T. Scharf, M.-S. Kim, and H. P. Herzig, "Measuring amplitude and phase of light emerging from microstructures with HRIM," Proc. of SPIE Vol. 8082, 80821O (2011).

• M.-S. Kim, T. Scharf, S. Mühlig, C. Rockstuhl, and H. P. Herzig, "Photonic Nanojet engineering: Focal point shaping with scattering phenomena of dielectric microspheres," Proc. of SPIE Vol. 7941, 794115 (2011).

Conferences and workshops

• H. P. Herzig, M.-S. Kim, and T. Scharf, " Measuring amplitude and phase of light emerging from microstructures with HRIM," EOS Conference on Manufacturing of Optical Components (EOSMOC), Munich, Germany, 2011.

• M.-S. Kim, T. Scharf, S. Mühlig, C. Rockstuhl, and H. P. Herzig, "Photonic Nanojet engineering: Focal point shaping with scattering phenomena of dielectric microspheres," Photonics West, San Francisco, USA, 2011.

• Myun-Sik Kim, "Measuring 3D amplitude and phase distribution of sub-wavelength diffraction phenomena," EPFL Photonics Day, Lausanne, Switzerland, 2010.

• M.-S. Kim, T. Scharf, S. Mühlig, C. Rockstuhl, and H. P. Herzig, "Amplitude and Phase fields of Photonic Nanojets," EOS Annual meeting, Paris, France, 2010.

• M.-S. Kim, T. Scharf, and H. P. Herzig, "Measuring amplitude and phase of light emerging from microstructures with the high resolution interference microscope," 8th Fraunhofer IISB Lithography Simulation Workshop, Hersbruck, Germany, 2010.

• M.-S. Kim, T. Scharf, and H. P. Herzig, "MEASUREMENTS OF LIGHT FIELDS EMERGING FROM FINE AMPLITUDE GRATINGS," Optical MEMS and Nanophotonics, Sapporo, Japan, 2010.

• M.-S. Kim, T. Scharf, and H. P. Herzig, "Multiwavelength High Resolution Interference Microscopy (HRIM) for the characterization of small size microlenes," Annual Conference of Association des Scientiques Coréens en France (ASCoF), Rennes, France, 2010.

• M.-S. Kim, T. Scharf, and H. P. Herzig, "High Resolution Interference Microscopy: 3D measurement of focused light at 405nm applied to optical disc," International Symposium on Optical Memory (ISOM), Nagasaki, Japan, 2009.

• T. Scharf, M.-S. Kim, and H. P. Herzig, "Characterization of small size microlenses by high resolution interference immersion microscopy," 15th Microoptics Conference (MOC), Tokyo, Japan, 2009.

- R. Bitterli, M.-S. Kim, T. Scharf, and H. P. Herzig, "Fabrication and Characterization of 1-D diffusing elements," 15th Microoptics Conference (MOC), Tokyo, Japan, 2009.
- R. Bitterli, M.-S. Kim, T. Scharf, and H. P. Herzig, "Fabrication Rules and Characterization of Concave Microstructures in Fused Silica," EOS Annual Meeting, Paris, France, 2008.
- M.-S. Kim, T. Scharf, and H. P. Herzig, "Interferometric Measurement on a Nanometric Length Scale," Atelier LEA-Microtechnique (Laboratorie Européenne Associé en microtechnique), Arc-et-Senans, France, 2008.
- O. Manzardo, L. Chantada, M.-S. Kim, L. Aeschimann, T. Akiyama, N.F. de Rooij, U. Staufer, P. Vettiger, R. Dändliker and H. P. Herzig, "Optical Read-out of Parallel Cantilever AFM arrays," Int. Conf. Nanoscience and Technology, Brisbane, Qld, Australia, 2006.
- L. Chantada, M.-S. Kim, O. Manzardo, R. Dändliker, L. Aeschimann, U. Staufer, P. Vettiger, K. Weible and H. P. Herzig, "Parallel atomic force microscopy using optical heterodyne detection," MEMS, MOEMS, and Micromachining II, Strasbourg, France, 2006.
- M.-S. Kim, O. Manzardo, R. Dändliker, H. P. Herzig, L. Aeschimann, U. Staufer, P. Vettiger, and J. H. Lee, "Atomic Force Microscopy with Optical Heterodyne Detection Method," IEEE/LEOS International Conference on Optical MEMS, Oulu, Finland, 2005.
- M.-S. Kim, K.-W. Jo, J. H. Lee, "Dimension controllability and Reflow characteristics of Self-aligned Microlens on the Sidewall of 45°-angled Optical Fiber for compact SNOM Optics," International Conference on OECC, Yokohama, Japan, 2004.
- M.-S. Kim, K.-W. Jo, T.-H. Kim, and J. H. Lee, "Reflow characteristics of a self-aligned PR pattern for compact SNOM optics," Korean MEMS Conference, Jeju, Korea, 2004.
- M.-S. Kim, K.-W. Jo, J. H. Lee, "Self-aligned Microlens Fabricated on the Sidewall of 45°-angled Optical Fiber for NSOM Illumination System," IEEE/LEOS International Conference on Optical MEMS, Hawaii, USA, 2003.

References

Professor Hans Peter Herzig

EPFL STI IMT OPT   Tel: +41 32 718 3270

Rue A.-L. Breguet 2, 2000 Neuchâtel   E-mail: hanspeter.herzig@epfl.ch

Dr. Toralf Scharf

EPFL STI IMT OPT   Tel: +41 32 718 3286

Rue A.-L. Breguet 2, 2000 Neuchâtel   E-mail: toralf.scharf@epfl.ch

Professor Jong Hyun Lee

Gwangju Institute of Science and Technology,   Tel. : + 82 62 715 2395

261 Cheomdan-gwagiro, Buk-gu, Gwangju   E-mail : jonghyun@gist.ac.kr

500-712, Republic of Korea   Web: http://mems.gist.ac.kr